# Charge-transport simulations in organic semiconductors

Dissertation

zur Erlangung des Grades

"Doktor der Naturwissenschaften"

am Fachbereich Physik, Mathematik und Informatik
der Johannes Gutenberg-Universität Mainz

**Falk May**

geb. in Heidelberg

Max-Planck-Institut für Polymerforschung

Mainz, den 04. Juni 2012

# Publications

Parts of this thesis have been submitted or are already published in the following references:

- **V. Ruehle, A. Lukyanov, F. May, M. Schrader, T. Vehoff, J. Kirkpatrick, B. Baumeier, D. Andrienko**
  *Microscopic Simulations of Charge Transport in Disordered Organic Semiconductors*
  J. Chem. Theory Comput., 7, 3335-3345, 2011.

- **F. May, V. Marcon, M. R. Hansen, F. Grozema, D. Andrienko**
  *Relationship between Supramolecular Assembly and Charge-carrier Mobility in Perylenediimide Derivatives: the Impact of Side Chains*
  J. Mater. Chem. 21, 9538-9545, 2011.

- **B. Baumeier, F. May, C. Lennartz, D. Andrienko**
  *Challenges for in silico design of organic semiconductors*
  J. Mater. Chem., 2012.

- **F. May, B. Baumeier, C. Lennartz, D. Andrienko**
  *Can lattice models predict density of states of amorphous organic semiconductors?*
  Submitted.

- **F. May, M. Al-Helwi, B. Baumeier, W. Kowalsky, E. Fuchs, C. Lennartz, D. Andrienko**
  *Design rules for charge-transport efficient host materials for phosphorescent OLEDs*
  Submitted.

Publications that are not related to this thesis, but have been finalized while working at the Max Planck Institute for Polymer Research:

- **A. Zyazin, J van den Berg, E. Osorio, H. van der Zant, N. Konstantinidis, M. Leijnse, M. Wegewijs, F. May, W. Hofstetter, C. Danieli, A. Cornia**
  *Electric Field Controlled Magnetic Anisotropy in a Single Molecule*
  Nano Lett. 10(9), 3307-3311, 2010.

- **F.May*, C. Romeike, M. R. Wegewijs, W. Hofstetter, H. Schoeller**
  *Erratum: Kondo-Transport Spectroscopy of Single Molecule Magnets*
  Phys. Rev. Lett. 106, 019902(E), 2011.

- **F.May*, C. Romeike, M. R. Wegewijs, W. Hofstetter, H. Schoeller**
  *Corrigendum: Magneto-transport through single-molecule magnets: Kondo-peaks, zero-bias dips, molecular symmetry and Berry's phase*
  J. New. Phys. 13, 079501, 2011.

- **F.May, M.R.Wegewijs, W.Hofstetter**
  *Spin-Vibration Coupling in Transport Through Single Molecule Magnets*
  Beilstein J. Nano. 2, 693-698, 2011.

*:Although the work of this erratum was performed by F.May, he could not appear in the author list because he was not an author of the erroneous original manuscript.

# Abstract

In this thesis we have extended the methods for microscopic charge-transport simulations for organic semiconductors, where weak intermolecular interactions lead to spatially localized charge carriers, and the charge transport occurs as an activated hopping process between diabatic states. In addition to weak electronic couplings between these states, different electrostatic environments in the organic material lead to a broadening of the density of states for the charge energies which limits carrier mobilities.

The contributions to the method development include (i) the derivation of a bimolecular charge-transfer rate, (ii) the efficient evaluation of intermolecular (outer-sphere) reorganization energies, (iii) the investigation of effects of conformational disorder on intramolecular reorganization energies or internal site energies and (iv) the inclusion of self-consistent polarization interactions for calculation of charge energies.

These methods were applied to study charge transport in amorphous phases of small molecules used in the emission layer of organic light emitting diodes (OLED). When bulky substituents are attached to an aromatic core in order to adjust energy levels or prevent crystallization, a small amount of delocalization of the frontier orbital to the substituents can increase electronic couplings between neighboring molecules. This leads to improved charge-transfer rates and, hence, larger charge-mobility. We therefore suggest using the mesomeric effect (as opposed to the inductive effect) when attaching substituents to aromatic cores, which is necessary for example in deep blue OLEDs, where the energy levels of a host molecule have to be adjusted to those of the emitter. Furthermore, the energy landscape for charges in an amorphous phase cannot be predicted by mesoscopic models because they approximate the realistic morphology by a lattice and represent molecular charge distributions in a multipole expansion. The microscopic approach shows that a polarization-induced stabilization of a molecule in its charged and neutral states can lead to large shifts, broadening, and traps in the distribution of charge energies. These results are especially important for multi-component systems (the emission layer of an OLED or the donor-acceptor interface of an organic solar cell), if the change in polarizability upon charging (or excitation in case of energy transport) is different for the components. Thus, the polarizability change upon charging or excitation should be added to the set of molecular parameters essential for understanding charge and energy transport in organic semiconductors.

We also studied charge transport in self-assembled systems, where intermolecular packing motives induced by side chains can increase electronic couplings between molecules. This leads to larger charge mobility, which is essential for devices such as organic field effect transistors. However, it is not sufficient to match the average local molecular order induced by the side chains with maxima of the electronic couplings. It is also important to make the corresponding distributions, e.g. of the pitch angle between consecutive molecules, as narrow as possible compared to the window determined by the closest minima of the electronic couplings. The immediate implication for compound design is that the side chains should assist the self-assembling process not only via "soft" entropic interactions, but also via stronger specific interactions, such as hydrogen bonding.

# Contents

# Chapter 1

# Introduction

After the discovery of electrical charge-carrier transport in conjugated polymers in 1977 by Heeger, MacDiarmid, and Shirakawa [1], who were awarded the Nobel Prize in chemistry 2000, the field of organic electronics has significantly expanded which was a result of combined efforts of several scientific communities. Synthetic chemists have identified classes of promising compounds, ranging from small conjugated molecules to self-assembling oligomers and conjugated polymers and developed new synthetic routes, improving both stability and processability of the materials [2–8]. At the same time, material processing, such as doping, annealing, use of a secondary solvent and composition tuning, has been adjusted to the demands of the field [9–14]. Furthermore, device efficiencies could be increased, e.g. by optimizing light in- and out-coupling and introducing tandem concepts [15, 16]. The power-conversion efficiency of organic solar cells, for example, increased by one order of magnitude between its first demonstration in 1986 [17] to above 10% achieved in 2012 by the company Heliatek using vacuum-deposited small molecules [18].

The fundamental difference between organic semiconductors and their inorganic counterparts lies in the nature of the bonding. While materials such as Si or GaAs are covalently bonded, organic molecules interact via much weaker Coulomb and Van der Waals forces. As a consequence, the electronic states available for charge carriers are spatially localized on the molecules which is in contrast to the situation in traditional inorganic semiconductors where the electronic states are delocalized (but since the valence and conduction band are energetically separated, the conductivity is low compared to conductors). Due to the localization, sufficient electronic coupling between and in the organic molecules is necessary to allow for charge transport. This can be achieved in compounds that consist of $\pi$-systems formed by the $p_z$ orbitals of $sp^2$-hybridized C-atoms (that can be combined, e.g. with electron donating S-atoms) allowing for overlap of the frontier orbitals at van der Waals distances.

In organic semiconductors, charge transport can be described as a thermally activated hopping process triggered by nuclear motion that occurs between initial and final *diabatic* states. These states correspond to the charge being localized on the donor in the initial state (while the acceptor is neutral), and vice versa for the final state. In other words, the time for the electronic wave function to move from donor to acceptor, $\tau_{\mathrm{el}} = \hbar/J$, that can

be estimated from the electronic coupling $J$ and the reduced Planck's constant $\hbar$, is much larger compared to the time for nuclear motion of the promoting mode $\tau_{\mathrm{nuc}} = 2\pi/\omega_{\mathrm{vib}}$ [19]. The criterion for this nonadiabatic electron transport, $\tau_{\mathrm{el}} \gg \tau_{\mathrm{nuc}}$, is fulfilled for most organic semiconductors since the promoting mode is typically given by C-C stretching modes with vibrational energy $\hbar\omega_{\mathrm{vib}} = 0.2\,\mathrm{eV}$ [20], while electronic couplings between the localized states are of the order of $J < 0.01\,\mathrm{eV}$ in the amorphous phase. Therefore, the charge transport rate can be obtained from first order perturbation theory with respect to $J$ using Fermi's golden rule, where the unperturbed states are given by the diabatic states. An exception to this situation can occur in highly ordered molecular crystals, where strong electronic couplings of up to $J = 0.2\,\mathrm{eV}$ can be achieved and the picture of diabatic states is not valid anymore.

Another important aspect of charge transport in organic semiconductors arises from the fact that different electrostatic environments of individual molecules lead to a broadening of the density of states for the charge energies. These site energies can be approximated by a Gaussian distribution characterized by the width $\bar{\sigma}$ (energetic disorder) of typically $0.1\,\mathrm{eV}$ [21, 22]. The energetic disorder limits the charge-carrier mobility $\mu$ and also leads to a field dependence so that in organic semiconductors $\mu \sim \exp\{-[\bar{\sigma}/(k_{\mathrm{B}}T)]^2 + \beta\sqrt{F}\}$, where $k_{\mathrm{B}}T$ is the thermal energy, $F$ is the applied electric field and $\beta$ is known as the Poole-Frenkel slope [23]. This is in contrast to band-like charge transport that occurs in inorganic semiconductors ($J = 10\,\mathrm{eV}$), where the mobility is independent of the electric field and decreases with temperature due to phonon scattering following a power law $\mu \sim T^{-n}$ with $n = 1...3$. However, at room temperature band transport in inorganic semiconductors allows for high mobilities, e.g. in the crystalline phase $\mu = 10^3\,\mathrm{cm}^2/(\mathrm{Vs})$ and in amorphous hydrogenated Si $\mu = 1\,\mathrm{cm}^2/(\mathrm{Vs})$. In contrast to this, the weak electronic coupling and the large energetic disorder in organic semiconductors lead to considerably lower charge-carrier mobility in amorphous phases where $\mu < 10^{-4}\,\mathrm{cm}^2/(\mathrm{Vs})$, while values up to $\mu = 10\,\mathrm{cm}^2/(\mathrm{Vs})$ have been achieved in organic molecular crystals [24].

Also the band gap in organic semiconductors is rather large (typically $E_g = 2.5\,\mathrm{eV}$ while in Si $E_g = 1.1\,\mathrm{eV}$) which results in very low intrinsic charge-carrier density $n \sim \exp[-E_g/(2k_{\mathrm{B}}T)]$. The carrier density can be increased by (electro-)chemical doping, injection from (metallic) electrodes, photo-generation or by field-effect doping. In combination with the low mobility, the low carrier density leads to weak electrical currents $j = en\mu F$ for experimentally accessible electric fields ($e$ is the elementary charge).

The advantage of organic compounds lies in the variety of materials ranging from small conjugated molecules to long polymers. This results in different optical and mechanical properties, such as chemically tunable emission and absorption (typically in the visible range of the spectrum), flexibility (polymers) and low melting point (amorphous phases), but also allows for different processing techniques. On the one hand, molecules with sufficiently low molecular weight can be vapor-deposited from the gas phase or grown in single crystals. On the other hand, materials with larger molecular weight, such as polymers or aromatic molecules with long side-chains, can be processed from solution. Typical techniques are spin-coating followed by evaporation of the solvent and scalable inkjet printing methods.

Possible applications of organic materials range from low-cost printed organic field effect transistors (OFET) to transparent light-weight organic photovoltaic cells (OPVC) and organic light emitting diodes (OLED) for use in large area light sources and flexible and efficient displays with high color quality. OFETs are three-terminal devices in which a gate voltage applied across a thin dielectric controls the charge carrier density and thereby also the electrical current flowing in an organic semiconducting channel between source and drain contact [25]. The current performance of OFETs is limited by insufficient carrier mobilities, allowing only low switching frequencies [26].

In OPVC incoming light is converted into electrical energy, with the main problem being the large exciton binding energy that originates from a low dielectric constant and the strong localization of the excitons on single molecules. Charge separation can be facilitated at a suitable donor-acceptor interface [27], but a high charge-carrier mobility is essential to allow for efficient transport of charges to the electrodes while minimizing recombination losses.

In OLEDs, the reverse process takes place and electrical energy is converted into light. Here, one of the main open issues is the insufficient stability [28] of OLEDs based on deep blue emitters [29, 30]. Several life-time limiting processes can occur during its operation: if the injection of electrons and holes into the emission layer is unbalanced or if their mobilities differ by several orders of magnitude, their recombination takes place in a narrow emission zone and molecules become exposed to high energetic stress which leads to their degradation. Also crystallization has to be prevented which would otherwise lead to formation of strong current filaments along pathways with strongest electronic coupling and molecules become exposed to high electric stress. In addition, all types of organic devices have to be protected by encapsulation against penetration of water or oxygen, which could act as energetic traps for charge-carriers. Thus, improving the performance of OFETs, OPVC and OLEDs is tightly linked to understanding of elementary charge-transfer and -transport processes occurring in these devices.

Computer simulations and modeling contributed substantially to the understanding of the basic physical processes in organic semiconductors [20, 31–33]. In particular, lattice models have been successful in rationalizing the influence of finite charge-carrier concentration [34, 35], explicit Coulomb interactions [36] and the shape of the density of states [37, 38] on charge transport. The drawback of these *mesoscopic* lattice models is that they must be parametrized on experimental data and thus do not provide a direct link to underlying chemical structures. Therefore, they cannot aid compound screening, which is becoming more and more important in view of the large number of organic compounds with semiconducting properties [39].

The goal of this thesis lies in the development and application of an alternative, *microscopic* description of charge transport, the main ingredients of which are illustrated in fig. 1.1. To begin with, every molecule has its own unique environment created by its neighbors, with local electric fields leading to level shifts, broadening, and spatial correlations of charge energies. Accounting for such effects requires the knowledge of the material morphology at an atomic resolution which is obtained by refining force fields that are used in molecular dynamics simulations. Furthermore, typical time scales of dynamic processes,

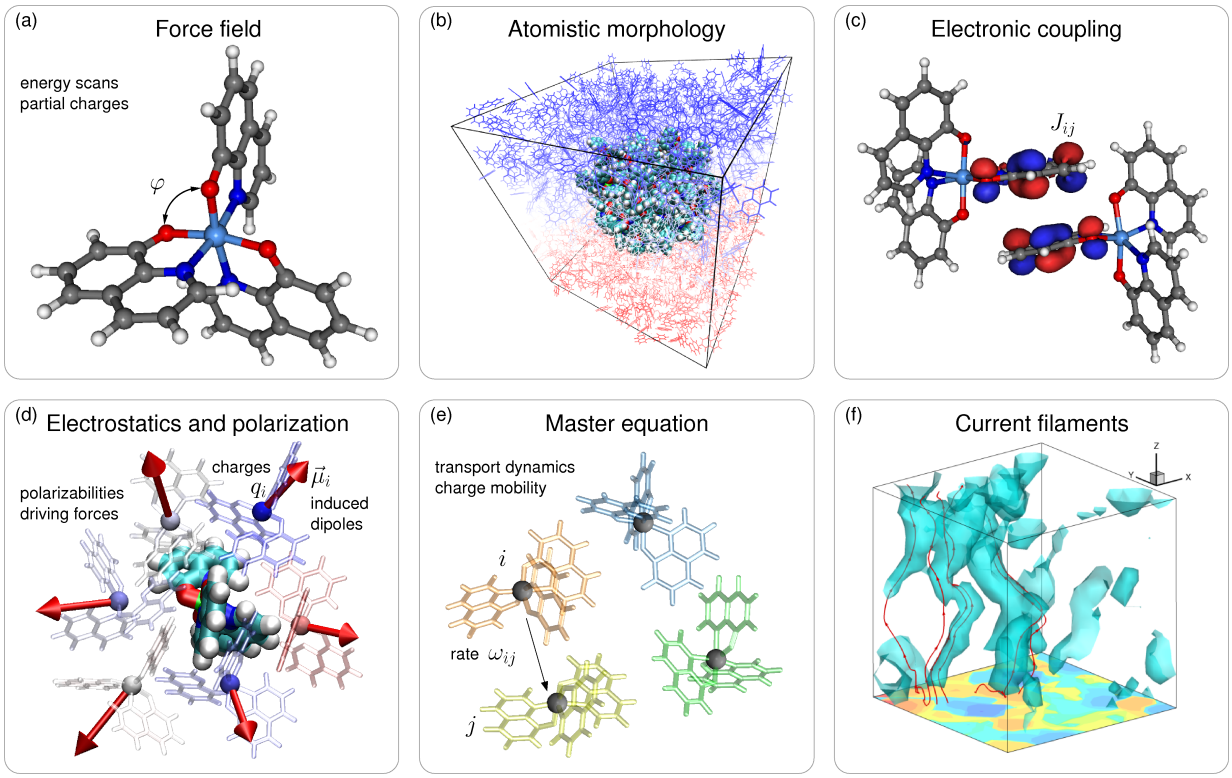


**Figure 1.1.** Essential ingredients of microscopic charge-transport simulations in organic semiconductors shown for the $Alq_3$ molecule. (a) Atomistic force fields are refined using electronic structure techniques. (b) Classical Molecular dynamics simulations allow to predict the morphology at an atomistic level of resolution. (c) Electronic coupling elements between localized states are evaluated using quantum-chemical approaches. (d) Site energies due to electrostatics and polarization are computed using polarizable force field. (e) A directed graph is constructed from charge-transfer rates. (f) Solution of the corresponding master equation allows to visualize microscopic charge currents.

such as charge and energy transfer, span several orders of magnitude. Hence, treatment of the charge motion cannot be achieved with numerical methods using a fixed time step. Instead, a description based on transition rates between localized states, supplemented by charge-transfer theories, is employed. All the ingredients entering the rate expression such as site energies of the localized states and electronic coupling elements between them are calculated using quantum-chemical approaches, classical simulation methods, or their combination. With the rates at hand, one can study charge transport by solving the corresponding differential master equation, e.g. by using the kinetic Monte Carlo method which is capable of simulating charge dynamics of non-steady-state systems. Analyzing charge dynamics thus provides understanding of microscopic processes and helps to formulate chemical design rules.

This thesis is structured as follows: in ch. 2 we describe the workflow of microscopic charge-transport simulations and explain basic concepts behind each method. As an il-

lustration, we study charge transport in an amorphous phase of small molecules which is used as the electron-transporting layer and as the matrix material for the emission layer of a blue OLED. We then apply this microscopic approach in ch. 3 to investigate charge transport in unimolecular and multi-component amorphous phases of small molecules in order to understand physical processes occurring in organic devices based on these systems such as OLEDs and OPVCs. Here, we address the question of how to design a charge-transport efficient host molecule for the emission layer of a deep blue OLED. By analyzing the electronic structure of the frontier orbitals, we show that small delocalization effects lead to large electronic coupling elements and hence improved mobility. In the second part we study charge transport in a host-guest system typically used in the emission layer of a deep blue OLED. We explicitly show that lattice models cannot predict charge transport in these systems because of simplifications used to account for polarization effects in calculation of charge energies. The microscopic approach shows, that the energy landscape for charge transport is very different if these polarization effects are considered on an atomistic scale. In ch. 4 we then discuss one-dimensional charge transport in self-assembled systems which are used for example as molecular wires in OFETs. There, we address the question of how intermolecular packing motives induced by the side chains attached to discotic aromatic cores can increase the charge mobility. We conclude the thesis with a summary and an outlook in ch. 5 describing the challenges for the field.

# Chapter 2

# Microscopic charge-transport simulations

Compound design of organic semiconductors requires in-depth understanding of elementary processes occurring in these materials [40]. In particular, linking the chemical structure to charge dynamics is a non-trivial task, since several factors determine macroscopic quantities such as the charge-carrier mobility: the molecular electronic structure, the relative positions and orientations of neighboring molecules, and spatial inhomogeneities in the morphology, which limit charge carrier pathways on a macroscopic scale [41].

Furthermore, the choice of the model Hamiltonian depends on the specific situation [42], e.g. for perfectly ordered defect-free crystals at low temperatures the Drude model based on band theory [43] or its extensions which account for local electron-phonon coupling [44–46] are often used. At ambient conditions, however, the thermal fluctuations of the transfer integral (electronic coupling) are of the same order of magnitude as its average value and charge transport should be treated as diffusion limited by thermal disorder. This can be achieved using semi-classical dynamics based on a Hamiltonian with interacting electronic and nuclear degrees of freedom [33, 47, 48]. If nuclear dynamics is much slower than the dynamics of charge carriers and electronic coupling is weak, charge transport can be described by a Hamiltonian with static disorder, based on simple assumptions on the electronic density of states and on the hopping rates between localized states.

The latter approach is by now routinely used to study charge transport in amorphous and partially disordered organic semiconductors [31, 49–62] and will also be followed in this thesis. Its key ingredients are material morphology and charge transfer (hopping) rates. The rates depend not only on the molecular electronic structure but are also sensitive to the relative positions and orientations of molecules. Hence, in order to evaluate the rates, the material morphology must be known at an atomistic resolution. This can be achieved by performing molecular dynamics simulations and thus relies on the force-field development for new compounds. If the required time- and length-scales exceed the range available to atomistic molecular dynamics, coarse-graining techniques can be used [63]. These techniques need to be capable of back-mapping the coarse-grained representation to an atomistic resolution.

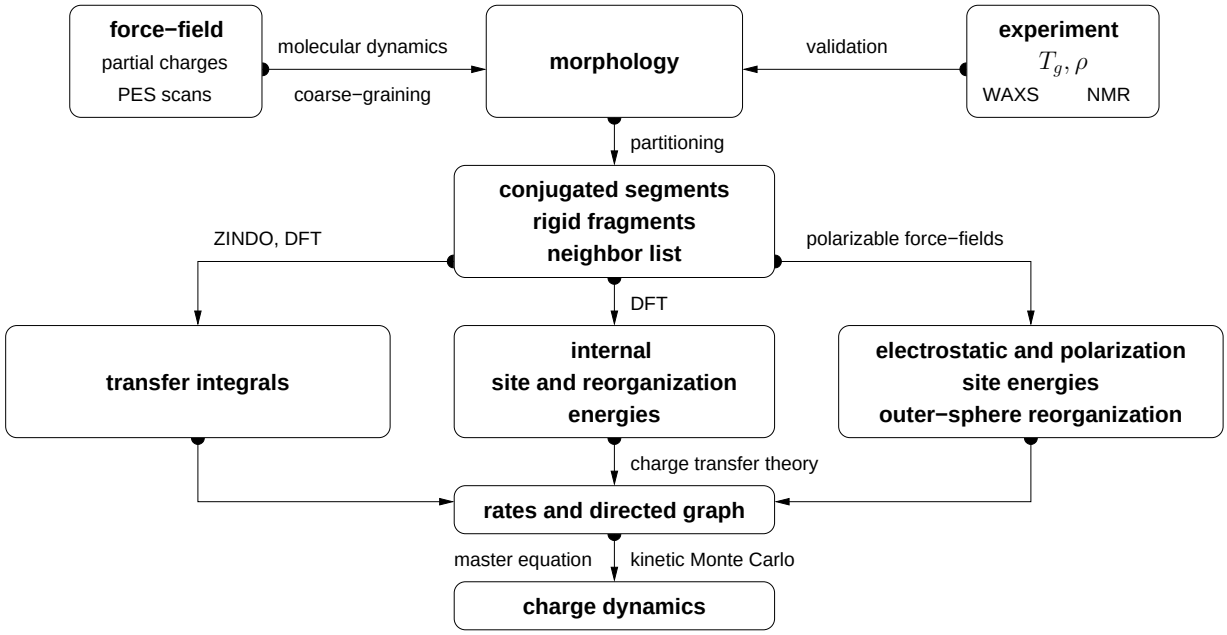


**Figure 2.1.** Workflow for microscopic simulations of charge transport. Ground state geometries, partial charges, and a refined force field are used to simulate atomistically-resolved morphologies (sec. 2.2). After partitioning on conjugated segments and rigid fragments (sec 2.3) a list of pairs of molecules (neighborlist) is constructed. For all pairs Marcus type hopping rates (sec. 2.4) are calculated based on transfer integrals (sec. 2.5), reorganization (sec 2.6) and site energies (sec. 2.7). Eventually, a directed graph is generated and the corresponding master equation is solved using the kinetic Monte Carlo method (sec. 2.8).

Altogether, the task of charge transport characterization is rather tedious and time-consuming to perform, even for a single compound. This is why we have introduced a software package *votca-ctp* (see www.votca.org [64]) which implements a set of techniques for charge-transport simulations, as well as provides a flexible modular platform for their further development. The aim of this chapter is to introduce the fundamental concepts of microscopic charge-transport simulations.

## 2.1 Workflow for charge-transport simulations

The workflow for microscopic charge-transport simulations is depicted in fig. 2.1. The first step is the generation of an atomistic morphology (sec. 2.2) that is partitioned on rigid fragments and conjugated segments representing diabatic states (sec. 2.3). The coordinates of the conjugated segments are used to construct a list of pairs (neighborlist), which reduces the number of charge-transfer rates that have to be calculated. After choosing an expression for the charge transfer rate (sec. 2.4), the involved transport parameters such as transfer integrals (sec. 2.5), reorganization energies (sec. 2.6), and site energies (sec. 2.7) are computed. The neighborlist and charge transfer rates define a directed graph and the

corresponding master equation is solved using the kinetic Monte Carlo method (sec. 2.8). This allows to explicitly monitor the charge dynamics in the system as well as to calculate time- or ensemble averages of occupation probabilities, charge fluxes, and field-dependent mobilities (sec. 2.9).

My personal contributions to the method development lie in the derivation and comparison of rate expressions, the evaluation of inter-molecular reorganization energies, the introduction of conformational disorder in intramolecular reorganization energies and site energies and the inclusion of self-consistent polarization interactions for site energies.

In this chapter, each method is illustrated by studying charge transport in amorphous 2,8-bis(triphenylsilyl)dibenzofurane (BTDF) whose structure is shown in fig. 2.2. This material is used as a matrix material doped with a triplet emitter in the emission layer of a blue organic light emitting diode. A more detailed study of charge transport in pure BTDF and in the mixture with an emitter is presented in ch. 3.

## 2.2 Material morphology

There is no generic recipe on how to predict a large-scale atomistically-resolved morphology of an organic semiconductor. The required methods are system-specific: for ultra-pure crystals, for example, density-functional methods can be used provided the crystal structure is known from experiment. For partially disordered organic semiconductors, however, system sizes much larger than a unit cell are required. Classical molecular dynamics [65] or Monte Carlo techniques [52] are then the methods of choice. Self-assembling materials, such as soluble oligomers, discotic liquid crystals (that we will discuss in ch. 4), block copolymers, partially crystalline polymers, etc., are the most complicated to study. The morphology of such systems often has several characteristic length scales and can be kinetically arrested in a thermodynamically non-equilibrium state. For such systems, the time- and length-scales of atomistic simulations might be insufficient to equilibrate or sample desired morphologies. In this case, systematic coarse-graining can be used to enhance sampling [63]. Note that the coarse-grained representation must reflect the structure of the atomistic system and allow for back-mapping to the atomistic resolution.

In molecular dynamics, Newton's equations of motion, $m_i \frac{\mathrm{d}^2 \vec{r}_i}{\mathrm{d}t^2} = \vec{F}_i$, are integrated for atoms $i$ that are represented by point masses, $m_i$. These interact via forces, $\vec{F}_i = -\vec{\nabla} V_i$, deduced from empirical potentials $V_i$ that are prescribed by a force field. Force fields are parametrized for a limited set of compounds and their refinement is often required for new molecules. In particular, special attention shall be paid to torsion potentials between successive repeat units of conjugated polymers or between functional groups and the $\pi$-conjugated system. First-principles methods can be used to characterize the missing terms of the potential energy surface. The parametrization must take into account existing force field contributions, e.g. due to non-bonded interactions and coupled degrees of freedom should be obtained by using a multidimensional fit. Note that force field validation is as important as its refinement. For instance, X-ray scattering and solid-state NMR provide information about averaged molecular arrangements to which simulation results can be

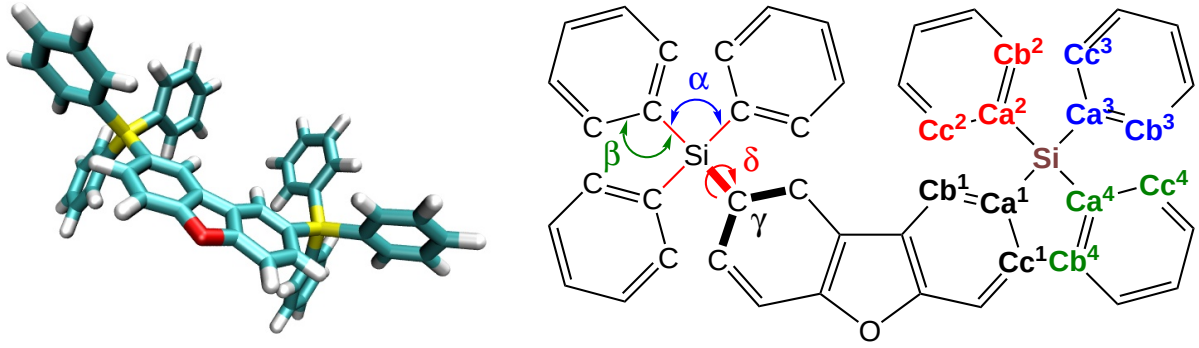


**Figure 2.2.** Chemical structure and atom labels of 2,8-bis(triphenylsilyl)dibenzofurane (BTDF), which is used as the matrix material in the emission layer of blue OLEDs. Unknown degrees of freedom are labeled $\alpha, \beta, \gamma, \delta$ and require definition of atom-types $Ca^1$ to $Cc^4$.

compared. In case of an amorphous morphology, thermodynamic quantities, e.g. density or glass transition temperature can be compared to experiments.

Since we make use of density functional theory not only force field refinement but also for computation of electronic coupling elements, we first introduce the basic concepts ot this electronic structure method.

As an example for force field refinement, we then describe the OPLS force field for BTDF, whose chemical structure is shown in fig. 2.2 together with the degrees of freedom with unknown potential energy surfaces. After force field re-parametrization we will describe the procedure used to generate an amorphous mesophase of BTDF, which is used as the electron transporting layer in an OLED.

### 2.2.1 Density functional theory

According to the fundamental theorems of density functional theory (DFT), the energy of the electronic ground state $E[n]$ of a many-electron system can exactly be determined as a functional of the electron density $n(\vec{r})$. Expressing this density in terms of single-particle wave functions, $n(\vec{r}) = \sum_i^N |\phi_i(\vec{r})|^2$, with $N$ being the number of electrons, allows to derive a set of effective non-interacting single-particle equations (Kohn-Sham) equations. This can be done by means of a variation of $E[n]$ with respect to the density under the condition that the single-particle functions are orthonormal. The resulting single-particle potential comprises the external potential, e.g. the potential of the nuclei, the Coulomb potential of the electron density (Hartree potential), and the exchange-correlation (XC) potential that contains all quantum many-body interactions of electrons. While this representation is formally exact, the exact expression of the exchange-correlation energy functional and the derived potential is unknown except for the case of the free electron gas. Local and semi-local functionals approximate the XC terms via a parametrization of the free electron gas result for the local density and its gradient. A common problem of the available functionals is the fact that the self-interaction of the electrons in the Hartree term is (unlike in Hartree-

Fock theory) not compensated by the exchange-correlation energy or potential. As a consequence of this self-interaction error, the effective potential acting on a single electron is too repulsive and in particular lacks the correct long-range Coulomb behavior, leading to typical errors such as a over-delocalization of electrons and an overestimation of total energies. A general quantification of this error is not possible since it sensitively depends on the characteristics of the electron density, e.g., the error is stronger the more localized a charge is. Note that the analysis of fundamental aspects of DFT and concomitant development of improved self-interaction-free exchange-correlation functionals is a research field on its own.

So called hybrid functionals mix fractions of exact Hartree-Fock exchange and semi-local exchange-correlation to reduce the spurious self-interaction. While the error is not eliminated, these hybrids are found to perform well for organic molecules. Specifically, in our calculations we have used the B3LYP functional, parametrized on a set of atomization energies, ionization potentials, proton affinities, and total atomic energies, for the force field refinement.

In addition to these intrinsic problems of using approximate functionals, another source of error can be attributed to the practical implementation of DFT. Since the effective potential depends on the electron density $n(\vec{r})$, the latter has to be found selfconsistently via the solution of the single-particle Kohn-Sham equations. Therein, the single-particle functions are expanded in a set of appropriate basis functions, the so-called basis set, i.e. $\phi_i(\vec{r}) = \sum_j c_{ij}\eta_j(\vec{r})$. Typically, this basis set consists of atom-centered Gaussian functions of different symmetry (with angular momentum of $l = s, p, d, \dots$) and different spatial localization defined by a decay constant. The more complete this basis set is, the more accurate is the obtained result as a consequence of the variational principle. In practice, in our calculation we have used the 6-311g(p,d) basis set, in which each angular momentum channel of the core electrons (e.g. $1s$ for carbon; $1s$, $2s$, and $2p_{x,y,z}$ for silicon) is represented by a linear combination of 6 primitive Gaussian functions (also referred to as one 6-fold contracted function). Each valence electron channel is described by three basis functions (the first being a 3-fold contracted function, while the other two are just primitive Gaussians). Such a basis set is also called *split valence triple zeta* basis (TZV). Additional polarization functions of higher higher angular momentum $l = p, d$) are added to this set of functions. It has to be made sure that (relative) energies are converged within numerical accuracy with respect to the choice of the basis set.

### 2.2.2 The force field

In classical molecular dynamics, the quantum picture of overlapping electron clouds is transformed into a system of point masses centered at the atoms which interact via effective potentials. Functional forms and parameters for these potentials are summarized in force fields that have to be found by adapting their results to information from quantum chemical calculations, thermodynamic and spectroscopic experimental data or measurement of transport properties. The interactions between atoms can be separated into bonded and non-bonded contributions depending on chemical connectivity. The term bonded refers to

interactions between atoms that are covalently bonded (or linked to one another by one or two bonds) so that these interactions have to be described quantum chemically through effective potentials. The term non-bonded refers to interactions between atoms that are separated by more than a few bonds which allows to model these interactions classically by electrostatic and Lennard-Jones interactions. In the OPLS force field, non-bonded interactions are taken into account between atoms that are separated by more than two bonds and in case of exactly three bonds they are reduced by the factor 1/2 in order to prevent intramolecular strain.

### Non-bonded interactions

In order to include electrostatic interactions by a classical Coulomb sum, the molecular charge distribution is represented by atomistic electrostatic partial charges (ESP). To find these partial charges, the molecular geometry is optimized to find their positions using quantum chemical methods.

The ESP charges are then obtained by fitting the resulting electrostatic potential to the potential arising from the electron density using the Merz-Kollman method [66, 67]. For BTDF the ESP charges are then symmetrized in order to have six identical phenyl rings and a $C_{2v}$ symmetric core without changing the molecular dipole moment of 0.8 D which is directed from the negatively charged oxygen to the center of the furan core.

Apart from electrostatic interactions, the repulsive interaction arising for very short distances between atoms (Pauli repulsion due to overlapping electron orbitals) and the attractive dispersion force due to induced dipoles is modeled by the Lennard-Jones potential. For atom-types $a$ and $b$ separated by a distance $r_{ab}$ this interaction is given by

$$V(r_{ab}) = 4\epsilon_{ab}\left[\left(\frac{\sigma_{ab}}{r_{ab}}\right)^{12} - \left(\frac{\sigma_{ab}}{r_{ab}}\right)^{6}\right]. \tag{2.1}$$

Lennard-Jones parameters $\epsilon_a, \sigma_a$ for atoms of BTDF are taken from the OPLS [68] force field, parameters for silicon and constituents of furane are taken from [69, 70] and Lorentz-Bertelot combination rules, $\epsilon_{ab} = (\epsilon_a\epsilon_b)^{1/2}$ and $\sigma_{ab} = \frac{1}{2}(\sigma_a + \sigma_b)$, are used to describe interactions of different atom-types.

### Bonded interactions

Most bonded interactions are taken from the OPLS [68] force field. Two angular potentials $(\alpha, \beta)$ and two dihedral potentials $(\gamma, \delta)$, introduced in fig. 2.2, are not parametrized in this force field. Their parametrization was performed by doing first principles scans of the corresponding degrees of freedom and then matching the first-principle and force-field potential energy surfaces. We have used density-functional theory (DFT) with the B3LYP hybrid functional and the 6-311g(p,d) basis set for the first-principle calculations. Note that the parametrization takes into account the existing force field contributions, e.g. due to non-bonded interactions [71, 72]. If $q$ is the degree of freedom of interest, *constrained*

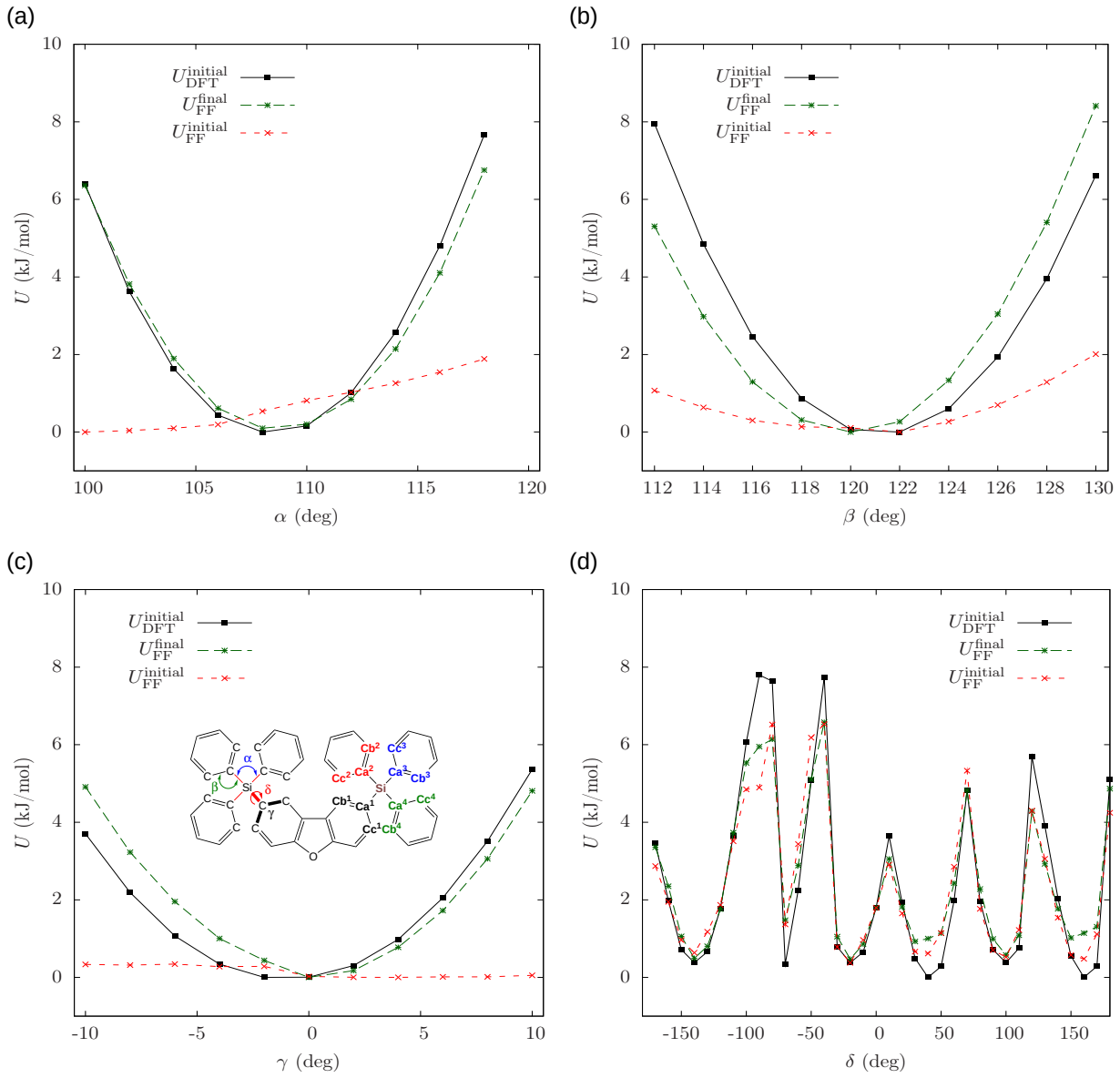


**Figure 2.3.** Force-field scans for the degrees of freedom introduced in fig. 2.2. First-principles scans, $U_{\mathrm{DFT}}$, and final and initial force field scans, $U_{\mathrm{FF}}$, are shown and at room temperature $2.479\mathrm{kJ\,mol^{-1}} = k_{\mathrm{B}}300°\mathrm{K}$. The resulting force field parameters are given in tab. 2.1.

| angle | atom labels | $\theta_0$ (deg) | $k$ (kJ mol$^{-1}$ rad$^{-2}$) |
|---|---|---|---|
| $\alpha$ | C-Si-C | 109.5 | 415 |
| $\beta$ | C-C-Si | 120 | 236 |
| $\gamma$ | Ca$^1$-Cc$^1$-Cb$^1$-Si | 0 | 305 |
| $\gamma$ | Ca$^2$-Cc$^2$-Cb$^2$-Si | 0 | 305 |
| $\gamma$ | Ca$^3$-Cc$^3$-Cb$^3$-Si | 0 | 305 |

| angle | atom labels | $C_1$ | $C_2$ | $C_3$ |
|---|---|---|---|---|
| $\delta$ | Cb$^1$-Ca$^1$-Si-Ca$^2$ | 0.13 | -0.04 | 0.13 |
| $\delta$ | Cb$^2$-Ca$^2$-Si-Ca$^3$ | 0.13 | -0.04 | 0.13 |
| $\delta$ | Cb$^3$-Ca$^3$-Si-Ca$^4$ | 0.13 | -0.04 | 0.13 |
| $\delta$ | Cb$^4$-Ca$^4$-Si-Ca$^1$ | 0.13 | -0.04 | 0.13 |

**Table 2.1.** Parameters for bonded interactions from scans of the potential energy surfaces. Atom labeling is shown in fig. 2.2. Angles $\alpha, \beta, \gamma$ have a quadratical form as shown in eq. 2.2 while the coupled angles $\delta$ are parametrized according to eq. 2.3. Coefficients $C_n$ are given in kJ mol$^{-1}$ (2.479kJ mol$^{-1}$ = $k_\mathrm{B}$300°K).

geometry optimizations are performed using both first-principles and the force-field levels, yielding the total energies $U_{\mathrm{DFT}}(q)$ and $U_{\mathrm{FF}}^{\mathrm{initial}}(q)$, respectively. The missing force field terms are then fitted to this difference using a prescribed functional form. Finally, the constrained geometry optimizations are repeated on the force field level including the obtained potential and $U_{\mathrm{FF}}^{\mathrm{final}}(q)$ is compared to the first-principles scan.

The potentials corresponding to the angles $\alpha$, $\beta$ and the dihedral angle $\gamma$ are fitted using a quadratic form

$$V(\theta) = \frac{1}{2}k(\theta - \theta_0)^2 \quad \text{for} \quad \theta = \alpha, \beta, \gamma\,, \tag{2.2}$$

where we have fixed the equilibrium angles to $(\alpha_0, \beta_0, \gamma_0) = (109.5°, 120°, 0°)$ for symmetry reasons (the same potentials are applied at the four phenyl rings attached to the Si-atom). For the potential corresponding to the dihedral angle $\delta$ we used a periodic functional form

$$V(\delta) = \sum_{n=1}^{3} C_n \cos(3n\delta)\,. \tag{2.3}$$

Here, a multidimensional fit is performed for all eight dihedrals $\delta$ since they are not independent. All fits are shown in fig. 2.3 and the resulting parameters are summarized in tab. 2.1.

### 2.2.3 Molecular dynamics

With the force field at hand, we can generate amorphous mesophases for BTDF. First, 512 BTDF molecules are randomly arranged in a simulation box using the PACKMOL

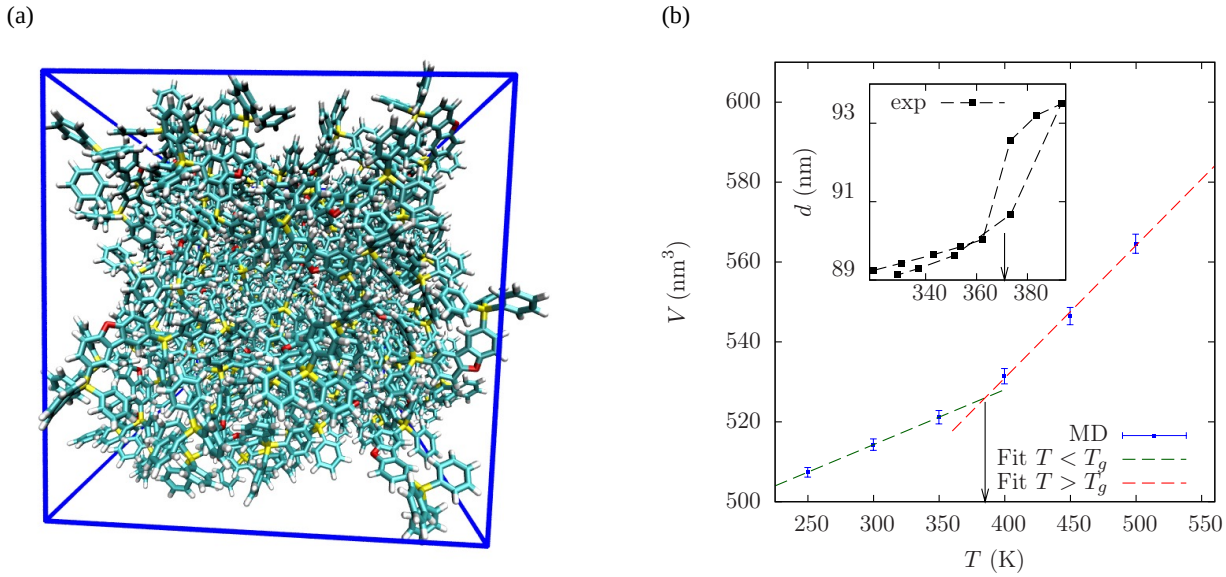


**Figure 2.4.** (a) Periodic simulation box containing 100 BTDF molecules. (b) Simulation of the glass transition in a system of 512 molecules where each data point is taken from a 2 ns MD simulation. Inset shows experimental thickness-temperature dependence for heating and cooling. An estimate for the glass transition temperature is indicated by the arrows.

package [73]. We then anneal the system in an NPT ensemble for 2 ns at 700 K (above the glass transition), until the equilibrium density of a liquid phase of BTDF is reached and molecules become spatially and orientationally uncorrelated, i.e. molecules have moved more than their diameter and the orientational correlation function has decayed to zero. The system is then quenched to room temperature in a time interval of 1 ns and equilibrated for another 0.5 ns before we start the final production with duration of 0.5 ns. This production run is used for the analysis of conformational disorder (see sec. 2.2.4). Charge-transport simulations are based on the morphology from one snapshot of the production run. All simulations are performed using the GROMACS package with a time step of 0.002 ps with constrained bonds using stochastic velocity rescaling for temperature coupling [74] (with a time constant of $\tau_T = 0.07$ ps), Berendsen pressure coupling [75] (reference pressure 1 Bar, time constant of $\tau_P = 2$ ps, and compressibility $4.5 \times 10^{-5}$ Bar$^{-1}$), and the grid-based particle mesh Ewald technique for electrostatic interactions [76]. While double precision accuracy is necessary for the energy minimization for the potential energy scans of isolated molecules (represented in fig. 2.3.b), single precision accuracy is sufficient to prevent instabilities of the morphologies (such as temperature shifts in the NVT ensemble). Note that the error in the observables we use to characterize the morphologies (glass transition temperature and density) due to single precision is small.

The glass transition temperature is estimated from the density-temperature depen-

| | experiment | simulation |
|---|---|---|
| $T_g$ (K) | 371 | 385 |
| $\rho$ (g/cm$^3$) | 1.16 | 1.13 |

**Table 2.2.** BTDF glass transition temperature and density at room temperature.

dence, which is shown in fig. 2.4. Experimental and simulated glass transition temperatures and densities at room temperature are in good agreement with each other as shown in tab. 2.2.

Larger boxes can be generated using the same protocol or can be constructed by connecting periodic images of equilibrated smaller boxes at 700 K and then continuing the annealing process at this temperature for 1 ns. Statistically independent morphologies necessary for error-estimates of charge transport simulations can be obtained by quenching different snapshots (with sufficiently long time intervals) from the 700 K trajectory to room temperature.

### 2.2.4 Conformational disorder

Due to "soft" dihedral potentials with energetic barriers comparable to $k_{\mathrm{B}}T$ (see, e.g., dihedral angle $\delta$ in fig. 2.2) molecules in the amorphous morphology can have different conformations. To show that these conformations are frozen on the timescale of charge transport ( $t_{\mathrm{ct}} \sim$ ps, see high rates in fig. 2.8c that dominate charge dynamics) as well as to identify the soft degrees of freedom, we calculate the time-distribution of the dihedral angles $\alpha_i$, $\beta_i$, $\gamma_i$, and $\delta_i$ for every BTDF molecule $i = 1, \ldots, 4096$ during the $t_{\mathrm{eq}} = 0.5$ ns production run at room temperature. Since the distributions are approximately Gaussian, we further characterize them by a mean $\mu_i$ and a variance $\sigma_i$ for each molecule.

Ensemble-distributions (for all molecules $i$) are then constructed from the means $\mu_i$ and variances $\sigma_i$ as shown in fig. 2.5. As one can see, the dihedral angles $\alpha$, $\beta$, and $\gamma$ have practically identical (narrow) mean and variance with distributions, indicating that their ensemble and time distributions are similar. The ensemble distribution of the mean values of the dihedral angle $\delta$ is, however, very broad. This implies that, in a single snapshot, there are molecules with all possible values of this dihedral angle. At the same time, the ensemble distribution of variances is rather narrow, which tells us that a variation around a particular mean value with time is restricted. In other words, each molecule has its own conformation (determined by the eight dihedral angles $\delta$) which practically does not change during the equilibration run. Note that in fig. 2.5d only the two dihedrals $\delta$ connecting the triphenylsilyl to the dibenzofurane core are considered, the remaining other six dihedrals $\delta$ are also frozen in time but they are evenly distributed. Since fluctuations of the eight individual dihedral angles $\delta$ are small on the time scale $t_{\mathrm{MD}}$, they can be assumed to be frozen on the much faster time scale of charge transport between molecules.

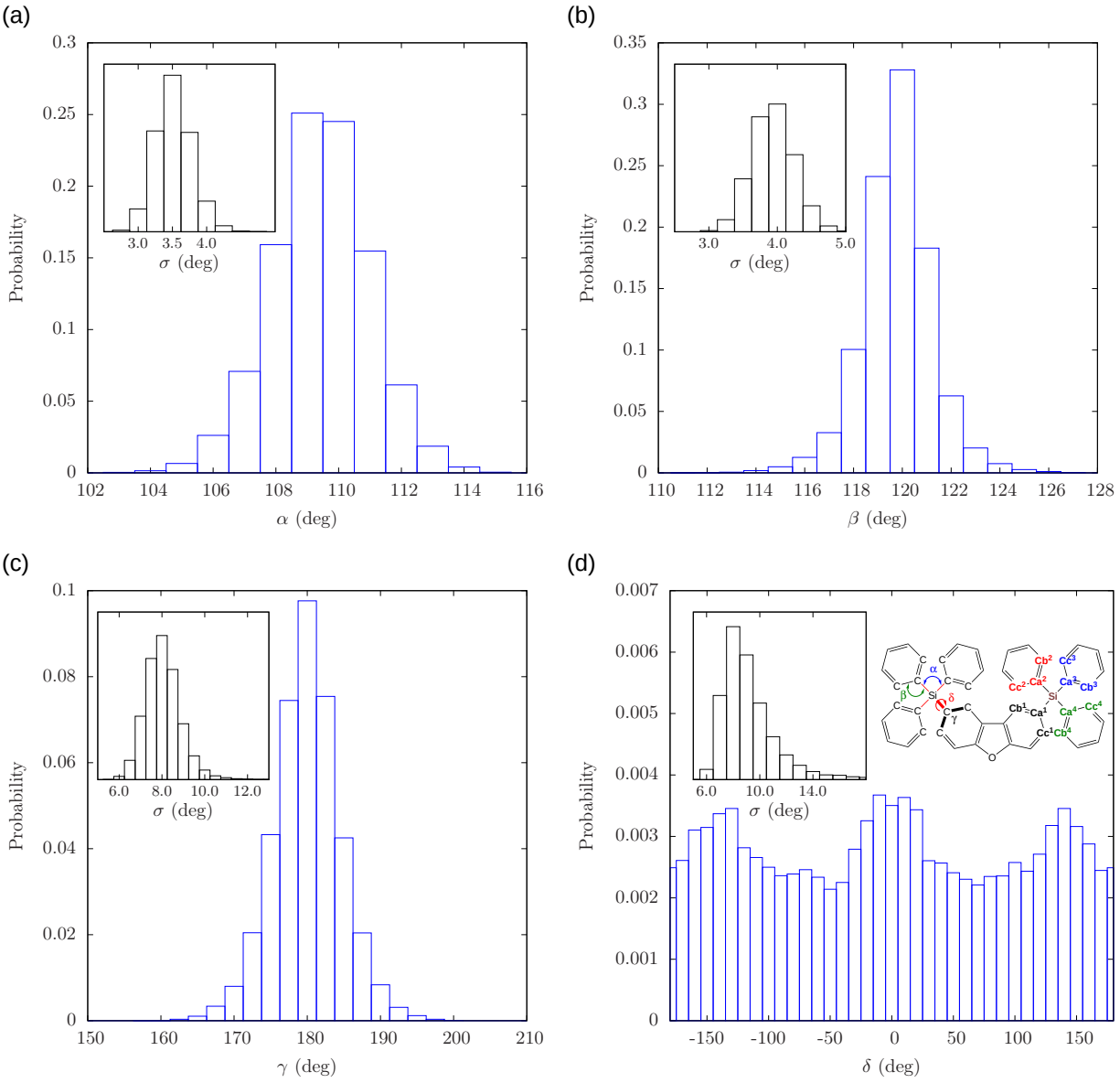


**Figure 2.5.** Ensemble distributions constructed from 4096 mean values of the angles introduced in fig. 2.2 obtained by time-averages over 4096 BTDF molecules. Insets show ensemble-distributions of variances of the corresponding time-distributions. Time distributions are accumulated during a production run of 0.5 ns. The eight dihedral angles $\delta$ are the only soft degree of freedom since in one snapshot molecules can have all possible values of this dihedral angle (see text for more details). Here we show only distributions of one of the dihedrals $\delta$ indicated in red in the inset of (d) since the other dihedrals $\delta$ are homogeneously distributed.

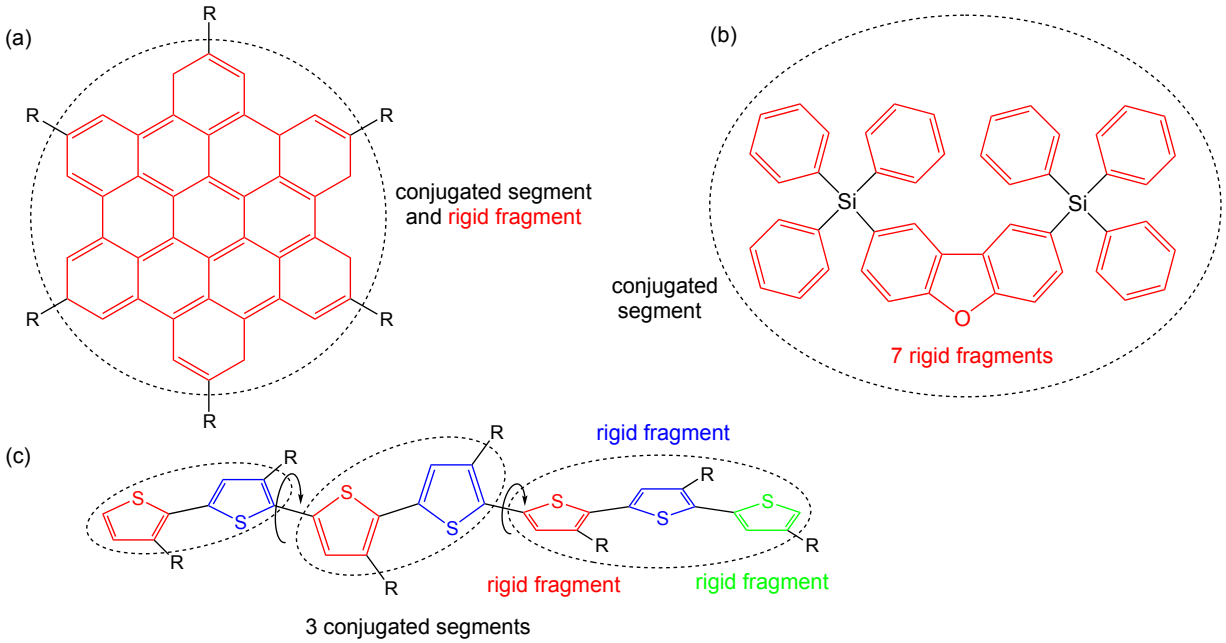


**Figure 2.6.** The concept of conjugated segments and rigid fragments. Dashed lines indicate conjugated segments while colors denote rigid fragments. (a) Hexabenzocoronene: the $\pi$-conjugated system is both a rigid fragment and a conjugated segment. (b) Bis(triphenylsilyl)dibenzofurane (BTDF): The dibenzofurane core and each of the phenyl rings is a rigid fragments while the whole molecule is a conjugated segment. (c) Polythiophene: each repeat unit is a rigid fragment. A conjugated segment consists of one or more rigid fragments. One molecule can have several conjugated segments.

## 2.3 Conjugated segments and rigid fragments

With the morphology at hand, the next step is the construction of the effective electronic Hamiltonian of the system. In a static disorder approximation, this is equivalent to partitioning the system on hopping sites, or conjugated segments that represent diabatic states and calculating charge transfer rates between them. Physically intuitive arguments can be used for the partitioning, which reflects the localization of the wave function of a charge. For most organic semiconductors, the molecular architecture includes relatively rigid, planar $\pi$-conjugated systems, which we will refer to as rigid fragments. A conjugated segment can contain one or more of such rigid fragments, which are linked by bonded degrees of freedom. The dynamics of these degrees of freedom evolves on time scales much slower than the frequency of the internal promoting mode. In some cases, e.g. glasses, it can be 'frozen' due to non-bonded interactions with the surrounding molecules.

To illustrate the concept of conjugated segments and rigid fragments, three representative molecular architectures are shown in fig. 2.6. The first one is a typical discotic liquid crystal, hexabenzocoronene. It consists of a conjugated core to which side chains are attached to aid self-assembly and solution processing. In this case the orbitals localized on

side chains do not participate in charge transport and the conjugated $\pi$-system is both, a rigid fragment and a conjugated segment.

In BTDF the individual phenyl rings and the dibenzofurane cores are relatively rigid, while energies of the order of $k_{\mathrm{B}}T$ are sufficient to reorient them with respect to each other. Thus the phenyl rings and the core are the seven rigid fragments of the BTDF molecule which is one conjugated segment since the charge delocalizes over the entire molecule.

In the case of a conjugated polymer, one molecule can consist of several conjugated segments, while each backbone repeat unit is a rigid fragment. Since the conjugation along the backbone can be broken due to large out-of-plane twists between two repeat units, an empirical criterion, based on the dihedral angle, can be used to partition the backbone on conjugated segments [59]. However, such intuitive partitioning is, to some extent, arbitrary and shall be validated by other methods [77–79].

After partitioning, an additional step is often required to remove bond length fluctuations introduced by molecular dynamics simulations, since they are already integrated out in the derivation of the rate expression. This is achieved by substituting respective molecular fragments with rigid, planar $\pi$-systems optimized using first-principles methods. Centers of mass and gyration tensors are used to align rigid fragments, though a custom definition of local axes is also possible. Such a procedure also minimizes discrepancies between the first-principles-based ground state geometries of conjugated segments as compared to their geometries in the snapshot of the MD simulation. We have quantified the effect of this substitution on transfer integrals in the amorphous phase of the $\mathrm{Alq_3}$ molecule by comparing distributions of the integrals obtained from geometries of the MD snapshot to distributions obtained with the substituted rigid fragments but have found that both lead to the same mobility (within the error bars of the charge transport simulation).

Finally, a list of neighboring conjugated segments is constructed. Two segments are added to this list if the distance between centers of mass of *any* of their rigid fragments is below a certain cutoff. This allows neighbors to be selected on a criterion of minimum distance of approach rather than center of mass distance, which is useful for molecules with anisotropic shapes. The cutoff for the neighborlist has to be sufficiently large to converge macroscopic charge transport properties. In case of BTDF a neighborlist cutoff of $r_{\mathrm{nb}} = 0.7\mathrm{nm}$ between the seven rigid fragments introduced in fig. 2.6b leads to 30.000 pairs in a cubic simulation box of 4096 molecules with box-length of $L = 16\mathrm{nm}$ and is sufficient to converge the mobility as discussed in sec. 2.9.4. We will therefore use this neighborlist for the remainder of this chapter.

## 2.4 Charge-transfer rates

Typical time scales of charge transfer in disordered organic semiconductors span several orders of magnitude as shown in fig. 2.8.c for charge transport in amorphous mesophases of BTDF. Hence, treatment of charge kinetics cannot be achieved with numerical methods using a fixed time step. Instead, a description based on charge-transfer rates between localized states has to be employed. In an amorphous morphology, electronic couplings be-

tween neighboring molecules are weak and hence charges are localized on entire molecules. Intermolecular charge transfer (i.e. for electron transport $M_i^- + M_j \rightarrow M_i + M_j^-$) then occurs between molecules $i$ and $j$ which form the charge-transfer complex. In this section we discuss different rate-expressions that can be used for the description of charge transport in organic semiconductors.

### 2.4.1 Miller-Abrahams rate

Rate-expressions for charge transfer can be postulated based on intuitive physical considerations, as it is done for example in the Gaussian disorder models (GDM) [21, 34, 37, 80], where the hopping sites are distributed on a discrete lattice. In these models, Miller-Abrahams rates [81] describing phonon-assisted tunneling are used

$$\omega_{ij} = \nu_0 \left\{ \begin{array}{rcl} \exp\left(-2\gamma_{ij} r_{ij} + \frac{\Delta E_{ij}}{k_\mathrm{B} T}\right) & : & \Delta E_{ij} = E_i - E_j \geq 0 \\ \exp\left(-2\gamma_{ij} r_{ij}\right) & : & \Delta E_{ij} = E_i - E_j \leq 0 \end{array} \right) . \tag{2.4}$$

Here $\omega_{ij}$ is the rate for the charge to be transferred from state $i$ to state $j$, $\nu_0$ is a material specific rate constant, $r_{ij}$ is the distance between localized states and $\gamma_{ij}$ is an inverse localization radius describing the decay of transfer integrals (electronic coupling elements) $J_{ij}$ with the separation according to $J_{ij}^2 = \exp(-2\gamma_{ij} r_{ij})$. Furthermore, $k_\mathrm{B}$ is Boltzmann's constant, $T$ the temperature, and $\Delta E_{ij}$ is the site-energy difference (driving force), so that a hop uphill $\Delta E_{ij} > 0$ (endothermic hopping) is energetically unfavorable.

The GDM can be used to understand the qualitative influence of parameters such as the width of the site-energy distribution (diagonal disorder) or disorder in electronic coupling elements (off-diagonal disorder) on the mobility. In order to do this, charge transport is simulated for one carrier on the discrete lattice with site-energies randomly drawn from a Gaussian distribution of width $\bar{\sigma}$. Transfer integrals are described by two site-specific contributions $\gamma_{ij} = \gamma_i + \gamma_j$ each varying randomly according to a Gaussian distribution of width $\bar{\sigma}_\gamma$ so that the variance of the transfer integrals is $\Sigma = \sqrt{2}\bar{\sigma}_\gamma$. This allows to extract an empirical relation for the mobility [21] given by

$$\mu(F,T) = \mu_0 \exp\left[ -\left(\frac{2\bar{\sigma}}{3 k_\mathrm{B} T}\right)^2 + C\left\{ \left(\frac{\bar{\sigma}}{k_\mathrm{B} T}\right)^2 - \Sigma^2 \right\} \sqrt{F} \right] \tag{2.5}$$

where $\mu_0$ and $C$ are constants and $F$ is the electric field. Comparing the mobility as a function of electric field and temperature for various combinations of the parameters $\nu_0, \bar{\sigma}, \Sigma$ to experimental data allows to estimate the diagonal and off-diagonal disorder in organic semiconductors. Although eq. 2.4 includes some of the key parameters such as transfer integrals and site-energy differences, the main disadvantage of the Miller-Abrahams rate lies in the fact that experimental data is necessary for its parametrization, and therefore it cannot be used to predict mobilities.

### 2.4.2 Charge-transfer theories

Alternatively, charge-transfer theories can be used to evaluate rates from quantum-chemical calculations [20, 32, 51, 82–84]. In spite of being significantly more computationally demanding, they allow to link the chemical and electronic structure, as well as the morphology, to charge dynamics and, in principle, provide a route for predicting charge transport without experimental input. In the following subsections, we will compare different rate expressions that fulfill this criterion and pay special attention to their applicability for charge transport in disordered organic semiconductors.

#### Marcus rate

The simplest rate expression is the high temperature limit of classical charge-transfer theory [85, 86], where the transfer rate for a charge to hop from a state $i$ to a state $j$ reads

$$\omega_{ij} = \frac{2\pi}{\hbar} \frac{J_{ij}^2}{\sqrt{4\pi\lambda_{ij} k_\mathrm{B} T}} \exp\left[ -\frac{(\Delta E_{ij} - \lambda_{ij})^2}{4\lambda_{ij} k_\mathrm{B} T} \right] . \tag{2.6}$$

As in eq. 2.4 rate parameters are $\Delta E_{ij}$, the site-energy difference and $J_{ij}$, the electronic coupling element. An additional parameter in the Marcus theory is the reorganization energy $\lambda_{ij}$ that accounts for relaxation of nuclear coordinates after charge transfer. It has two contributions $\lambda_{ij} = \lambda_{ij}^{\mathrm{int}} + \lambda_{ij}^{\mathrm{out}}$ from degrees of freedom inside the charge-transfer complex consisting of states $i$ and $j$ (internal, or intramolecular reorganization of donor and acceptor) and from outside (outer-sphere reorganization), both terms are described in sec. 2.6.

The first assumption in eq. 2.6 is that charge transport occurs between initial and final *diabatic* states [19]. These states correspond to the charge being localized on the donor molecule in the initial state (while the acceptor is neutral), and vice versa for the final state. In other words, the time for the electronic wave function to move from donor to acceptor, $\tau_{\mathrm{el}} = \hbar/J$ is much larger compared to the time for nuclear motion of the promoting mode $\tau_{\mathrm{nuc}} = 2\pi/\omega_{\mathrm{vib}}$, where typically $\omega_{\mathrm{vib}} = 0.2\mathrm{eV}$. In this case Fermi's golden rule can be applied and the rate is found from a first order perturbation of the diabatic states with respect to the electronic coupling, which explains the prefactor $J_{ij}^2$ in eq. 2.6. In case of BTDF typically $J < 1\,\mathrm{meV}$ so that the condition of non-adiabaticity is certainly fulfilled. Note that we have indicated the diabatic states with solid lines in fig. 2.7a, while the adiabatic states (where the charge would be delocalized in case of strong electronic coupling) are dashed red.

The second assumption in the derivation of eq. 2.6 lies in the fact that all promoting modes are harmonic and can be treated classically. Thermal averaging over these classical modes of nuclear motion with mass weighted coordinate $q$ and vibrational energy $\frac{1}{2}\omega^2 q^2$ leads to the remaining part of the prefactor and the Boltzmann term so that $\omega_{ij} \sim J^2 \exp[-E_{\mathrm{act}}/(k_\mathrm{B}T)]$ with activation energy $E_{\mathrm{act}}$. The latter depends on site-energy difference and reorganization energy and corresponds to the energy difference from the groundstate of the initial diabatic state to the crossing point with the final diabatic

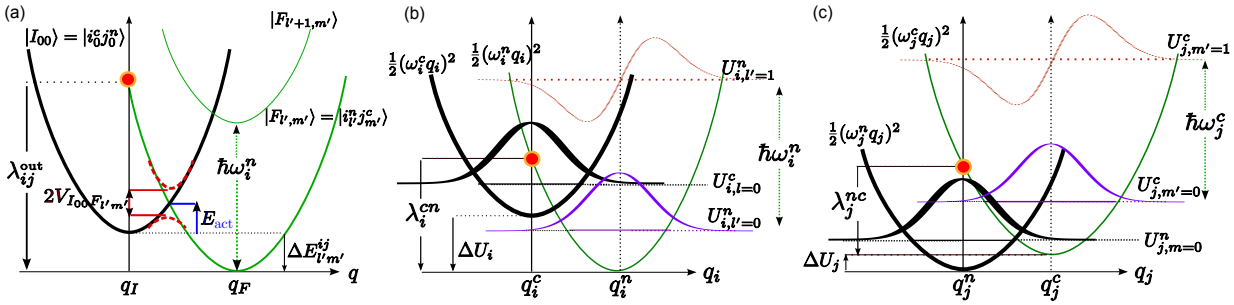


**Figure 2.7.** (a) Potential energy surfaces of the charge-transfer complex in a dimer representation (transfer is from initially charged molecule $i$ to molecule $j$). In the initial state (black), $|I_{00}\rangle$, both molecules are in their vibrational ground states. In the final state (green), $|F_{l'm'}\rangle$, the neutral molecule $i$ is in vibrational state $l'$, while the charged molecule $j$ is in vibrational state $m'$. Initial and final states are coupled to a classical harmonic outer-sphere normal mode with mass weighted average coordinate $q$ and reorganization energy $\lambda_{ij}^{\text{out}}$. Together with the energy offset $\Delta E_{l'm'}^{ij}$ between initial and final state it results in the activation energy $E_{\text{act}}$. For small couplings $V_{I_{00}F_{l'm'}}$ the ET reaction occurs between diabatic states where the charge is initially(finally) localized on molecule $i(j)$ (solid curves) as opposed to delocalized adiabatic states (dotted red). (b) PES of molecule $i$ as a function of the averaged normal internal mode $q_i$. $l$ and $l'$ enumerate vibrational modes of the initial charged and the final neutral states. (c) Same as (b) for initially neutral molecule $j$. $\Delta U_i$ ($\Delta U_j$) is the internal energy difference while $\lambda_i^{cn}$ ($\lambda_j^{nc}$) is the intramolecular reorganization energy for discharging molecule $i$ (charging molecule $j$).

state since we have performed first order perturbation theory. If only the harmonic outer sphere mode is treated classically, $E_{\text{act}} = \frac{\left(\Delta E_{ij} - \lambda_{ij}^{\text{out}}\right)^2}{4\lambda_{ij}^{\text{out}}}$ can be deduced from fig. 2.7a, with $\lambda_{ij}^{\text{out}} = \frac{1}{2}\omega_{\text{out}}^2 |q_I^2 - q_F^2|$. If modes of donor and acceptor are also treated classically, their internal site-energy differences, e.g. due to molecular (dis)charging energies, and their intramolecular reorganization energies can be added to those of the environment when computing $E_{\text{act}}$ [19] (see fig. 2.7b, c for definition of these intramolecluar contributions).

While the outer-sphere mode (corresponding to slow reorientation of the molecules surrounding the charge-transfer complex) can indeed be treated classically, this is not true for the intramolecular promoting modes, which roughly correspond to C-C bond stretching [82] so that their vibrational energy is $\hbar\omega^{\text{int}} \approx 0.2\,\text{eV} \gg k_{\text{B}}T$ and they should be treated quantum-mechanically at ambient conditions. Furthermore, the weak interactions between the molecules imply that each molecule has its own, practically independent, set of quantum-mechanical degrees of freedom so that also just adding the intramolecular energies of molecules $i$ and $j$ is problematic. To overcome these limitations, we have developed a more rigorous rate equation as presented in the next section. Note that the derivation becomes rather technical, so that the fast reader should directly go to the next subsection, where we discuss a special case of the bimolecular rate known as the Levich-Jortner rate and to the subsection thereafter, where we compare the three rates of this section.

**Bimolecular electron-transfer rate**

During a bimolecular electron-transfer reaction the electron moves between two molecules with decoupled nuclear degrees of freedom. Therefore, one needs separate sets of coordinates for the donor and acceptor. If the independent vibrational modes of molecule $i$ and $j$ are harmonic, are treated classically, and the charging ($\lambda_i^{\rm nc}$) and discharging reorganization energies ($\lambda_i^{\rm cn}$) of the same molecule are identical ($\lambda_i^{\rm nc} = \lambda_i^{\rm cn}, \lambda_j^{\rm nc} = \lambda_j^{\rm cn}$ see sec. 2.6), one still obtains the Marcus-type rate expression (eq. 2.6) with the intramolecular reorganization energy $\lambda_{ij}^{\rm int} = \lambda_i^{\rm cn} + \lambda_j^{\rm nc}$ which is the sum of the reorganization energies of discharging the donor and charging the acceptor [19]. Similarly, the classical treatment of the outer-sphere mode allows to add its reorganization energy to the intramolecular contribution.

If the high-frequency intramolecular vibrational modes of molecules $i$ and $j$ are treated quantum-mechanically but in a common set of vibrational coordinates and an outer-sphere low-frequency (classical) vibrational coordinate is also considered, a mixed quantum-classical multi-channel generalization of the Marcus formula, the Levich-Jortner rate [19], is available as a special case of the derivation and is presented later (eq. 2.15).

Following Ref. [82] we assume that all intramolecular modes of a donor $i$ can be averaged into a single mode with mass weighted coordinate $q_i$ and energy $\hbar\omega_i^n$ ($\hbar\omega_i^c$) for the molecule in a neutral (charged) state (for readability, we omit the superscript $\omega^{\rm int}$ for these intramolecular modes). Similar assumptions are made for the acceptor $j$. In addition, we allow for an averaged classical outer-sphere mode with mass weighted coordinate $q$ and energy $\hbar\omega_{ij}^{\rm out} \ll k_{\rm B}T$. This mode is common to both molecules and plays the role of the reaction coordinate for electron transfer. In a more general case the curvature of the potential energy surface (PES) of this mode might change depending on whether molecule $i$ or $j$ is charged, i.e. $\omega_{ij}^{\rm out} \neq \omega_{ji}^{\rm out}$ and thus $\lambda_{ij}^{\rm out} \neq \lambda_{ji}^{\rm out}$. If the difference is large one has to combine our derivation with the argument of Ref. [87].

In amorphous organic semiconductors the electronic coupling is usually small compared to both the energy of the classical vibrational mode and intermolecular reorganization energies. In this case the initial, $|I_{lm}\rangle$, and final, $|F_{l'm'}\rangle$, states of the ET reaction are diabatic (non-interacting) dimer states which depend on the vibrational states with quantum numbers $l, l'$ for molecule $i$ and $m, m'$ for molecule $j$ respectively. The potential energy surfaces (PES) corresponding to these states are shown in fig. 2.7a as a function of the common outer-sphere reaction coordinate $q$. The PES for intramolecular degrees of freedom for molecules $i$ and $j$ are shown in fig. 2.7b and c, respectively.

For the contributions of the classical outer-sphere mode to initial and final states we introduce Hamilton functions

$$H_{I,F}(q) = \frac{1}{2}\left[\omega^{\rm out}\left(q - q_{I,F}\right)\right]^2 , \tag{2.7}$$

where the equilibrium position in the initial (final) state $q_I$ ($q_F$) corresponds to the arrangement of all nuclear coordinates of molecules surrounding the ET complex when molecule $i$ ($j$) is charged. The outer-sphere reorganization energy, defined as $\lambda_{ij}^{\rm out} = \frac{1}{2}\left[\omega^{\rm out}|q_I - q_F|\right]^2$, is shown in fig. 2.7a. It can be computed from the initial and final electric displacement fields of the charge-transfer complex as explained in sec. 2.6.

The complete Hamiltonian of the ET complex can now be written as

$$\begin{aligned} H_{ij} = & \sum_{l,m=0}^{\infty} \left(H_I(q) + E_{lm}^{ij}\right) |I_{lm}\rangle\langle I_{lm}| + \sum_{l',m'=0}^{\infty} \left(H_F(q) + E_{m'l'}^{ji}\right) |F_{l'm'}\rangle\langle F_{l'm'}| \\ & + \sum_{l,m,l',m'} V_{I_{lm}F_{l'm'}} |I_{lm}\rangle\langle F_{l'm'}| + \text{h.c}\,, \\ E_{lm}^{ij} = & \; U_i^{cC} + U_j^{nN} + E_i^{\text{el}} + E_i^{\text{ext}} + \hbar\left[\omega_i^c\left(l+\frac{1}{2}\right) + \omega_j^n\left(m+\frac{1}{2}\right)\right], \\ E_{m'l'}^{ji} = & \; U_j^{cC} + U_i^{nN} + E_j^{\text{el}} + E_j^{\text{ext}} + \hbar\left[\omega_j^c\left(m'+\frac{1}{2}\right) + \omega_i^n\left(l'+\frac{1}{2}\right)\right]. \end{aligned} \tag{2.8}$$

Here, a manifold of initial states, $|I_{lm}\rangle$, with quantum numbers $l$ ($m$) for intramolecular vibrations in molecule $i$ ($j$) and energy $E_{lm}^{ij}$, is coupled to a classical phonon bath $H_I(q)$. Transitions to the manifold of final states $|F_{l'm'}\rangle$ where the charge has hopped from $i$ to $j$ are possible due to a coupling $V_{I_{lm}F_{l'm'}}$. The initial, $E_{lm}^{ij}$, and final, $E_{m'l'}^{ji}$, energies contain internal energies $U_i^{nN}$ and $U_i^{cC}$ ($U_j^{nN}$ and $U_j^{cC}$) of molecule $i$ (molecule $j$) in the neutral and charged ground states, the contributions of electrostatic interactions, $E_i^{\text{el}}$ and $E_j^{\text{el}}$, the external electric field, $E_i^{\text{ext}}$ and $E_j^{\text{ext}}$, and finally respective oscillator energies.

Within the Born-Oppenheimer approximation, a separation in terms of electronic and nuclear degrees of freedom gives

$$\begin{aligned} |I_{lm}\rangle &= |\phi_i^c\rangle|\chi_{il}^c\rangle|\phi_j^n\rangle|\chi_{jm}^n\rangle\,, \\ |F_{l'm'}\rangle &= |\phi_i^n\rangle|\chi_{il'}^n\rangle|\phi_j^c\rangle|\chi_{jm'}^c\rangle\,, \end{aligned} \tag{2.9}$$

where $\phi_i^n$ ($\phi_i^c$) corresponds to the electronic part of the wave function, while $\chi_{il}^n$ ($\chi_{il}^c$) represents an $l$-th phonon mode of the neutral (charged) molecule $i$.

The coupling element $V_{I_{lm}F_{l'm'}}$ in eq. 2.8 can then be factorized in an electronic and nuclear parts

$$V_{I_{lm}F_{l'm'}} = J_{ij}\langle\chi_{il}^c|\chi_{il'}^n\rangle\langle\chi_{jm}^n|\chi_{jm'}^c\rangle\,. \tag{2.10}$$

The calculation of the electronic part $J_{ij}$ is explained in more detail in sec. 2.5. Franck-Condon overlap integrals $\langle\chi_{il}^c|\chi_{il'}^n\rangle$ ($\langle\chi_{jm}^n|\chi_{jm'}^c\rangle$) describe couplings of vibrational modes $l, l'$ ($m, m'$) of the charged and neutral configurations of molecule $i$ ($j$). Exemplary modes are shown in fig. 2.7b,c.

Since $k_{\text{B}}T \ll \hbar\omega_i^c, \hbar\omega_j^n$ one can restrict the initial state to the vibrational ground-states $l = m = 0$ while allowing tunneling to all vibrationally excited states $l'$ for molecule $i$ and $m'$ for molecule $j$. In other words, a single initial state $|I_{00}\rangle$ couples to a manifold of final states $|F_{l',m'}\rangle$. This assumes that ET is sufficiently slow compared to the relaxation of the intramolecular degrees of freedom, so that there is enough time for a complex to relax to its vibrational ground state between two consecutive ETs.

The energy difference driving the reaction from the ground state to channel $l'm'$ therefore is

$$\Delta E_{l'm'}^{ij} = E_{00}^{ij} - E_{m'l'}^{ji} = \Delta E_{ij} - \hbar(\omega_i^n l' + \omega_j^c m')\,,$$

where $\Delta E_{ij} = \Delta E_{ij}^{\rm ext} + \Delta E_{ij}^{\rm el} + \Delta E_{ij}^{\rm int}$ as explained in sec. 2.7.

Assuming that $|V_{I_{00}F_{l'm'}}| \ll \lambda_{ij}^{\rm out}, \hbar\omega^{\rm out}$ and using Fermi's golden rule with $V_{I_{00}F_{l'm'}}$ as a perturbation to the initial diabatic state, we obtain a multi-channel rate equation

$$\omega_{ij} = \sum_{l',m'=0}^{\infty} \frac{2\pi}{\hbar} |V_{I_{00}F_{l'm'}}|^2 \int dq f_I(q) \delta(\Delta E_{l'm'}^{ij} + H_I(q) - H_F(q)) \,, \tag{2.11}$$

where the thermal averaging over the classical outer-sphere mode is performed by introducing a canonical distribution function $f_I(q) = Z^{-1} \exp(-H_I(q)/k_{\rm B}T)$, with the partition function $Z = \int dq \exp(-H_I(q)/k_{\rm B}T)$. Energy conservation pins the transition to the crossing point of the diabatic PES (see fig. 2.7a) resulting in

$$\begin{aligned} \omega_{ij} = \quad & \frac{2\pi}{\hbar} \frac{|J_{ij}|^2}{\sqrt{4\pi\lambda_{ij}^{\rm out} k_{\rm B}T}} \sum_{l',m'=0}^{\infty} |\langle \chi_{i0}^c | \chi_{il'}^n \rangle|^2 |\langle \chi_{j0}^n | \chi_{jm'}^c \rangle|^2 \\ \times \quad & \exp\left\{ - \frac{\left[\Delta E_{ij} - \hbar(l'\omega_i^n + m'\omega_j^c) - \lambda_{ij}^{\rm out}\right]^2}{4\lambda_{ij}^{\rm out} k_{\rm B}T} \right\}. \end{aligned} \tag{2.12}$$

Eq. 2.12 is the quantum-classical expression for the bimolecular ET rate with two independent, high-frequency vibrational modes and one classical common outer-sphere mode. This rate expression is the main result of this section and indicates that the rate has to be computed by summing over all transitions from the initial diabatic groundstate to excited final states characterized by vibrational quanta $l'$ and $m'$ of donor and acceptor. As we have used Fermi's golden rule, the transition rate for each of these channels is proportional to the squared coupling element between initial and final state including an electronic term $J_{ij}$ and nuclear Franck-Condon factors of donor and acceptor. Thermal averaging over the classical outer sphere mode of the environment leads to the Boltzmann term where the activation energy $E_{\rm act}$ is depicted in fig. 2.7a. It includes the effect of different initial and final site energies $\Delta E_{ij}$ (for example due to different electrostatic environments of donor and acceptor), the vibrational energies in the final donor and acceptor state (the initial state is assumed to be the groundstate) and the relaxation of the environment given by the reorganization energy $\lambda_{ij}^{\rm out}$.

If the curvatures of intramolecular PES of charged and neutral states of a molecule are different, that is $\omega_i^c \neq \omega_i^n$, the corresponding reorganization energies, $\lambda_i^{cn} = \frac{1}{2}[\omega_i^n(q_i^n - q_i^c)]^2$ and $\lambda_i^{nc} = \frac{1}{2}[\omega_i^c(q_i^n - q_i^c)]^2$, will also differ. In this case the Franck-Condon (FC) factors for discharging of molecule $i$ that was initially in the vibrational ground state $l = 0$ are given by [88]

$$|\langle \chi_{i0}^c | \chi_{il'}^n \rangle|^2 = \frac{2}{2^{l'} l'!} \frac{\sqrt{\omega_i^c \omega_i^n} \exp\left(-|s_i|\right)}{(\omega_i^c + \omega_i^n)} \left[ \sum_{\substack{k=0 \\ k \,\text{even}}}^{l'} \binom{l'}{k} \left( \frac{2\omega_i^c}{\omega_i^c + \omega_i^n} \right)^{k/2} \frac{k!}{(k/2)!} H_{l'-k}\left( \frac{s_i}{\sqrt{2S_i^{cn}}} \right) \right]^2 , \tag{2.13}$$

where $H_n(x)$ is a Hermite polynomial, $s_i = \frac{2\sqrt{\lambda_i^{nc}\lambda_i^{cn}}}{\hbar(\omega_i^c+\omega_i^n)}$, and $S_i^{cn} = \lambda_i^{cn}/\hbar\omega_i^c$. The FC factors for charging of molecule $j$ can be obtained by substituting $(s_i, S_i^{cn}, \omega_i^c)$ with $(-s_j, S_j^{nc}, \omega_j^n)$. In order to evaluate the FC factors, the internal reorganization energy $\lambda_i^{cn}$ can be computed from the intramolecular PES as explained in sec. 2.6.

### Levich-Jortner rate

If identical curvatures in charged and neutral state are assumed, i.e. $\omega_i^c = \omega_i^n = \omega_i$, which implies $\lambda_i^{nc} = \lambda_i^{cn} = \lambda_i$, the Franck-Condon factor simplifies to

$$|\langle\chi_{i0}|\chi_{il'}\rangle|^2 = \frac{1}{l'!}\left(\frac{\lambda_i}{\hbar\omega_i}\right)^{l'} \exp\left(-\frac{\lambda_i}{\hbar\omega_i}\right) . \tag{2.14}$$

If this is true for both donor and acceptor molecules, eq. 2.12 becomes identical to the quantum-classical Levich-Jortner rate expression [19] with $\lambda_{ij}^{\text{int}} = \lambda_i + \lambda_j$ and

$$\begin{aligned} \omega_{ij} = \quad & \frac{2\pi}{\hbar}\frac{|J_{ij}|^2}{\sqrt{4\pi\lambda_{ij}^{\text{out}}k_{\text{B}}T}}\sum_{N=0}^{\infty}\frac{1}{N!}\left(\frac{\lambda_{ij}^{\text{int}}}{\hbar\omega^{\text{int}}}\right)^N \exp\left(-\frac{\lambda_{ij}^{\text{int}}}{\hbar\omega^{\text{int}}}\right) \\ \times \quad & \exp\left\{-\frac{\left[\Delta E_{ij} - \hbar N\omega^{\text{int}} - \lambda_{ij}^{\text{out}}\right]^2}{4\lambda_{ij}^{\text{out}}k_{\text{B}}T}\right\} . \end{aligned} \tag{2.15}$$

### Comparison of rate expressions

To conclude the section, we compare the classical Marcus rate, eq. 2.6, the quantum-classical Jortner rate, eq. 2.15, and the multi-channel bimolecular rate, eq. 2.12 for electron transport in BTDF.

Figure 2.8 shows that the main difference between the quantum-classical and classical rates is the tail of smaller rates for large negative $\Delta E$ (endothermal hopping) and higher rates for large positive $\Delta E$ (exothermal hopping). Note that the Marcus rate is symmetric with respect to energy so that for too high energy differences (too strong exothermal hopping with $\Delta E > \lambda$) the rate decreases again, which is called the Marcus inverted region. This decrease is weaker if the internal degrees of freedom are treated quantum-mechanically since higher vibrational states are always accessible as indicated in fig. 2.7. Note that the inverted region is absent in the Miller-Abrahams rate (eq. 2.4). One can see that the bimolecular and the Jortner rates are similar (fig. 2.8a,b) and that distributions of Marcus and Jortner rates in fig. 2.8c are practically on top of each other (except for very small rates) and hence will lead to similar charge dynamics.

In general, our observation is that for a situation with (i) intramolecular reorganization energy similar to the outer-sphere one ($\lambda_{ij}^{\text{int}} \sim \lambda_{ij}^{\text{out}}$), (ii) reorganization energies similar to the frequency of the promoting mode $\lambda \sim \hbar\omega \approx 0.2\,\text{eV}$ and (iii) driving force $\Delta E_{ij}$ small compared to the intramolecular reorganization energy, and the classical Marcus rate eq. 2.6

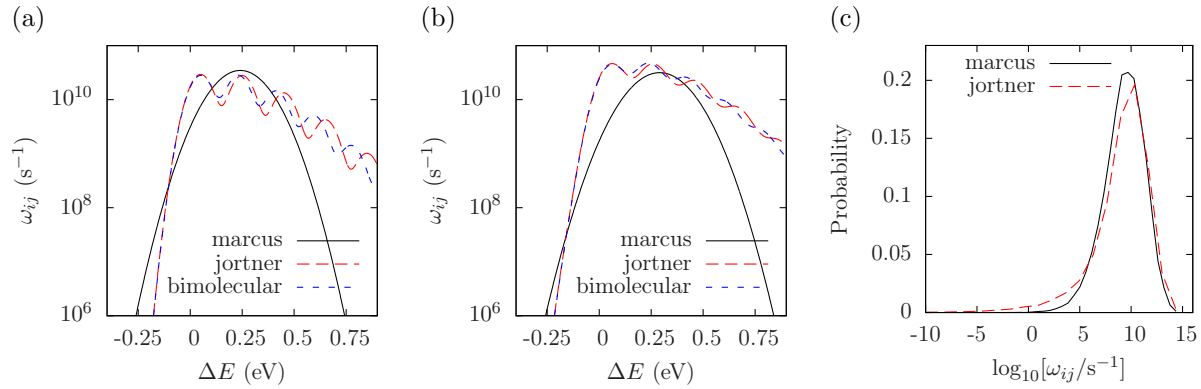


**Figure 2.8.** (a) Hopping rates for constant $J = 1\,\mathrm{meV}$ calculated at room temperature using the classical Marcus rate eq. 2.6, quantum-classical Levich-Jortner rate eq. 2.15 and bimolecular multichannel rate eq. 2.12. Constant outer-sphere reorganization energy $\lambda_{ij}^{\mathrm{out}} = 0.05\,\mathrm{eV}$, and internal reorganization energies for transport in pure BTDF so $\lambda_i^{cn} = \lambda_j^{cn} = 0.08\,\mathrm{eV}$ while $\lambda_i^{nc} = \lambda_j^{nc} = 0.11\,\mathrm{eV}$. For the Marcus rate $\lambda_{ij} = \lambda_i^{cn} + \lambda_j^{cn} + \lambda_{ij}^{\mathrm{out}}$ while for the Jortner rate $\lambda^{\mathrm{int}} = \lambda_i^{cn} + \lambda_j^{nc}$ plays a different role than $\lambda_{ij}^{\mathrm{out}}$. Intramolecular vibrations have averaged frequency $\hbar\omega_i^{\mathrm{int}} = \hbar\omega_j^{\mathrm{int}} = 0.2\,\mathrm{eV}$ for the Jortner rate, while $\hbar\omega_i^{n} = 0.2\,\mathrm{eV}$ and $\hbar\omega_j^{c} = \hbar\omega_i^{n}(\lambda_j^{nc}/\lambda_j^{cn})^{1/2}$ for the bimolecular rate. (b) The same but for $\lambda_{ij}^{\mathrm{out}} = 0.1\,\mathrm{eV}$. (c) Histogram of rates at a field of $10^7\,\mathrm{Vm}^{-1}$ for the Marcus and Jortner rates as computed from a morphology of 4096 BTDF molecules including transfer integrals (see sec. 2.5), conformational and electrostatic disorder (see sec. 2.7) and using $\lambda_{ij}^{\mathrm{out}} < 0.7\,\mathrm{eV}$ evaluated from the dielectric displacement with a Pekar factor of $c_p = 0.05$ (see sec. 2.6) and constant $\lambda^{\mathrm{int}} = 0.19\,\mathrm{eV}$. Only a small difference can be seen in the tail of small rates.

and semi-classical (eq. 2.15 and eq. 2.12) expressions lead to quantitatively similar rates. However, for systems with large $\Delta E_{ij}$, e.g. when computing escape rates from traps, eq. 2.12 or eq. 2.15 should be used. In this case a rather accurate estimate of the outer-sphere reorganization energy is required [89].

In case of BTDF a small static dipole moment (see sec. 2.7) leads to small site-energy differences $\Delta E$ so that the three rate expressions yield similar results for moderate electric fields. This is also true in a more complicated situation of a host-guest system treated in sec. 3.3, where BTDF is doped with small amounts of an emitter molecule. Finally, in case of the system studied in ch. 4 energetic disorder can be neglected due to strong nematic order. Therefore, the classical Marcus rate expression is used for the remainder of this thesis. From now on, our task is to compute all the ingredients entering eq. 2.6 as accurately as possible. This implies the use of electronic structure techniques for single molecular properties (internal reorganization energies or conformational energetic disorder) and pair properties (transfer integrals), while classical simulation methods are needed for long-range electrostatic interactions for site energies as outlined in the following sections of this chapter. With the rates at hand, one can then study charge transport by solving the differential (master) equation, e.g. by using the kinetic Monte Carlo method which is

capable of simulating charge dynamics of non-steady-state systems. The full workflow for the transport simulation has been illustrated in fig. 2.1.

## 2.5 Transfer integrals

In order to evaluate the charge transfer rate (eq. 2.6) for all conjugated segments in the neighborlist with atomistic coordinates obtained from the realistic morphology introduced in sec. 2.3, we need to compute electronic transfer integrals $J_{ij}$. They are defined as

$$J_{ij} = \left\langle \phi^i \left| \hat{H} \right| \phi^j \right\rangle, \tag{2.16}$$

where $\phi^i$ and $\phi^j$ are diabatic states of a dimer consisting of conjugated segments $i$ and $j$, i.e for $\phi^i$ the charge is fully localized on conjugated segment $i$ while segment $j$ is neutral and for $\phi^j$ the charge has been transferred to segment $j$ (in case of BTDF the charge is fully localized on a molecule so that the segments $i$ and $j$ correspond to neighboring molecules). $\hat{H} = \hat{H}_i + \hat{H}_j + \hat{H}_{ij}$ is the electronic Hamiltonian of the formed dimer. Within the frozen-core approximation, a typical choice for the diabatic wavefunctions $|\phi^i\rangle$ in case of hole transport consists of the highest occupied molecular orbital (HOMO) of molecule $i$ (which is extended to a dimer state by setting all coefficients for basis functions localized on molecule $j$ to zero), and the lowest unoccupied molecular orbital (LUMO) in the case of electron transfer (with similar extension), while $\hat{H}$ is an effective single-particle Hamiltonian, e.g. Fock operator or, in case of density-functional theory (DFT), Kohn-Sham operator of the dimer. As such, $J_{ij}$ is a measure of the strength of the electronic coupling of the frontier orbitals of monomers mediated by the dimer interactions. Intrinsically, the transfer integral is very sensitive to the molecular arrangement, i.e. the distance and the mutual orientation of the molecules participating in charge transport. Since this arrangement can also be significantly influenced by static and/or dynamic disorder [33, 54, 57, 58, 86], it is essential to calculate $J_{ij}$ explicitly for each hopping pair within a realistic morphology. Considering that the number of dimers for which eq. 2.16 has to be evaluated is proportional to the number of molecules times their coordination number, computationally efficient and at the same time quantitatively reliable schemes are required.

In order to evaluate $J_{ij}$, information about three objects is needed: the two monomer wave functions and the dimer interaction Hamiltonian. An approximate method based on Zerner's Independent Neglect of Differential Overlap (ZINDO) has been described in Ref. [84]. In the ZINDO approach, the overlap of the orbitals centered at different atoms are neglected and two electron integrals are only considered if the first two orbitals are centered at the same atom and the last two are also centered at the same atom (which does not have to be the same atom as the first). These two-electron integrals can be different for orbitals with different angular momentum and are parametrized with the help of spectroscopic data. This semi-empirical method is substantially faster than first-principles approaches in calculation of the transfer integral, since it avoids the self-consistent calculations on each individual monomer and dimer. This allows to construct the matrix elements of the

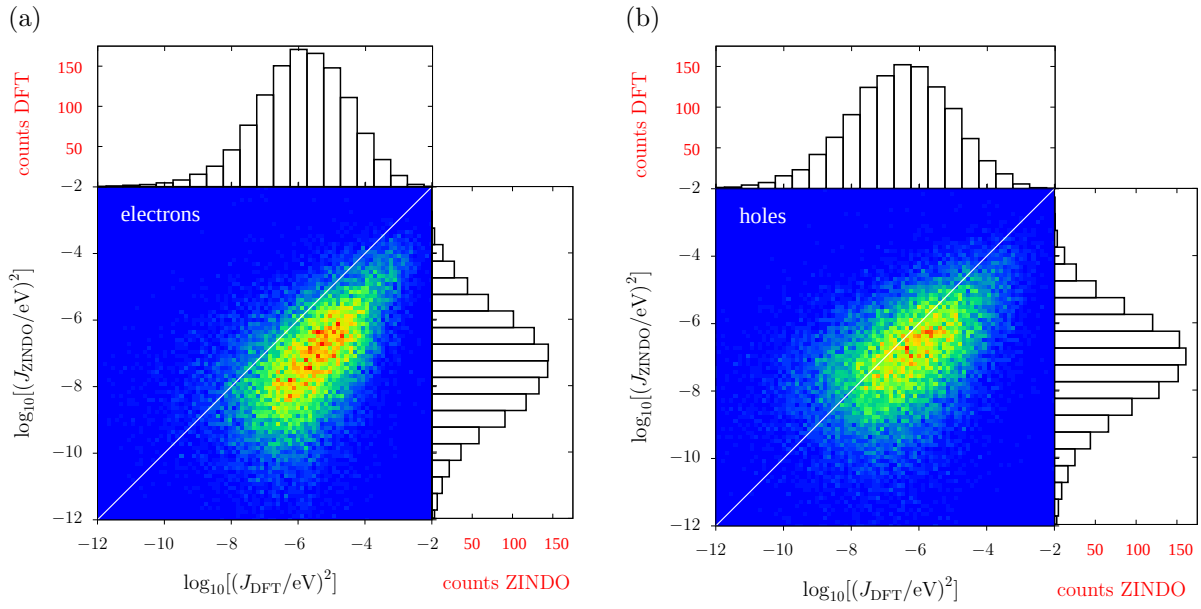


**Figure 2.9.** Distributions and correlation of transfer integrals for 4096 BTDF molecules for 30.000 pairs from the MD simulation calculated using ZINDO and DFT methods. (a) Transfer integrals for electron transport and (b) for hole transport.

ZINDO Hamiltonian of the dimer from the weighted overlap of molecular orbitals of the two monomers, i.e. $J_{ij} \sim \langle \phi^i | \phi^j \rangle$. Together with the introduction of rigid fragments, only a single self-consistent calculation on one isolated conjugated segment is required. All relevant molecular overlaps can then be constructed from the obtained molecular orbitals. This Molecular Orbital Overlap (MOO) method has been applied successfully to study charge transport, for instance, in discotic liquid crystals [54, 60, 61], polymers [59], or partially disordered organic crystals [56–58].

While the use of the semi-empirical ZINDO method provides an efficient on-the-fly technique to determine electronic coupling elements, it is not generally applicable to all systems. For instance, its predictive capacity with regards to atomic composition and localization behavior of orbitals within more complex structures is reduced. Moreover, transition- or semi-metals are often not even parametrized. In this case, *ab-initio* based approaches, e.g., DFT can remedy the situation [83, 90–94]. Within the dimer projection method described in detail in Ref. [83], explicit quantum-chemical calculations are required for every molecule and every hopping pair in the morphology. As a consequence, this procedure is significantly more computationally demanding.

As an example, distributions of transfer integrals are calculated using ZINDO and DFT obtained from the PBE functional and the TZVP basis [95] (similar to the triple zeta basis set introduced in sec. 2.2.1). Results are shown in fig. 2.9 for the amorphous phase of 4096 BTDF molecules for electrons (based on LUMO) and holes (based on HOMO). Distributions deviate by roughly one order of magnitude for hole transport which might

be due to the smaller basis set and the resulting stronger localization of orbitals in case of ZINDO. Distributions of electrons show even stronger differences indicating that the semi-empirical ZINDO formalism is unreliable in this case. Since we also want to compare transfer integrals of the pure BTDF system to the electronic couplings in the emission layer of an OLED, where BTDF is doped with a triplet emitter (containing the transition metal Ir), DFT is used for computation of $J_{ij}$ in the remaining part of this thesis.

## 2.6 Reorganization energy

The reorganization energy $\lambda_{ij}$ takes into account the change in nuclear and dielectric degrees of freedom as the charge moves within the charge-transfer complex from donor $i$ to acceptor $j$. It has two contributions: intramolecular, $\lambda_{ij}^{\text{int}}$, which is due to reorganization of nuclear coordinates of the molecules $i$ and $j$ inside the complex, and intermolecular (outer-sphere), $\lambda_{ij}^{\text{out}}$, which is due to the relaxation of the environment. In what follows we discuss how these contributions can be calculated.

### 2.6.1 Intramolecular reorganization energy

The rearrangement of the nuclear coordinates of the two molecules $i$ and $j$ forming the charge-transfer complex after a charge transfer results in the dissipation of the internal reorganization energy, $\lambda_{ij}^{\text{int}}$. It can be computed from four points on the potential energy surface (PES) of both molecules in neutral and charged states, as indicated in fig. 2.10. Adding the contributions due to discharging of molecule $i$ and charging of molecule $j$ (see discussion in sec. 2.4) yields [82]

$$\lambda_{ij}^{\text{int}} = \lambda_i^{cn} + \lambda_j^{nc} = U_i^{nC} - U_i^{nN} + U_j^{cN} - U_j^{cC} \,. \tag{2.17}$$

Here $U_i^{nC}$ is the internal energy of the neutral molecule $i$ in the geometry of its charged state (small $n$ denotes the neutral charge state and capital $C$ the geometry of the charged molecule). Similarly, $U_j^{cN}$ is the energy of the charged molecule $j$ in the geometry of its neutral state. If the PES of neutral and charged states are different for the same molecule, that is $\lambda_i^{cn} \neq \lambda_i^{nc}$, reorganization energies of discharging molecule $i$ and charging molecule $j$ cannot simply be added in eq. 2.6. If both modes are treated classically, the rate is an integral over the charge detachment and attachment spectrum of molecules $i$ and $j$ [96]. For most systems, however, the reorganization energies for charging or discharging of the same molecule do not deviate by more than a few percent, hence eq. 2.6, the Marcus rate expression can safely be used. Note that the PES of the donor and acceptor are not identical for chemically different compounds or for conformers of the same molecule. In this case $\lambda_i^{cn} \neq \lambda_j^{cn}$ and $\lambda_i^{nc} \neq \lambda_j^{nc}$. Thus $\lambda_{ij}^{\text{int}}$ is a property of the charge-transfer complex, and not of a single molecule, which is important for the discussion in sec. 3.3.3, where reorganization energies in a host-guest system are evaluated.

In BTDF, the eight soft dihedrals $\delta$ introduced in fig. 2.2 can have all possible values in the amorphous phase, as shown in fig. 2.5. Molecular conformations are then 'frozen' due to

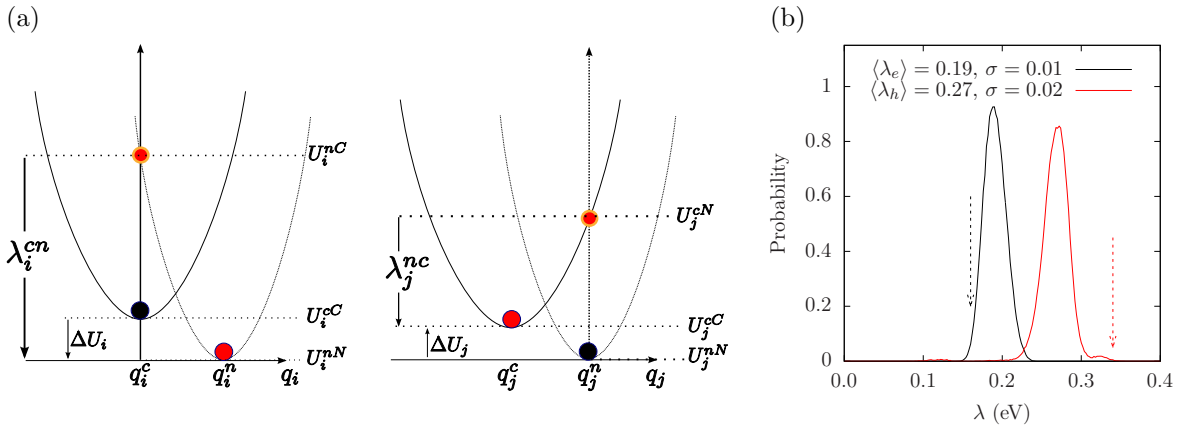


**Figure 2.10.** (a) Intramolecular reorganization energy: Potential energy surfaces of donor(left) and acceptor(right) in charged and neutral states. After the change of the charge state (black to orange circle) both molecules relax their nuclear coordinates (orange to red). If all vibrational modes are treated classically, the total internal reorganization energy and the internal energy difference of the charge transfer reaction are $\lambda_{ij}^{\text{int}} = \lambda_i^{\text{cn}} + \lambda_j^{\text{nc}}$ and $\Delta E_{ij}^{\text{int}} = \Delta U_i - \Delta U_j$, respectively. (b) Histogram of intramolecular reorganization energy $\lambda_{ij}$ for electrons and holes from an amorphous phase of 512 BTDF molecules taking into account different conformations that arise in the bulk. If the molecules could fully relax $\lambda_{e(h)}^{\text{free}} = 0.16(0.34)\,\text{eV}$ as indicated by the arrows which deviates from the mean of the distribution in the bulk.

non-bonded interactions as explained in sec. 2.2.4. In order to evaluate how reorganization energies depend on molecluar conformations, the internal energies entering eq. 2.17 were calculated after optimizing molecular geometries of all molecules whose coordinates were taken from the small MD simulation with 512 neutral molecules in charged and neutral states with the soft degrees of freedom $\delta$ constrained to their time-averaged mean values in each molecule as presented in fig. 2.5. Due to the conformational disorder, the mean of the distribution for $\lambda_{ij}^{\text{int}}$ does not coincide with the value obtained in the gas phase. Quantitatively, the shift of the mean of the reorganization energy in the bulk for holes from the gas-phase value of 0.34 eV to 0.27 eV by $\Delta\lambda = 0.07\,\text{eV}$ will decrease the Marcus rates by a factor of $c = \exp\left[\frac{\Delta\lambda}{4k_{\text{B}}T}\right] \sim 2$ for small energy differences $\Delta E$, while the effect of the broadening of the distribution of $\lambda_{ij}^{\text{int}}$ on mobility is even smaller.

### 2.6.2 Outer-sphere reorganization energy

During the charge transfer reaction, also the molecules outside the charge-transfer complex reorient and polarize in order to adjust for changes in electric field, resulting in the outer-sphere contribution to the reorganization energy. $\lambda_{ij}^{\text{out}}$ is particularly important if charge transfer occurs in a polarizable environment. Assuming that charge transfer is much slower than electronic polarization but much faster than nuclear rearrangement of

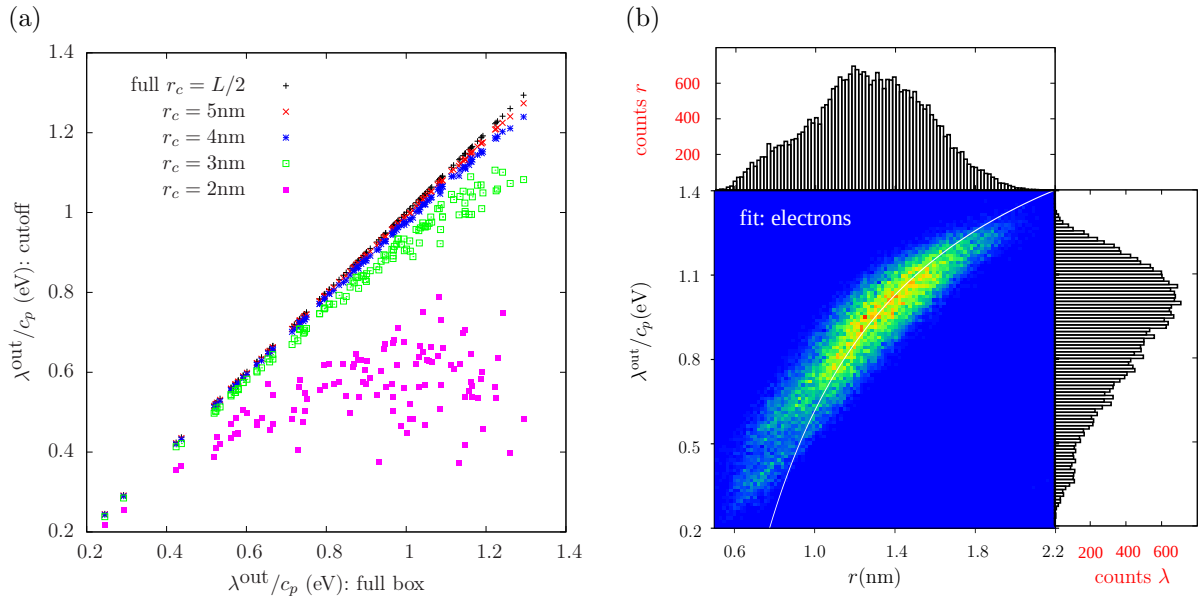


**Figure 2.11.** (a) Outer sphere reorganization energy for electrons divided by the Pekar factor $c_p$ for 125 selected BTDF charge-transfer complexes with different cutoff radius changing the number of molecules surrounding the complex that are taken into account: a cutoff of 5 nm is sufficient for convergence in a cubic box containing 4096 molecules with $L = 16$ nm. (b) Histogram of outer sphere reorganization energy from the neighborlist divided by the Pekar factor $c_p$ as function of the distance $r_{ij}$ between BTDF molecules in the charge-transfer complex. A fit to eq. 2.20 is also shown yielding $R = 0.7$ nm in agreement with the radius of gyration $R_g = 0.6$ nm.

the environment, $\lambda_{ij}^{\rm out}$ can be estimated from the electric displacement fields created by the charge-transfer complex [19]

$$\lambda_{ij}^{\rm out} = \frac{c_p}{2\epsilon_0} \int_{V^{\rm out}} dV \left[\vec{D}_I(\vec{r}) - \vec{D}_F(\vec{r})\right]^2 , \tag{2.18}$$

where $\epsilon_0$ is the the permittivity of free space, $\vec{D}_{I,F}(\vec{r})$ are the electric displacement fields created by the charge-transfer complex in the initial (charge on molecule $i$) and final (charge transferred to molecule $j$) states, $V^{\rm out}$ is the volume outside the complex, and

$$c_p = \frac{1}{\epsilon_{\rm opt}} - \frac{1}{\epsilon_{\rm s}} \tag{2.19}$$

is the Pekar factor, which is determined by the low (static $\epsilon_{\rm s}$) and high (optical $\epsilon_{\rm opt}$) frequency dielectric permittivities. This factor takes into account the fact that the polarization field has a high and a low frequency part. While the high frequency part is determined only by electronic contributions, the low frequency part is determined by electrons and the reorientation of the heavier nuclei. Since we are interested only in the slow relaxation of the nuclear coordinates of the environment, the electronic contribution to

the low frequency Polarization field has to be eliminated which is done by introducing the Pekar factor [19].

Eq. 2.18 can be simplified by assuming spherically symmetric charge distributions on molecules $i$ and $j$ with total charge $e$. Integration over the volume $V^{\text{out}}$ outside of the two spheres of radii $R_i$ and $R_j$ centered on molecules $i$ and $j$ leads to the classical Marcus expression for the outer-sphere reorganization energy [19]

$$\lambda_{ij}^{\text{out}} = \frac{c_p e^2}{4\pi\epsilon_0}\left(\frac{1}{2R_i} + \frac{1}{2R_j} - \frac{1}{r_{ij}}\right), \tag{2.20}$$

where $r_{ij}$ is the molecular separation in the charge-transfer complex. While eq. 2.20 captures the main physics, e.g. predicts smaller outer-sphere reorganization energies (higher rates) for molecules at smaller separations, it often cannot provide quantitative estimates, since charge distributions are rarely spherically symmetric.

Alternatively, the displacement fields can be constructed using the atomic partial charges. The difference of the displacement fields at the position of an atom $b_k$ outside the charge-transfer complex (molecule $k \neq i, j$) can be expressed as

$$\vec{D}_I(\vec{r}_{b_k}) - \vec{D}_F(\vec{r}_{b_k}) = \sum_{a_i} \frac{q_{a_i}^c - q_{a_i}^n}{4\pi} \frac{(\vec{r}_{b_k} - \vec{r}_{a_i})}{|\vec{r}_{b_k} - \vec{r}_{a_i}|^3} + \sum_{a_j} \frac{q_{a_j}^n - q_{a_j}^c}{4\pi} \frac{(\vec{r}_{b_k} - \vec{r}_{a_j})}{|\vec{r}_{b_k} - \vec{r}_{a_j}|^3}, \tag{2.21}$$

where $q_{a_i}^n$ ($q_{a_i}^c$) is the partial charge of atom $a$ of the neutral (charged) molecule $i$ in vacuum. The partial charges of neutral and charged molecules are obtained by fitting their values to reproduce the electrostatic potential of a single molecule (charged or neutral) in vacuum. Assuming a uniform density of atoms, the integration in eq. 2.18 can be rewritten as a density-weighted sum over all atoms excluding those of the charge-transfer complex.

Using eq. 2.21, $\lambda_{ij}^{\text{out}}/c_p$ was calculated for all pairs from the neighborlist of a system of 4096 BTDF molecules with a neighborlist cutoff of 0.7 nm for the seven fragments using ESP charges of charged and neutral molecules (see sec. 2.2). The resulting distribution of $\lambda_{ij}^{\text{out}}/c_p$ is shown in fig. 2.11, together with a fit to eq. 2.20. The fit yields $R = 0.7\,\text{nm}$ which is comparable to the radius of gyration of BTDF $R_g = 0.6\text{nm}$. Note that the fit predicts *negative* $\lambda_{ij}^{\text{out}}$ for a few pairs where the molecules in the charge-transfer complex are very close ($r_{ij} < R$) which would lead to ill-defined Levich-Jortner rates, eq. 2.15.

The remaining unknown needed to calculate $\lambda_{ij}^{\text{out}}$ is the Pekar factor $c_p$ defined in eq. 2.19. In polar solvents $\epsilon_{\text{s}} \gg \epsilon_{\text{opt}} \sim 1$ and $c_p$ is of the order of 1 resulting in very high outer-sphere reorganization energies. In most organic semiconductors, however, molecular orientations are fixed and therefore the low frequency dielectric permittivity is of the same order of magnitude as $\epsilon_{\text{opt}}$. Hence, $c_p$ is small and its value is very sensitive to differences in the permittivities.

For BTDF, $\epsilon_{\text{s}} = 2.82 \pm 0.3$ is the experimentally measured dielectric constant at low frequencies ($10^4\,\text{Hz}$), while at optical frequencies ($3.75 \times 10^{14}\,\text{Hz}$, below electronic absorption) $\epsilon_{\text{opt}} = 2.75 \pm 0.1$. Thus $c_p = 0.01 \pm 0.04$ yielding outer-sphere reorganization energies of $\lambda_{ij}^{\text{out}} < 0.07\,\text{eV}$, which are small compared to $\lambda_{ij}^{\text{int}}$. Similar results have been reported for other organic semiconductors and different methods for computing $\lambda_{ij}^{\text{out}}$ [89, 97, 98].

## 2.7 Site-energy difference

A charge-transfer reaction between molecules $i$ and $j$ is driven by the site-energy difference, $\Delta E_{ij} = E_i - E_j$. It can be computed from the individual site energies $E_i$ which are defined as the difference of the energy of the entire system when molecule $i$ is charged or neutral. Since the transfer rate depends exponentially on the driving force $\Delta E_{ij}$ (see eq. 2.6) it is important to compute site-energy distributions as accurately as possible. The total site-energy difference has contributions due to externally applied electric field, electrostatic interactions including polarization effects, and internal energy differences. In what follows we discuss how to estimate these contributions by making use of first-principles calculations and polarizable force-fields.

### 2.7.1 Externally applied electric field

The contribution to the site-energy difference due to an external electric field $\vec{F}$ is given by $\Delta E_{ij}^{\text{ext}} = q\vec{F} \cdot \vec{r}_{ij}$, where $q = \pm e$ is the charge and $\vec{r}_{ij} = \vec{r}_i - \vec{r}_j$ is a vector connecting molecules $i$ and $j$. For typical distances between small molecules, which are of the order of 1 nm, and moderate fields of $F < 10^8$ V/m this term is always smaller than 0.1 eV. Note that as we treat the external field as a perturbation to the energetic landscape we can obtain the charge carrier mobility as $\mu = \langle v \rangle / F$ where $\langle v \rangle$ is the projection of the mean carrier velocity on the field. In the limit $F \to 0$ the zero-field mobility is then identical to the diffusive mobility according to the Einstein relation as discussed in sec. 2.9.3.

### 2.7.2 Electrostatic energy

Variations of the local electric field inside the organic semiconductor can result in large electrostatic contributions to the site energies. A typical example is an amorphous phase of small molecules where one of the molecules is charged and the surrounding neutral molecules carry a static dipole moment: For randomly oriented static dipoles of strength $d$ on a regular lattice with spacing $a$ the individual site energies due to charge-dipole interactions are approximately Gaussian distributed [99] with zero mean (due to angular averaging) and a width $\bar{\sigma}$ (energetic disorder) given by

$$p(E^{\text{el}}) = \frac{1}{\bar{\sigma}\sqrt{2\pi}} \exp\left[ -\left( \frac{E^{\text{el}}}{\sqrt{2}\bar{\sigma}} \right)^2 \right], \qquad \bar{\sigma} = \frac{2.35ed}{4\pi\epsilon_0\epsilon_{\text{s}}a^2} \tag{2.22}$$

where $\epsilon_0$ is the permittivity of free space and $\epsilon_{\text{s}}$ is the relative dielectric constant which accounts for possible screening due to polarization of the material. Small energetic disorder facilitates high mobility, since the energetic landscape the charge travels in is rather smooth. Quantitatively, the mobility increases exponentially with lower disorder

$$\mu \sim \exp\left[ -\left( \frac{2\bar{\sigma}}{3k_{\text{B}}T} \right)^2 \right] \tag{2.23}$$

as shown in the Gaussian disorder model [37]. This relation is often used to extract the value of the energetic disorder $\bar{\sigma}$ from experimental data by plotting $\log \mu(T^2)$ obtained by measuring the mobility at different temperatures.

Since our approach allows to access all atomistic coordinates in the morphology, we can use atomic partial charges of charged and neutral molecules, as introduced in sec. 2.6.2 to evaluate the energetic disorder and the electrostatic contribution to the site energies $\Delta E_{ij}^{\mathrm{el}} = E_i^{\mathrm{el}} - E_j^{\mathrm{el}}$ from a Coulomb sum [54] of the individual sites which are defined as

$$E_i^{\mathrm{el}} = E_i^{\mathrm{crg}} - E_i^{\mathrm{neu}} = \frac{1}{4\pi\epsilon_0} \sum_{a_i} \sum_{\substack{b_k \\ k \neq i}} \frac{\left(q_{a_i}^{\mathrm{crg}} - q_{a_i}^{\mathrm{neu}}\right) q_{b_k}^{\mathrm{neu}}}{\epsilon_{\mathrm{s}} r_{a_i b_k}}, \tag{2.24}$$

where $E_i^{\mathrm{crg}}$ and $E_i^{\mathrm{neut}}$ are the intermolecular energies when molecule $i$ is charged or neutral and $r_{a_i b_k} = |\vec{r}_{a_i} - \vec{r}_{b_k}|$ is the distance between atoms $a_i$ and $b_k$. The first sum extends over all atoms of molecule $i$, for which the site energy is calculated. The second sum reflects interactions with all atoms of neutral molecules $k \neq i$. Hence, we assumed that the influence of conformational changes on partial charges and changes of the molecular geometry upon charging are small.

In evaluating eq. 2.24 we can include interactions of the charged molecule $i$ with *all* neutral molecules by using periodic boundary conditions and the nearest image convention. Alternatively, we can use a spherical cutoff $r_{\mathrm{el}}$ in order to include only a certain amount of molecules interacting with the charge to speed up calculations. The influence of this cutoff on site-energy distributions is discussed in sec. 2.9.4.

As an example we have computed individual electrostatic site energies using eq. 2.24 for a box of 4096 BTDF molecules using the nearest image convention. We have first neglected polarization effects by setting $\epsilon_{\mathrm{s}} = 1$. As energy differences are important for the charge-transfer rate, we also evaluate the distributions of the site-energy differences from the neighborlist introduced at the end of sec. 2.2. Both distributions are displayed for electrons and holes in fig. 2.12.a. As expected from the lattice model [99], the distributions are Gaussian and the energetic disorder is rather small $\bar{\sigma} \sim 0.11\,\mathrm{eV}$ because of the small static dipole moment $d = 0.8\,\mathrm{D}$ in BTDF.

Note however, that the mean for the individual energies does not vanish as predicted by the lattice model and also energetic disorder is twice as large as $\bar{\sigma} = 0.06\mathrm{eV}$ obtained from eq. 2.22 with a lattice spacing of $a = 1\,\mathrm{nm}$ which can be estimated from the density. This indicates that the assumptions made in the lattice model such as non-overlapping charge distributions and identical intermolecular distances break down already at the static level.

Another remarkable fact about the electrostatic site-energy distribution are spatial correlations between the energies that arise due to similar electrostatic environments of neighboring molecules. While an uncorrelated Gaussian distribution of width $\bar{\sigma}$ for individual energies would lead to a width of $\sigma = \sqrt{2}\bar{\sigma}$ for the energy-differences, fig. 2.12.a shows that the distribution for the differences from the neighborlist is only slightly broader than the distribution for the individual energies ($\sigma_{\mathrm{nb}} \approx \bar{\sigma}$) indicating a spatial correlation, whose influence on transport is discussed in sec. 2.7.5.

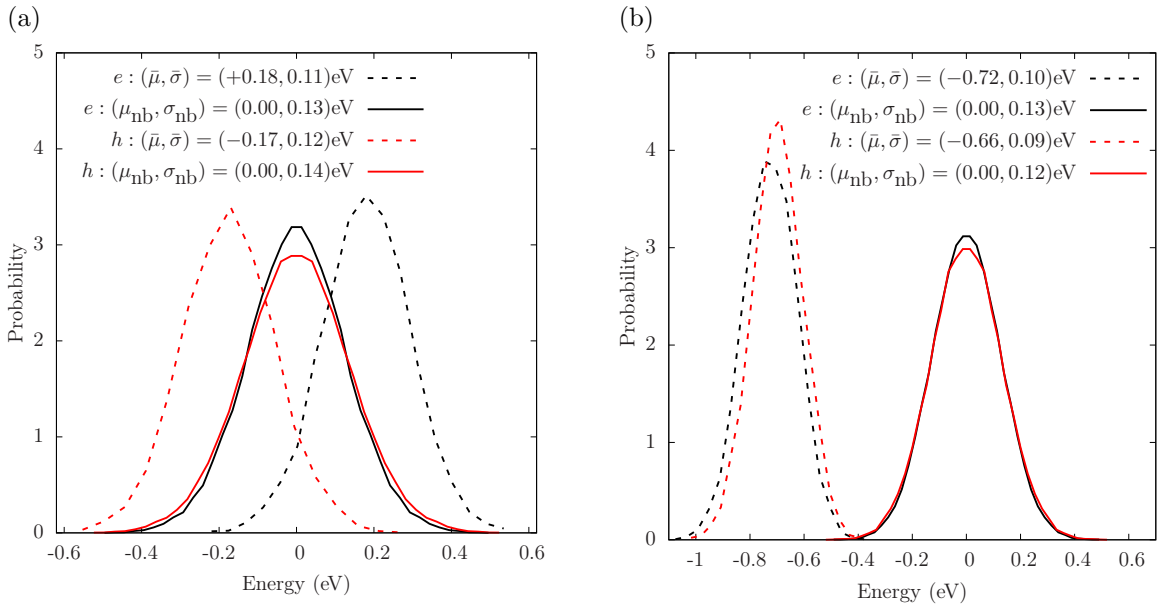


**Figure 2.12.** Electrostatic site energies for 4096 BTDF molecules. (a) Distributions of static ($\epsilon_s = 1$) energies (dashed) in the nearest image convention and energy differences from the neighborlist. The mean $\mu$ and width $\sigma$ of the Gaussian distributions are given in brackets for electrons and holes. (b) Including polarization (Thole model with $r_{\rm el} = 4\,$nm) leads to stabilization of individual site energies and narrowing of the distributions due to screening. Electrons are stabilized more than holes due to higher change in polarizability upon charging (see ch. 3).

### 2.7.3 Polarization effects

The simplest way of taking into account the influence of polarization is to use a relative dielectric constant $\epsilon_{\rm s}$ in the Coulomb sum, eq. 2.24. Bulk values of $\epsilon_{\rm s} = 2 - 5$ for typical organic semiconductors uniformly reduce all site energies but are not capable of describing polarization effects on an atomistic scale. The contribution to $E_i^{\rm el}$ from the first coordination shell is then underestimated due to over-screening and, as a result, the site-energy differences become artificially small.

Alternatively, one can use an effective screening derived as a function of the bulk dielectric constant from lattice simulations [100], or introduce a phenomenological distance-dependent screening function to replace the constant $\epsilon_{\rm s}$ in eq. 2.24 by [53]

$$\epsilon(r_{a_i b_k}) = \epsilon_{\rm s} - (\epsilon_{\rm s} - 1)\left(1 + \kappa r_{a_i b_k} + \frac{1}{2}\kappa^2 r_{a_i b_k}^2\right) \exp -\kappa r_{a_i b_k}\,, \tag{2.25}$$

where $r_{a_i b_k}$ is the distance between atoms $a$ and $b$ of molecules $i$ and $k$, $\kappa$ is the inverse screening length and $\epsilon_{\rm s}$ the bulk dielectric constant. For a monovalent ion in water, for example, $\epsilon_{\rm s} = 80$ and $\kappa = 3\,{\rm nm}^{-1}$ [101]. This screening function ensures that neighboring atoms interact via an unscreened Coulomb potential ($\epsilon \sim 1$) and the electrostatic interaction between atoms at large separations is screened by $\epsilon_{\rm s}$.

While phenomenological distance-dependent screening is computationally efficient, it cannot be used for inhomogeneous systems or systems with anisotropic molecular polarizabilities. Moreover, $\epsilon_\mathrm{s}$ and $\kappa$ are not known for newly synthesized compounds. Finally, using an effective distance dependent screening will always lead to a reduction of the site-energy disorder, which is not necessarily the case e.g. due to changes in molecular polarizabilities upon charging as discussed in ch. 3.

A more general approach relies on charge-transfer between atoms [102] or self-consistent methods to obtain polarization fields [103]. In this thesis we use a polarizable force-field based on the Thole model [104] since parametrization for new compounds is simple. In this model, every atom is assigned an isotropic polarizability which allows to induce atomistic dipoles in response to an electric field originating from the electrostatic environment. These induced dipoles are allowed to interact so that the polarization contribution has to be refined iteratively. In order to prevent a polarization catastrophe that can occur by cooperative (head to tail) interaction of induced point dipoles in the direction of their connection, the induced interactions are damped by smearing out the corresponding charge distributions. The polarizabilities and damping constant can be found by comparison to ab-initio calculations or to experimental data [105].

The iterative procedure for the calculation of induced dipoles has been implemented in the TINKER package [106] and works as follows: first, the electric fields, $\vec{F}_{a_i}^{(0)}$, at all atoms $a$ in all molecules $i$ are evaluated as created by all atomic partial charges ($\epsilon_\mathrm{s} = 1$, nearest image convention or cutoff) and induced dipole moments on all atoms, $\vec{\mu}_{a_i}^{(0)} = \alpha_{a_i}\vec{F}_{a_i}^{(0)}$ are computed from the fields and the atomic polarizabilities $\alpha_{a_i}$. During this first step, intramolecular interactions are excluded. The induced dipole moments are then iteratively refined by the recursive relation $\vec{\mu}_{a_i}^{(k+1)} = \vec{\mu}_{a_i}^{(k)} + \alpha_{a_i}\vec{F\prime}_{a_i}^{(k)}$, where the field $\vec{F\prime}_{a_i}^{(k)}$ is created on atom $a$ in molecule $i$ only by the induced dipoles of all other atoms but now including intramolecular contributions which allows for anisotropic molecular polarizabilities. This recursive relation $x^{(k+1)} = f\left(x^{(k)}\right)$ can be solved by successive over-relaxation $x^{(k+1)} = (1-\omega)x^{(k)} + \omega f\left(x^{(k)}\right)$ with a damping constant $\omega$ which yields [107]

$$\vec{\mu}_{a_i}^{(k+1)} = (1-\omega)\vec{\mu}_{a_i}^{(k)} + \omega\left(\vec{\mu}_{a_i}^{(k)} + \alpha_{a_i}\vec{F\prime}_{a_i}^{(k)}\right) . \tag{2.26}$$

The procedure is repeated until $\sum_{a_i} |\vec{\mu}_{a_i}^{(k+1)} - \vec{\mu}_{a_i}^{(k)}| < 10^{-4}\,\mathrm{D}$ which converges energies to meV. We have found fastest convergence for neutral (cationic/anionic) systems using $\omega = 0.5\,(0.35/0.2)$.

As for eq. 2.24, the site energy of molecule $i$ is evaluated as the total intermolecular energy of the system when molecule $i$ is charged and the total energy of the system in the neutral state has to be subtracted. Note however that the induced dipole moments on the surrounding molecules are different depending on which molecule is charged, so that in addition to all interactions between the charged molecule $i$ and all others $k \neq i$ that are counted in eq. 2.24, now also interactions between the surrounding molecules have to be taken into account. Therefore computational time for evaluating one site energy $E_i^\mathrm{el}$ grows quadratically with the number of involved molecules.

| | neutral | anion | cation | $f_a$ | $f_c$ |
|---|---|---|---|---|---|
| $\frac{1}{3}\mathrm{Tr}\hat{\alpha}$ (Å$^3$) | 91.1 | 210.2 | 154.8 | 3.4 | 2.1 |
| $\alpha_1 : \alpha_2 : \alpha_3$ (DFT) | 1:1.0:1.3 | 1:1.1:3.7 | 1:1.3:3.0 | | |
| $\alpha_1 : \alpha_2 : \alpha_3$ (THO) | 1:1.0:1.2 | 1:1.1:1.4 | 1:1.2:1.3 | | |

**Table 2.3.** Polarizabilities for BTDF. Given are orientational averages of the polarizability as a third of the trace of the polarizability tensor $\hat{\alpha}$ obtained by DFT. Isotropic scaling factors $f_{(a,c)}$ for anions and cations are introduced to increase atomistic polarizabilities in the Thole model to match the orientational average exactly to the value obtained by DFT. Anisotropies of $\hat{\alpha}$ from DFT and the Thole model are analyzed in terms of the ratio of the three eigenvalues with respect to the smallest value $\alpha_1$, which shows that isotropic scaling in the Thole model leads to underestimation of the anisotropy in the charged states.

Due to the large number of interactions in the self-consistent loop, these calculations become time-consuming for large systems. Therefore, for big simulation boxes (i.e. 4096 BTDF molecules) we introduced a cutoff radius of $r_{\mathrm{el}} = 4\,\mathrm{nm}$ in order to compute the polarized site energies in the Thole model. This cutoff corresponds to a sphere containing 250 molecules.

For homogeneous systems and isotropic molecular polarizabilities one can avoid this problem by performing self-consistent calculations for small systems, parametrizing the distance dependent screening function, eq. 2.25, and then using it to study much larger systems. To this end, the bulk dielectric constant can be obtained from the Clausius-Mosotti relation [108]

$$\epsilon_{\mathrm{s}} = 1 + \frac{12\pi\alpha N/V}{3 - 4\pi\alpha N/V} \tag{2.27}$$

where $\alpha$ is the molecular polarizability volume, and $N/V$ is the the number density. In case of BTDF $\epsilon_{\mathrm{s}} = 2.6$ according to eq. 2.27 with $N/V = 1\,\mathrm{nm}^{-1}$ and $\alpha = 91.1\,\mathrm{Å}^3$ which agrees well with the experimental value of $\epsilon_{\mathrm{s}} = 2.82 \pm 0.3$ from capacitance measurements. Using this value of $\epsilon_{\mathrm{s}}$, the parameter $\kappa$ in eq. 2.25 can then be then fitted to reproduce the distribution of site-energy differences for molecules from the neighbor list.

While this combined approach was successful yielding $\kappa = 1.3\mathrm{nm}^{-1}$ for the $\mathrm{Alq_3}$ molecule which has approximately spherical van der Waals surface [64], it fails in case of BTDF due to a large difference in polarizabilities of charged and neutral states (see sec. 3.3) and the anisotropic molecular shape that leads to an anisotropic polarizability tensor and strongly intercalating molecules.

In order to compare polarized site energies to the static case discussed in the previous section for the BTDF system we therefore have to invoke the Thole model. We use element-specific atomic polarizabilities $\alpha_{\mathrm{H,\,C,\,Si,\,O}} = (0.7, 1.9, 1.9, 1.2)\,\mathrm{Å}^3$ which yield perfect agreement with respect to *ab initio* methods (DFT with B3LYP functional and TZVP basis set) for the trace and anisotropy of polarizability tensors in neutral BTDF molecules as indicated in tab. 2.3. Furthermore a damping factor of $a = 0.39$ for interactions with

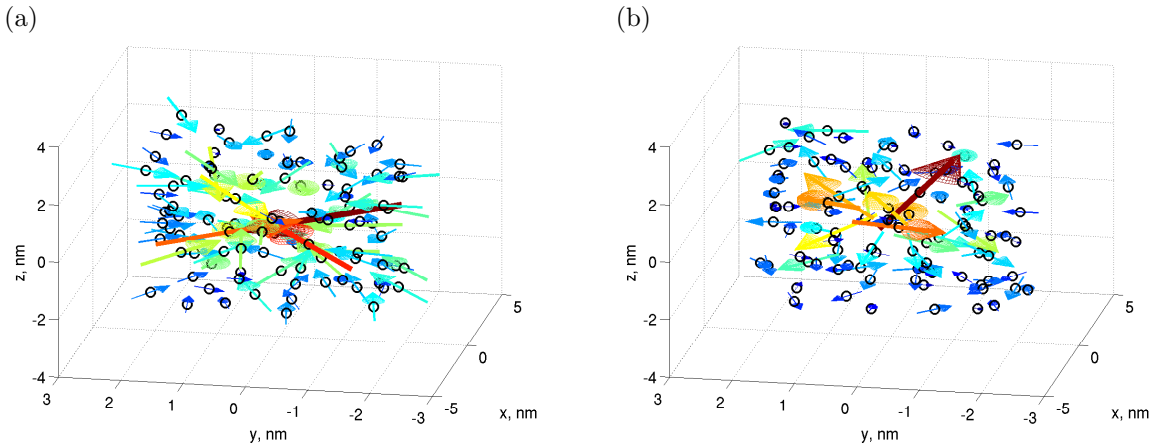


**Figure 2.13.** Polarization response of 100 BTDF molecules to a charged molecule in the center of the simulation box as computed using the Thole model. (a) A negatively charged molecule induces dipole moments on the surrounding molecules (black circles are centers of mass). These induced dipole moments are stronger (red) close to the charge and point towards it. (b) If the central molecule is positively charged, the molecular dipole moments point away from it.

induced moments is used to prevent a polarization catastrophe [106]. Since polarizabilities depend on the actual charge state of the molecules, we have scaled the atomic polarizabilities in case of anions(cations) by $f_{a(c)} = 3.4\,(2.1)$ as to reproduce the trace of the molecular polarizability tensor obtained by ab initio methods for the charged states. Note that the Thole model underestimates the anisotropy of the polarizability tensor of the charged states as can be seen in tab. 2.3, which could, in principle, be cured by introducing non-isotropic atomistic polarizabilities or different scaling factors $f$ for the atomistic polarizabilities.

The effect of placing a charged molecule in a polarizable environment is visualized in fig. 2.13. The charge on molecule $i$ induces atomic dipoles $\vec{\mu}_{a_k}$ on all surrounding neutral molecules, $k \neq i$, which are computed from the Thole model. These moments add up to molecular dipole moments $\vec{\mu}_k = \sum_{a_k} \vec{\mu}_{a_k}$ depicted in the figure. Although, on average, the induced dipoles are stronger if they are close to the charge ($\mu_k \sim r_{ik}^{-2}$) and are aligned with the (radial) electric field, the amorphous morphology and the anisotropic polarizability in combination with interactions between all induced dipoles, result in strong disorder in these dipole moments, which again indicates that polarization effects cannot be treated at a macroscopical level (see also sec. 3.3).

In a next step, we have computed polarized individual site energies from the Thole model and the corresponding site-energy differences from the neighborlist for a system of 4096 BTDF molecules, as shown in fig. 2.12.b. A comparison to the static case (fig. 2.12.a) shows that polarization stabilizes both anions and cations, e.g. mean energies of anions (relevant for electron transport) are reduced from 0.11 eV in the static case to $-0.72$ eV when polarization effects are included. Furthermore, very small effective screening can be observed that slightly reduces the width of all distributions, e.g. for electron transport the

disorder for individual energies is reduced from $\bar{\sigma} = 0.11\,\mathrm{eV}$ to $0.10\,\mathrm{eV}$. This screening is substantially weaker as it would be predicted by using the static dielectric constant $\epsilon_\mathrm{s} = 2.6$ in eq. 2.24, since in the special case of BTDF a change in polarizability upon charging induces additional disorder (see sec. 3.3).

Note that we have also checked that the site energies from morphologies of two independent MD snapshots are uncorrelated and that the mean and variance of site energies in these snapshots are practically identical for simulation boxes containing 4096 molecules.

### 2.7.4 Internal energy difference

The contribution to the site-energy difference due to different internal energies (see fig. 2.10) can be written as

$$\Delta E_{ij}^\mathrm{int} = \Delta U_i - \Delta U_j = \left(U_i^{cC} - U_i^{nN}\right) - \left(U_j^{cC} - U_j^{nN}\right) , \tag{2.28}$$

where $U_i^{cC(nN)}$ is the total energy of molecule $i$ in the charged (neutral) state and geometry. $\Delta U_i$ corresponds to the adiabatic ionization potential (or electron affinity) of molecule $i$. For one-component systems and negligible conformational changes $\Delta E_{ij}^\mathrm{int} = 0$. For multi-component systems, such as the emission layer of an OLED, the ionization potential of the matrix material BTDF and the emitter differs by roughly 1.5 eV (see sec. 3.3) so that $\Delta E_{ij}^\mathrm{int}$ has to be taken into account to describe the site-energy distributions of matrix and emitter.

Also in pure BTDF, significant conformational changes (see sec. 2.2) lead to a distribution of $\Delta E_{ij}^\mathrm{int}$. Since the single site values, $\Delta U_i$, are spatially not correlated, it is sufficient to compute the distribution for a small box and then randomly generate internal energies for larger boxes from this distribution. For 512 molecules we find a Gaussian distribution with a variance of $\sigma_{e(h)}^\mathrm{int} \sim 0.04\,(0.05)\,\mathrm{eV}$ for $\Delta E_{ij}^\mathrm{int}$ in case of electron (hole) transport. The influence of the internal energy disorder on the total disorder in the system $\bar{\sigma}_\mathrm{tot}$ is small compared to the electrostatic contribution because the variances of the two uncorrelated Gaussian variables add, $\bar{\sigma}_\mathrm{tot}^2 = \bar{\sigma}_\mathrm{int}^2 + \bar{\sigma}_\mathrm{el}^2$. Charge carrier mobility, for example, is reduced by less than half an order of magnitude if internal disorder is added to the disorder originating from electrostatic contributions.

### 2.7.5 Spatial correlations of energetic disorder

Long-range (electrostatic) interactions often result in spatially correlated disorder [99] which affects the onset of the mobility-field dependence [23, 53, 109].

To quantify the degree of correlation, one can calculate the spatial correlation function of $E_i$ and $E_j$ at a distance $r_{ij}$

$$C(r_{ij}) = \frac{\langle (E_i - \langle E \rangle)\,(E_j - \langle E \rangle) \rangle}{\langle (E_i - \langle E \rangle)^2 \rangle}, \tag{2.29}$$

where $\langle E \rangle$ is the average site energy. $C(r_{ij})$ is zero if $E_i$ and $E_j$ are uncorrelated and 1 if they are fully correlated. For a system of randomly oriented point dipoles on a lattice with

spacing $a$ with energetic disorder of $\bar{\sigma}$ and vanishing mean of the individual site-energies, the correlation function decays with the inverse distance for intermolecluar separations accoring to [110]

$$C(r_{ij})\rangle \sim \frac{\bar{\sigma}^2 a}{r_{ij}}\,. \tag{2.30}$$

Using these (three dimensional) correlations in a one-dimensional transport model yields an analytic expression for the mobility [23]

$$\mu = \mu_0 \exp\left[-\left(\frac{\bar{\sigma}}{k_\mathrm{B}T}\right)^2 + 2\frac{\bar{\sigma}}{k_\mathrm{B}T}\sqrt{eaF/k_\mathrm{B}T}\right], \tag{2.31}$$

where $\mu_0$ is the zero-field mobility, $e$ is the elementary charge and $F$ the applied electric field.

The linear dependence of the logarithm of the mobility with the square root of the applied electric field is known as the Poole-Frenkel behavior and can ben be seen in many experiments for charge transport in small organic molecules and polymers. Note that our approach of computing electrostatic and polarization interactions from the realistic morphology includes spatial correlations of the site-energies by construction. In order to investigate the effect of correlations on the mobility, we have used the organic semiconductor $Alq_3$ as a test-system, since its strong static dipole moment leads to pronounced spatial correlations. In this system, we have first performed charge-transport simulations using site-energies obtained as described in sec. 2.7.2 and sec. 2.7.3 and in a second simulation, we have destroyed the spatial correlations by randomly re-distributing these energies to the molecules in the simulation box. While in the first case, a clear Poole-Frenkel dependence develops, the mobility is practically field independent in the second case [64].

Furthermore, spatial correlations in site-energies can lead to current filaments because the energetic landscape of a charge carrier can be envisioned as mountains separated by wide and deep-lying valleys. Only these valleys are well sampled by the charge carriers as shown in fig. 1.1 for hole transport in a simulation box of 4096 $Alq_3$ molecules. These current filaments can have a negative impact on device stability due to material degradation. Note that in BTDF, energetic disorder is not as strong as in $Alq_3$ and spatial correlations are less pronounced because its dipole moment is small.

## 2.8 Solving the master equation

Having determined the list of conjugated segments (hopping sites) and charge transfer rates between them, the next task is to solve the master equation which describes the time evolution of the system

$$\frac{\partial P_\alpha}{\partial t} = \sum_\beta P_\beta \Omega_{\beta\alpha} - \sum_\beta P_\alpha \Omega_{\alpha\beta}, \tag{2.32}$$

where $P_\alpha$ is the probability of the system to be in a state $\alpha$ at time $t$ and $\Omega_{\alpha\beta}$ is the transition rate from state $\alpha$ to state $\beta$. A state $\alpha$ is specified by a set of site occupations,

$\{\alpha_i\}$, where $\alpha_i = 1(0)$ for an occupied (unoccupied) site $i$, and the matrix $\hat{\Omega}$ can be constructed from rates $\omega_{ij}$.

In particular, for a system with only one charge carrier, each state is uniquely characterized by the index $i$ of the site the carrier occupies. In other words, only states of type $i \equiv \{0, \ldots, 0, \alpha_i = 1, 0, \ldots, 0\}$ are possible, and the corresponding probabilities $P_i$ and the transition rates $\Omega_{ij}$ are identical to site occupation probabilities $p_i$ and the transfer rates $\omega_{ij}$ (as introduced in sec. 2.4), respectively. Eq. 2.32 can then be rewritten as

$$\frac{\partial p_i}{\partial t} = \sum_j p_j \omega_{ji} - \sum_j p_i \omega_{ij}, \tag{2.33}$$

and can be solved using linear algebra. While being efficient for stationary, low charge carrier density cases (one charge carrier per simulation box), this approach can become unstable for systems with high energetic disorder, where rates vary by several orders of magnitude.

In more general cases, such as multiple charge carriers, expressing the state picture (eq. 2.32) in terms of site occupations is required because of extremely large total number of states. For multiple charge carriers, the master equation can still be rewritten in terms of occupation probabilities [64] by assuming only site-blocking charge-charge interactions and by using a mean-field approximation [111]. The analogue of eq. 2.33 becomes, however, non-linear and requires special solvers. If, in addition, several different types of carriers, such as holes, electrons, and excitons are present in the system, as well as their creation/annihilation processes take place, it is practically impossible to link state and site occupation probabilities and the corresponding rates.

Instead, the solution of eq. 2.32 can be obtained by using kinetic Monte Carlo (KMC) methods. KMC explicitly simulates the dynamics of charge carriers by constructing a Markov chain in state space and can find both stationary and transient solutions of the master equation. The main advantage of KMC is that only states with a direct link to the current state need to be considered at each step. Since these can be constructed solely from current site occupations, extensions to multiple charge carriers (without the mean-field approximation), site-occupation dependent rates (needed for the explicit treatment of Coulomb interactions), and different types of interacting particles and processes, are straightforward.

Note that in this thesis we have always simulated charge transport for one carrier in the periodic simulation box. The influence of charge carrier density on macroscopic quantities such as the charge carrier mobility are weak in all systems considered in this thesis due to small energetic disorder [112].

In this case, the KMC simulation starts by randomly choosing a site $i$ where the charge is injected and its total escape rate from this site is computed as

$$\omega_i = \sum_j \omega_{ij}, \tag{2.34}$$

where the sum extends over all neighbors $j$ of site $i$ from the neighbor list. Then, a particular neighbor $k$ is selected according to the variable step size method with a probability

of $\omega_{ik}/\omega_i$, which is done by choosing the biggest $k$ for which

$$\omega_i^{-1} \sum_{j=j_{\min}}^{k} \omega_{ij} \leq r_1. \tag{2.35}$$

where the rates $\omega_{ij_{\min}}, ..., \omega_{ik}, ..., \omega_{ij_{\max}}$ do not have to be sorted and $r_1 \in (0, 1]$ is the first random number. Then the charge is moved to the chosen site $k$ and the time is advanced by $\tau_i$ taking into account the total escape time out of site $i$ according to

$$\tau_i = -\omega_i^{-1} \ln r_2 \,, \tag{2.36}$$

where $r_2 \in (0, 1]$ is the second random number. The cycle then repeats until the total KMC simulation time $t_{\mathrm{KMC}}$ has been reached.

## 2.9 Macroscopic observables

Spatial distributions of charge and current densities can provide a better insight in the microscopic mechanisms of charge transport. If $O$ is an observable which has a value $O_\alpha$ in a state $\alpha$, its ensemble average at time $t$ is a sum over all states weighted by the probability $P_\alpha$ to be in a state $\alpha$ at time $t$

$$\langle O \rangle = \sum_\alpha O_\alpha P_\alpha. \tag{2.37}$$

If $O$ does not explicitly depend on time, the time evolution of $\langle O \rangle$ can be calculated as

$$\frac{d \langle O \rangle}{dt} = \sum_{\alpha,\beta} \left[ P_\beta \Omega_{\beta\alpha} - P_\alpha \Omega_{\alpha\beta} \right] O_\alpha = \sum_{\alpha,\beta} P_\beta \Omega_{\beta\alpha} \left[ O_\alpha - O_\beta \right]. \tag{2.38}$$

If averages are obtained from KMC trajectories, $P_\alpha = s_\alpha / s$, where $s_\alpha$ is the number of Markov chains ending in the state $\alpha$ after time $t$, and $s$ is the total number of chains.

Alternatively, one can calculate time averages by analyzing a single Markov chain. If the total occupation time of the state $\alpha$ is $\tau_\alpha$ then

$$\overline{O} = \frac{1}{\tau} \sum_\alpha O_\alpha \tau_\alpha \,, \tag{2.39}$$

where $\tau = \sum_\alpha \tau_\alpha$ is the total time used for time averaging.

For ergodic systems and sufficient sampling times, ensemble and time averages should give identical results. In many cases, the averaging procedure reflects a specific experimental technique. For example, an ensemble average over several KMC trajectories with different starting conditions corresponds to averaging over injected charge carriers in a time-of-flight experiment. In what follows, we focus on the single charge carrier (low concentration of charges) case.

### 2.9.1 Charge density

For a specific type of particle, the microscopic charge density of a site $i$ is proportional to the occupation probability of the site, $p_i$

$$\rho_i = e p_i / V_i \,, \tag{2.40}$$

where, for an irregular lattice, the effective volume $V_i$ can be obtained from a Voronoi tessellation of space. For reasonably uniform lattices (uniform site densities) this volume is almost independent of the site and a constant volume per site, $V_i = V/N$, can be assumed. In the macroscopic limit, the charge density can be calculated using a smoothing kernel function, i.e. a distance-weighted average over multiple sites. Site occupations $p_i$ can be obtained from eq. 2.37 or eq. 2.39 by using the occupation of site $i$ in state $\alpha$ as an observable.

If the system is in thermodynamic equilibrium, that is without sources or sinks and without circular currents (and therefore no net flux) a condition, known as detailed balance, holds

$$p_j \omega_{ji} = p_i \omega_{ij} \,. \tag{2.41}$$

It can be used to test whether the system is ergodic or not by correlating $\log p_i$ and the site energy $E_i$. For exmaple in one-component systems $\lambda_{ij} = \lambda_{ji}$ and the ratio of forward and backward rates are determined solely by the energetic disorder, $\omega_{ji}/\omega_{ij} = \exp(-\Delta E_{ij}/k_\mathrm{B}T)$ (see eq. 2.6).

### 2.9.2 Current

If the position of the charge, $\vec{r}$, is an observable, the time evolution of its average $\langle \vec{r} \rangle$ gives the total current in the system

$$\vec{j} = e \langle \vec{v} \rangle = e \frac{d \langle \vec{r} \rangle}{dt} = e \sum_{i,j} p_j \omega_{ji} (\vec{r}_i - \vec{r}_j). \tag{2.42}$$

Symmetrizing this expression we obtain

$$\vec{j} = \frac{1}{2} e \sum_{i,j} \left( p_j \omega_{ji} - p_i \omega_{ij} \right) \vec{r}_{ij}, \tag{2.43}$$

where $\vec{r}_{ij} = \vec{r}_i - \vec{r}_j$. Symmetrization ensures equal flux splitting between neighboring sites and absence of local average fluxes in equilibrium. It allows to define a local current through site $i$ as

$$\vec{j}_i = \frac{1}{2} e \sum_{j} \left( p_j \omega_{ji} - p_i \omega_{ij} \right) \vec{r}_{ij}. \tag{2.44}$$

A large value of the local current indicates that the site contributes considerably to the total current. A collection of such sites thus represents most favorable charge pathways.

### 2.9.3 Mobility and diffusion constant

For a single particle, e.g. a charge or an exciton, a zero-field mobility can be determined by studying particle diffusion in the absence of external fields. Using the particle displacement squared, $(\Delta\vec{r}_i)^2$, as an observable we obtain

$$2dD_{\gamma\delta} = \frac{d\left\langle \Delta r_{i,\gamma}\Delta r_{i,\delta}\right\rangle}{dt} = \sum_{\substack{i,j\\ i\neq j}} p_j\omega_{ji}\left(\Delta r_{i,\gamma}\Delta r_{i,\delta} - \Delta r_{j,\gamma}\Delta r_{j,\delta}\right) = \sum_{\substack{i,j\\ i\neq j}} p_j\omega_{ji}\left(r_{i,\gamma}r_{i,\delta} - r_{j,\gamma}r_{j,\delta}\right) . \tag{2.45}$$

Here $\vec{r}_i$ is the coordinate of the site $i$, $D_{\gamma\delta}$ is the diffusion tensor, $\gamma,\delta = x,y,z$, and $d = 3$ is the system dimension. Using the Einstein relation,

$$D_{\gamma\delta} = k_{\mathrm{B}}T\mu_{\gamma\delta}\,, \tag{2.46}$$

one can, in principle, obtain the zero-field mobility tensor $\mu_{\gamma\delta}$. Eq. 2.45, however, does not take into account the use of periodic boundary conditions when simulating charge dynamics. In this case, the simulated occupation probabilities can be compared to the solution of the Smoluchowski equation with periodic boundary conditions [64].

Alternatively, one can directly analyze time-evolution of the KMC trajectory and obtain the diffusion tensor from a linear fit to the mean square displacement, $\overline{\Delta r_{i,\gamma}\Delta r_{i,\delta}} = 2dD_{\gamma\delta}t$.

The charge carrier mobility tensor, $\hat{\mu}$, for any value of the external field can be determined either from the average charge velocity defined in eq. 2.42

$$\langle\vec{v}\rangle = \sum_{i,j} p_j\omega_{ji}(\vec{r}_i - \vec{r}_j) = \hat{\mu}\vec{F}\,, \tag{2.47}$$

or directly from the KMC trajectory. In the latter case the velocity is calculated from the unwrapped (if periodic boundary conditions are used) charge displacement vector divided by the total simulation time. Projecting this velocity on the direction of the field $\vec{F}$ yields the charge carrier mobility in this particular direction. In order to improve statistics, mobilities can be averaged over several KMC trajectories from different injection points and MD snapshots.

### 2.9.4 Convergence of mobility

In the previous part of this chapter we have introduced several computational parameters that influence the accuracy and efficiency of charge-transport simulations including a cutoff radius $r_{\mathrm{nb}}$ for the neighborlist construction, a cutoff $r_{\mathrm{el}}$ for polarized electrostatic interactions and the KMC simulation time $t_{\mathrm{KMC}}$.

In this section we investigate the convergence of the charge-carrier mobility with respect to these parameters and also discuss finite-size effects that have to be considered when extrapolating to experimental system sizes (typically layer thicknesses are at least 100 nm).

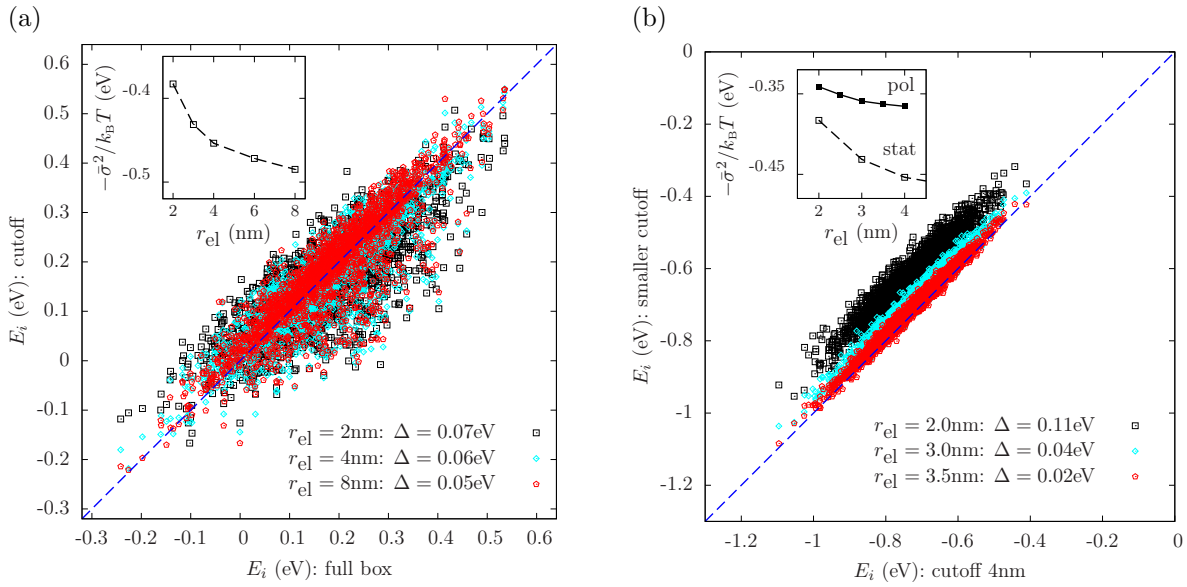


**Figure 2.14.** Cutoff dependence of individual electrostatic energies for electron transport in system with $L = 16$nm containing 4096 BTDF molecules. (a) Static ($\epsilon_s = 1$) contributions determined with a cutoff $r_{el}$ are compared to energies from the full box (nearest image convention). Root mean square deviation $\Delta$ shows slow convergence, which leads to slow convergence of the transport energy $E_\infty = -\bar{\sigma}^2/k_BT$ shown in the inset. (b) Same as (a) but now including polarization interactions using the Thole model which leads to faster convergence due to screening. Instead of the full box, energies are compared to a simulation with $r_{max} = 4\,$nm.

## Cutoff dependence of electrostatic energies

Introducing a cutoff $r_{el}$ for calculation of electrostatic site energies can be necessary for large system sizes to speed up calculations. It restricts the number of neutral molecules surrounding the molecule whose site energy is to be computed. The first criterion for convergence of electrostatic interactions including polarization is the site-energy differences from the neighborlist, where $r_{el} = 2\,$nm is sufficient due to the spatial correlations. In KMC simulations, where the charge carrier is randomly injected at the beginning of the simulations, the equilibrium transport energy [113] also has to be reached. It is defined in terms of inverse temperature $\beta = (k_BT)^{-1}$ as

$$E^{equ} = \frac{\int_{-\infty}^{+\infty} p(E) E \exp(-\beta E)\, dE}{\int_{-\infty}^{+\infty} p(E) \exp(-\beta E)\, dE}, \tag{2.48}$$

and represents the energy a charge carrier relaxes to after it has been randomly injected into a site-energy distribution $p(E)$. In case of a Gaussian distribution of individual (uncorrelated) site energies with zero mean and width $\bar{\sigma}$ the transport energy is $E^{equ} = -\beta\bar{\sigma}^2$. Therefore, using a cutoff radius $r_{el}$, which does allow to converge the site-energy differences of the neighborlist, but is too small to converge electrostatic interactions for the *individual*

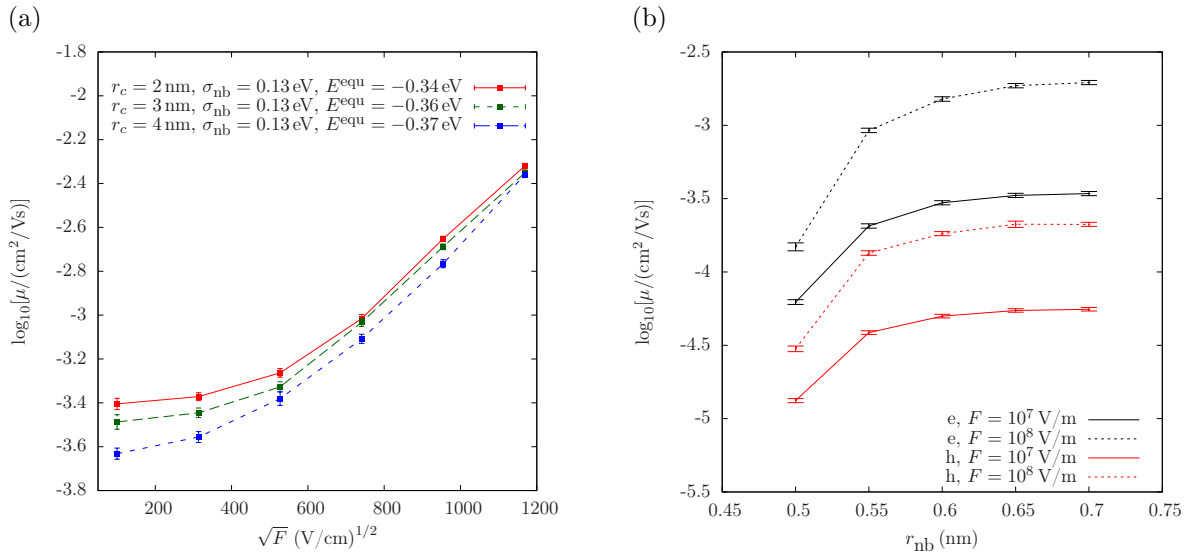


**Figure 2.15.** Convergence of mobility in system of 4096 BTDF molecules. (a) Poole-Frenkel plots for electron transport for different $r_{\mathrm{el}}$ used for polarized site-energy calculations show that although site-energy differences ($\sigma_{\mathrm{nb}}$) are converged at $r_{\mathrm{el}} = 2\,\mathrm{nm}$, unconverged transport energy $E^{\mathrm{equ}}$ leads to slight overestimation of mobility for small electric fields. (b) A neighborlist cutoff of $r_{\mathrm{nb}} = 0.7\,\mathrm{nm}$ between centers of mass of rigid fragments yielding 30.000 pairs is sufficient to converge mobilities. All mobilities in a and b are averaged over ten KMC runs with different injection points and six directions of the field. In case of b, averages are obtained from two independent MD snapshots while only one snapshot is used for a. Errors for the mean of the mobility are taken from a bootstrap analysis with 10.000 data sets. Conformational disorder has been neglected in a and b.

site energies leads to underestimation of $\bar{\sigma}$ which leads to overestimation of $E^{\mathrm{equ}}$ and higher mobilities.

To investigate the convergence of the individual site energies we first analyze the unscreened electrostatic contributions (eq. 2.24 with $\epsilon_{\mathrm{s}} = 1$) which are shown for different cutoff radii in fig. 2.14.a with respect to the energies evaluated using the whole box containing 4096 BTDF molecules (nearest image convention). Due to the long-range nature of the charge-dipole interaction, which is proportional to $r^{-2}$, the convergence of the individual energies is slow, which leads to slow convergence of $E^{\mathrm{equ}}$ as shown in the inset of fig. 2.14.a.

Next we include polarization effects using the Thole model described in sec. 2.7.3. As evaluation of the polarization contributions for a box of $N = 4096$ BTDF molecules becomes computationally prohibitive due to $N^2$ interactions in the self-consistency loop, we compare the individual site energies using different cutoff radii to energies obtained using $r_{\mathrm{el}} = 4\,\mathrm{nm}$. Figure 2.14.b shows that energies systematically shift to lower values with increasing cutoff radius since more polarizable material is available to stabilize the charge. Note that since the interaction of the charge with the induced dipole is proportional to $r^{-4}$, this shift does not increase much for $r_{\mathrm{el}} > 3.5\,\mathrm{nm}$. As compared to the static case, the

convergence of individual site-energy distributions is much faster which, in turn, speeds up the convergence of $E^{\mathrm{equ}}$ as shown in the inset of fig. 2.14.b. This speed-up is due to the fact that at long distances the screening reduces the charge-dipole interactions.

In order to investigate the dependence of mobility on the cutoff radius, we have performed KMC simulations with one charge carrier in the box of 4096 BTDF molecules using the polarized site energies from the Thole model obtained with different $r_{\mathrm{el}}$. As shown in fig. 2.15.a, the mobility converges rather fast indicating that $r_{\mathrm{el}} = 3\,\mathrm{nm}$ is sufficient for simulations at moderate electric fields, while a slight overestimation of mobilities (with respect to $r_{\mathrm{el}} = 4\,\mathrm{nm}$) can still be seen in case of small electric fields and is due to not completely converged $\bar{\sigma}$ and $E^{\mathrm{equ}}$.

## Cutoff dependence of the neighborlist

The list of neighbors for computation of hopping rates is based on a cutoff distance between centers of mass between rigid fragments as introduced in fig. 2.6. In case of BTDF the phenyl groups and the dibenzofurane cores constitute seven rigid fragments. The dependence of the simulated electron and hole mobilities on this cutoff is shown in fig. 2.15.b indicating that a value of $r_{\mathrm{nb}} = 0.7\,\mathrm{nm}$ is sufficient for convergence. The neighborlist then contains about 30.000 pairs for which transfer integrals are evaluated using the PBE functional, the TZVP basis set, and the dimer projection method [83, 92].

## KMC simulation time dependence

We have also checked the convergence of mobility with respect to the total KMC simulation time $t_{\mathrm{KMC}}$.As can be seen from fig. 2.16.a, too short KMC simulation times lead to higher mobilities since the charge carrier that has been randomly injected in the density of states has not relaxed to the transport energy $E^{\mathrm{equ}}$, which is in the tail of the density of states. Due to relatively small energetic disorder in BTDF, this equilibration is fast so that mobility is converged after $t_{\mathrm{KMC}} >= 10^{-5}\,\mathrm{s}$ for electrons and $t_{\mathrm{KMC}} > 10^{-4}\,\mathrm{s}$ for holes, which corresponds to crossing the simulation box a few thousand times.

## System size effects

Predictions of charge-carrier mobilities in partially disordered semiconductors rely on charge transport simulations in systems which are only several nanometers thick. As a result of too small system sizes, the simulated mobility in materials with large energetic disorder decreases with increasing system size and the transport is said to be dispersive [114, 115]. If the system size is large enough, charge transport is non-dispersive meaning that mobility does not depend on the system size.

In order to understand the concept of dispersive mobility, let us consider a Gaussian distribution of site energies $p(E)$, from which $i = 1...N$ site energies $E_i$ are drawn that represent the site energies of $N$ molecules in the simulation box. Even in infinitely large systems (obtained from periodic boundary conditions), only $N$ *different* site energies are

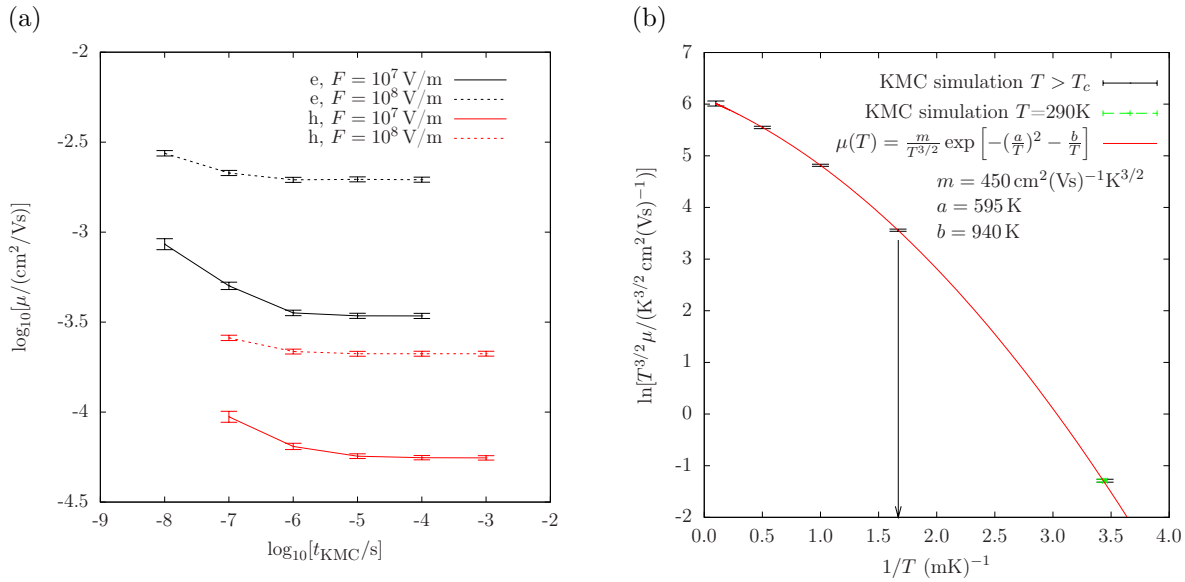


**Figure 2.16.** (a) Dependence of mobility $\mu$ on the duration $t_{\mathrm{KMC}}$ of the KMC simulation for 4096 BTDF molecules for holes ($h$) and electrons ($e$) at small and high values of the external field $F$. (b) Temperature dependence of mobility. Simulations are performed for holes in the interval from 10.000 K to 290 K. The extrapolation of the fit (red) obtained for points above $T_c = 600\,\mathrm{K}$ (black arrow) confirms that charge transport is non-dispersive up to room temperature (green). All mobilities in (a) and (b) are averaged over ten injection points and six directions of the field and two independent MD snapshots. Error bars are taken from a bootstrap analysis with 10.000 data sets. Conformational disorder has been neglected in a and b.

accessible since all periodic images of a molecule have the same energy. In this case, there are only a few (depending on $N$) states with very low lying energy, and the charge carrier relaxes to a system size dependent transport energy $E_N^{\mathrm{equ}}$, which is higher compared to $E^{\mathrm{equ}}$ resulting from a system with an infinite amount of different site energies (where the low lying energies in $p(E)$, that have the largest weight due to the Boltzmann factor, are perfectly sampled)

$$E_N^{\mathrm{equ}} = \frac{\sum_i^N E_i \exp\left(-\beta E_i\right)}{\sum_i^N \exp\left(-\beta E_i\right)} > E^{\mathrm{equ}} = \frac{\int_{-\infty}^{+\infty} p(E) E \exp\left(-\beta E\right) dE}{\int_{-\infty}^{+\infty} p(E) \exp\left(-\beta E\right) dE}\,. \tag{2.49}$$

The system-size dependent transport energy can result in a mobility decrease with increasing system size $N$ until enough sites are available and transport becomes non-dispersive. Within an uncorrelated Gaussian disorder model, the critical temperature $T_c$, at which the transition from the dispersive to the non-dispersive regime occurs, can be estimated as [55]

$$(\bar{\sigma}/k_{\mathrm{B}}T_c)^2 = -5.7 + 1.05\ln(N)\,. \tag{2.50}$$

Here $\bar{\sigma}$ is the width of the Gaussian-distributed individual site energies, $N$ is the number of sites visited during the KMC run, and the natural logarithm is used.

In case of hole transport in BTDF, where $\bar{\sigma} \approx 0.1\,\mathrm{eV}$, it is estimated that the non-dispersive regime sets in for temperatures above $T_c = 600\,\mathrm{K}$ for the biggest simulation boxes we considered ($N = 4096$ molecules). This implies that when KMC simulations are performed at room temperature, the mobility might still be dispersive. Since computation of transfer integrals and site energies is very time consuming for larger system sizes, we can obtain the non-dispersive mobility by exploiting the fact that the relevant parameter in eq. 2.50 is $\bar{\sigma}/(k_\mathrm{B}T)$ and using temperature-based extrapolation [55].

In this approach, one needs to perform KMC simulations at temperatures above $T_c$ but using the morphology and transport parameters $(E_i, J_{ij}, \lambda_{ij})$ obtained at room temperature. Non-dispersive mobilities calculated at these elevated temperatures can then be used in combination with an analytical result for the temperature dependence [109, 116, 117] to extrapolate mobilities to a desired temperature below $T_c$. We have used the following temperature dependence with the parameters $m, a, b$ derived in a one-dimensional model [55]

$$\mu(T) = \frac{m}{T^{3/2}} \exp\left[-\left(\frac{a}{T}\right)^2 - \frac{b}{T}\right] . \tag{2.51}$$

For BTDF, the non-dispersive mobilities for $T > T_c = 600\mathrm{K}$ are shown in fig. 2.16.b together with a fit of these data points using eq. 2.51. We also show the simulated data point at room temperature and find that it agrees well with the result of the extrapolation. This indicates that the room-temperature mobility simulated for $N = 4096$ is already converged with respect to the system size.

# Chapter 3

# Charge transport in amorphous systems

Organic semiconductors are used as building blocks of various electronic devices such as low cost organic field effect transistors (OFET), lightweight organic photovoltaic cells (OPVC) and flexible organic light emitting diodes (OLED). In contrast to OFET that still suffer from low switching frequencies and OPVC where the power conversion is low, OLEDs based on vacuum-deposited small molecules have already entered the market of flat panel displays and lighting applications [118, 119]. In spite of successful commercialization, the field still faces a number of problems such as the insufficient stability [28] especially for OLEDs based on deep blue emitters [29, 30] with wavelength of $\lambda < 460$nm. In an OLED, several life-time limiting processes can occur during its operation: if the injection of electrons and holes into the emission layer is unbalanced or if their mobilities differ by several orders of magnitude, their recombination takes place in a narrow emission zone at the interface of the emission layer with one of the injection layers. Molecules in this zone are then exposed to high (energetic) stress which can lead to a chemical reaction and device degradation. The morphology of the emission layer also needs to be amorphous in order to prevent the formation of current filaments, which would occur in a crystal structure and would again result in high (electric) stress on certain molecules.

In this chapter we perform microscopic simulations of charge dynamics in (multi-component) amorphous phases of organic materials using the methods introduced in ch. 2.

After explaining the multi-layer structure of an OLED and introducing the basic physical processes occurring in its emission layer (sec. 3.1), we analyze charge transport in pure 2,8-bis(triphenylsilyl)dibenzofurane (BTDF), which has already been introduced in the previous chapter. The amorphous phase of this molecule is used as the electron-transporting layer and as the matrix material for the emission layer of a blue OLED. In sec. 3.2 we discuss the effect of substituents attached to the aromatic dibenzofurane core. By analyzing the electronic structure of BTDF we show that small delocalization effects lead to large electronic coupling elements between neighboring molecules and hence improved mobility. In sec. 3.3, we analyze a host-guest system composed of BTDF doped with a blue triplet emitter [30] forming the emission layer of the OLED. There, we concentrate on the effect of

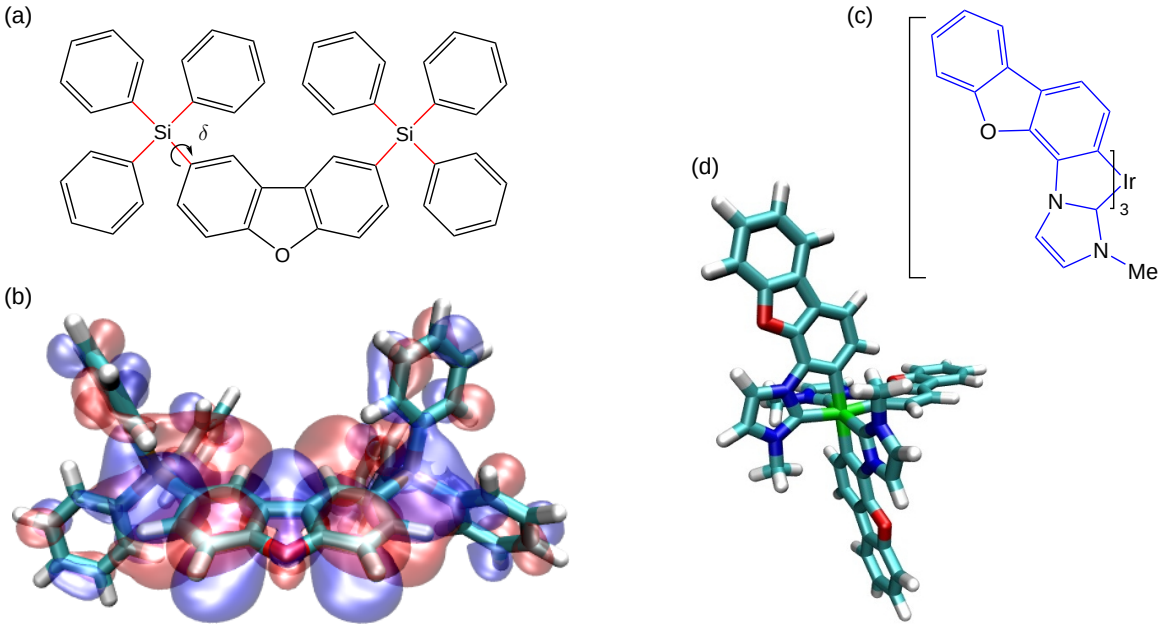


**Figure 3.1.** Materials used in the emission layer of organic light emitting diodes. (a) Chemical structure of host molecule BTDF consisting of a dibenzofurane core and triphenylsilyl substituents that can rotate due to soft dihedrals $\delta$ (red). (b) Isosurfaces of the LUMO using a value of $\pm 0.007$ a.u. allowing to visualize small fractions of orbital density delocalized from the core over the Si-atom to the substituents. (c) Chemical structure of guest molecule acting as deep blue triplet emitter and (d) representation of its meridional isomer used in our simulations.

polarization on the relative site energies of host and guest molecules and consequences for charge transport. Chemical structures for the host and the emitter tris[(1,2-dibenzofurane-4-ylene)(3-methyl-1/1-imidazole-1-yl-2(3/1)-ylidene)]Ir(III) are shown in fig. 3.1.

Although the focus here is on OLEDs in which films of small molecules are used, our findings are also applicable to other devices such as OFET or OPVC.

## 3.1 Basic physical processes in OLEDs

A prototypical OLED is a multi-layer structure which is shown in fig. 3.2.a. Every layer bears a certain task: electrons are injected from a metallic cathode, holes are injected on the opposite side of the OLED from a transparent anode, typically made of indium tin oxide (ITO). Transport layers (which may be doped) allow for energy alignment of the organic semiconductors and the electrodes and provide a balanced charge transport into an emission layer (EML). Additional blocking layers are used to confine charge carriers to the EML facilitating their efficient radiative recombination.

The EML itself consists of a charge-transporting organic semiconductor and an emitter. The main processes occurring in the EML are shown in fig. 3.2.b. Holes and electrons

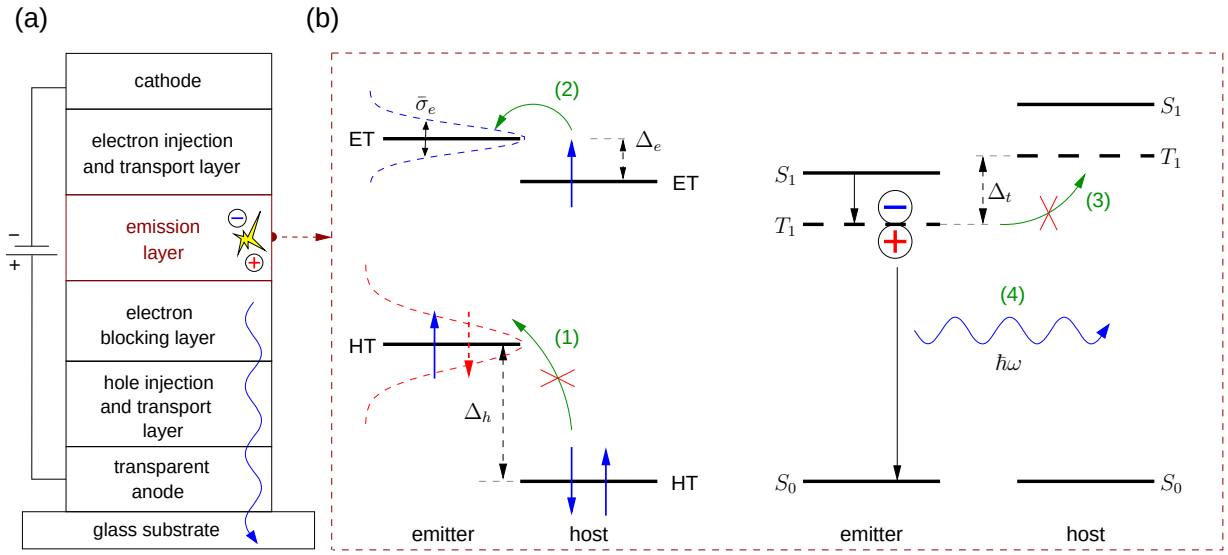


**Figure 3.2.** (a) Multi-layered structure of a phosphorescent OLED with an electron-conducting host and a hole-conducting emitter. (b) Relative alignment of hole (HT) and electron (ET) transport levels of emitter and host and their broadening $\bar{\sigma}$ (right) and energy levels of singlets ($S$) and triplets ($T$) of the emitter emission spectrum and the host excitation spectrum (left). The following processes are shown : (1) Hole transfer from emitter to host is avoided by a large barrier, $\Delta_h$. (2) Electron transfer to the neutral emitter is prevented by the barrier $\Delta_e$. In order to ensure exciton formation on the emitter, $\Delta_h \gg E_{\mathrm{Coul}} > \Delta_e$, where $E_{\mathrm{Coul}}$ is the Coulomb attraction between the hole on the emitter and the electron on the neighboring host. (3) Transfer of the exciton from the emitter to the host is avoided by the barrier $\Delta_t$ for triplet excitons. (4) Carrier recombination results in emission of blue light.

have to be injected from either side into the emission layer. In case of a large band-gap emitter, its small electron affinity makes injection of electrons from the cathode to the *emitter* difficult. Therefore, the *host* is used as the electron transporting material, and the corresponding electron-transport level (ET) has to be below that of the emitter resulting in an energy barrier $\Delta_e$ between host and guest. On the other hand, injection of holes then occurs into the emitter molecule where the corresponding transport level (HT) can more easily be energetically aligned with the Fermi level of the anode.

There are two ways of forming an exciton in the EML. First, electrons and holes can form excitons on a *host* molecule with a subsequent energy transfer of the exciton to the emitter. Alternatively, hole transport can be restricted to emitter molecules by introducing a large energy barrier $\Delta_h$. In this case, a hole on the emitter can attract a charge of the opposite sign from the host and a neutral exciton will be formed directly on the emitter. This direct charge transfer to the emitter leads to more efficient OLEDs than the excitation by energy transfer from the host since, due to different spectral overlap, it is difficult to realize at the same time efficient Förster and Dexter energy transfers of singlet excitons (spin $S = 0$) and triplet excitons ($S = 1$), respectively [120–123].

The balance between forming excitons on the host or on the emitter is determined by

the respective energy level alignment of the emitter and the host, and can therefore be rationally designed. In order to ensure exciton formation on the emitter, the Coulomb attraction between the hole on the emitter and the electron on the neighboring host (typically $E_{\mathrm{Coul}} \approx 0.5\,\mathrm{eV}$) should be capable of overcoming the transport barrier $\Delta_e \approx 0.3\,\mathrm{eV}$ for electrons. For holes $\Delta_h > 1.5\,\mathrm{eV}$ so that excitons are only formed on the emitter. In addition, a large energy barrier for the (triplet) excitons, $\Delta_t$, prevents their transfer from the emitter to the host and the re-absorption of the emitted light by the host which is out-coupled through the transparent anode.

In order to be able to convert all excitons that are created in the EML to light, phosphorescent organo-metallic emitters are used. Excitons are formed on the emitter with a ratio of 1:3 between singlets and triplets according to their multiplicity $2S + 1$. In fluorescent emitters, triplets decay non-radiatively so that the internal conversion efficiency of excitons is limited to 25%. On the other hand, phosphorescent emitters that allow for inter-system crossing due to large spin-orbit coupling, can convert singlets to triplets so that all excitons are converted into light independent of their spin state. This process is known as triplet harvesting [121] and allows for internal conversion efficiencies up to 100%.

Note that in order to avoid triplet quenching and triplet-triplet annihilation, the charge-transporting material, as the majority component (host), is doped only with a small amount ($5 - 20\%\,\mathrm{w/w}$) of the emitter (guest). This is necessary because the internal quantum efficiency decreases upon increase of the concentration of the triplet emitter since two triplets can form a double excitation which can result in material degradation or decay non-radiatively or with undesirable wavelength. A uniform light emission requires a homogeneous distribution of emitter molecules in the matrix. Hence, host and guest must be compatible in order to prevent phase-separation. Aggregation is especially pronounced at high emitter concentrations and leads to a red-shift of the emission and a decrease of the luminescence quantum yield.

After having understood the working principle of the OLED and the requirements for the involved materials, we now first address the rational design of the host molecule that is to be used in combination with a deep blue emitter, and then investigate the emission layer in sec. 3.3 focusing always on charge transport.

## 3.2 Design of charge-transport efficient host molecules

The large band gap of deep blue emitters and the resulting high triplet energy dramatically reduces the number of promising compatible host materials since an even higher triplet energy is necessary for the host to ensure trapping of the exciton on the emitter and to prevent the reabsorption of the emitted light [124, 125]. Such a high triplet energy often implies small electron affinity for the host which can result in material degradation when the material is transporting electrons. Also carrier injection into the host then becomes difficult since it requires overcoming large energy barriers between transport layers and the host. This problem can partially be solved by doping the transport layer which leads to band-bending and energy level alignment of host with the electron-transporting layer

and/or cathode.

Among possible charge transporting units with sufficient stability for electron transport and a high triplet energy are dibenzofuranes or N-phenylcarbazoles [126]. Substituents must be attached to these materials for various reasons. First, they are necessary to prevent crystallization [127]. The amorphous morphology of the EML is important for both efficiency and lifetime of an OLED, since crystallinity favors transport along the $\pi$-stacking direction which leads to inhomogeneous charge transport in current filaments resulting in inhomogeneous emission. To avoid crystallization, side groups must be sufficiently flexible and bulky. For example, 2,9-dimethyl-4,7-diphenyl-1,10-phenanthroline (BCP) crystallizes because its substituents are too small. Second, large substituents suppress emitter aggregation, and therefore facilitate a uniform light emission while at the same time reducing shifts in the wavelength and non-radiative losses. Hence, host and guest must be compatible in order to prevent phase separation, which, in our case, is achieved by using the dibenzofurane core as a building block of both host and guest molecules, as shown in fig. 3.1. Aggregation is especially pronounced at high guest concentrations and can lead to a red shift of the emission wavelength due to strong interactions between the $\pi-$systems of the emitters which leads to a splitting of HOMO and LUMO and a lower bandgap. Third, substituents can be used to optimize the molecular weight of the host for vacuum deposition where, as a rule of thumb, molecular weights below 1000 u are suitable since the thermal energy that the substrate is transferring to the molecules at a given temperature has to be sufficient to overcome the absorption energy. Note that large molecules often have a large number of internal degrees of freedom so that the thermal energy of the substrate is not fully converted into kinetic energy and the evaporation is more difficult.

The main role of the substituents, however, is to adjust the relative positions of electron and hole transporting levels as well as singlet and triplet excited states of the host to those of the emitter which are shown in fig. 3.2.b. In case of dibenzofurane for example, the high triplet energy implies a high electron transporting level, which has to be adjusted below the level of the emitter by attaching substituents in order to ensure electron transport by the host. Synthetically, level adjustment can be achieved by inductive effects [128], when strongly electronegative substituents (e.g. trifluoromethyl) are used. An alternative approach is to exploit the mesomeric effect [128], when the frontier orbital densities delocalize (by using e.g. triphenylsilyl substituents). In case of the BTDF host molecule shown in fig. 3.1.a, two triphenylsilyl groups are attached to an aromatic core, which lowers the electron transport level of the host below the one of the emitter while keeping its triplet energy above the emitter. In addition they are sufficiently bulky to prevent crystallization. However, apart from a suitable level alignment, processability, amorphous structure and stability, an adequate charge carrier mobility of the host is required in order to prevent ohmic losses.

Due to its complexity, the effect of the attached substituents on charge carrier mobility has rarely been addressed. It is obvious that bulky substituents can lead to large spatial separations of $\pi$-conjugated systems of neighboring molecules. Since electronic couplings decrease exponentially with intermolecular separations, one might expect very poor charge carrier mobility of the host. The aim of this section is to show that the use of the mesomeric

effect can remedy the situation by delocalizing the frontier orbitals over the substituents. To do this, we perform charge-transport simulations to quantify the influence of transport parameters such as reorganization energy and site-energy disorder in sec. 3.2.1 and analyze the influence of the mesomeric effect on transfer integrals in sec. 3.2.2. In order to formulate design rules for charge-transport efficient host materials in sec. 3.2.4 we have to compare our findings to experimental data from admittance spectroscopy in sec. 3.2.3, because the widely used time-of-flight (TOF) technique cannot be applied in case of BTDF which we now explain. In TOF, the organic semiconductor is sandwiched between two electrodes and charges are photo-excited in the organic material using a laser pulse. Let us assume that hole mobilities are to be measured. Then the anode (positive electrode) has to be transparent, and due to the absorption of the organic material, charges are generated near the anode. The negative charges are then directly extracted which leads to a large current signal directly after the excitation. Under the influence of an applied field $F$ the holes are drifting towards the cathode (negative electrode) and the current is time-independent until the holes have reached the cathode. Therefore the current starts to decay for times larger than the transit time $\tau$. The hole mobility can then be extracted from the transit time and the sample thickness $L$ according to $\mu = \tau/(FL)$. Note that in order to be able to accurately determine $\tau$, the sample thickness has to be large enough to be in the non-dispersive regime (see sec. 2.9.4). Otherwise the finite penetration depth of the laser beam leads to different mobilities for charges depending on where in the sample they are generated since the mobility for each charge depends on the distance it travels before extraction.

In case of BTDF layer thicknesses of $d > 1\,\mu$m would be necessary, while in OLEDs films with $d < 200\,$nm are typically used. Furthermore, in case of BTDF, doped interlayers are necessary to adjust the transport levels of the organic material to that of the electrodes to allow for efficient extraction of the charges, and these interlayers absorb at the excitation wavelength of the large band gap organic material which makes photo-excitation impossible.

In contrast to TOF, admittance spectroscopy is independent of light absorption and can be used to extract the mobility of thin organic films sandwiched between electrodes. This is done by applying a small $ac$ voltage in addition to a $dc$ voltage and investigating the capacitance of the device in the frequency domain to find the transit time as explained in sec. 3.2.3.

### 3.2.1 Charge-transport simulations

To relate charge carrier mobility to the chemical structure the methodology introduced in ch. 2 is applied to the BTDF system. First, atomistic molecular dynamics (MD) is used to simulate material morphology and then charge-transfer rates between neighboring molecules $i$ and $j$ are evaluated from reorganization energies, site energies and transfer integrals using the high-temperature limit of Marcus theory (eq. 2.6), as explained in ch. 2. The rates and molecular centers of mass are used in kinetic Monte Carlo (KMC) simulations to solve the master equation for a charge drift-diffusing in a box with periodic boundary

conditions in an applied electric field $F$. The charge carrier mobility is then determined as $\mu = \langle v \rangle / F$, where $\langle v \rangle$ is the averaged projection of the carrier velocity on the direction of the field. Simulated mobilities are averaged over two independent MD snapshots, ten injection points, and six different spatial directions of the field. We have discussed the convergence of the mobility with respect to different simulation parameters such as cut-off radius for a neighborlist, cut-off radius for electrostatic interactions including polarization, KMC simulation time and box size in sec. 2.9.4.

### Morphology

An amorphous morphology of 4096 BTDF molecules is obtained by first annealing the system at 700 K, well above the glass transition temperature, $T_g = 380\,\mathrm{K}$, followed by fast quenching to room temperature, as explained in sec. 2.2. This leads to a representative system with a density that agrees reasonably well with experiment as shown in sec. 2.2 although partial crystallization or non-equilibrium effects can not be investigated since this would require much larger time scales. The final length of the cubic box is $L = 16\,\mathrm{nm}$. To determine charge hopping rates in this morphology, a neighborlist based on the closest approach of centers of mass between phenyl rings or dibenzofurane cores is constructed using a cutoff of 0.7 nm. The parameters entering the rate expression are then calculated for each molecular pair from the neighborlist.

Since BTDF has soft degrees of freedom, such as dihedrals $\delta$ in fig. 3.1.b, molecules in the amorphous phase have different conformations as indicated in the inset of fig. 3.3a. These conformations are frozen on the time scale of charge transport, as shown in sec. 2.2. Reorganization energies $\lambda_{ij}$ and internal (conformational) energy differences $\Delta E_{ij}^{\mathrm{int}}$ are therefore computed from potential energy surfaces of 512 molecules with geometries taken from the MD simulation making use of density functional theory (DFT).

### Reorganization energy

We find a small variance of the reorganization energy due to conformational changes. Since such a small variation does not affect the mobility we use the mean values of $\lambda_{e(h)}^{\mathrm{BTDF}} = 0.19(0.27)\,\mathrm{eV}$ for electrons (holes). As the bare dibenzofurane has $\lambda_e^{\mathrm{DBF}} = 0.27\,\mathrm{eV}$, attaching the triphenylsilyl groups increases electron hopping rates roughly by a factor of $\sqrt{\frac{\lambda_e^{\mathrm{DBF}}}{\lambda_e^{\mathrm{BTDF}}}} \exp\left(-\frac{\lambda_e^{\mathrm{BTDF}} - \lambda_e^{\mathrm{DBF}}}{4 k_{\mathrm{B}} T}\right) \sim 3$ (see also eq. 4.6), which can be explained in terms of delocalization effects [82]. The reorganization energy for holes is similar in BTDF and the bare dibenzofurane. Note that the mean $\langle \lambda_{e(h)} \rangle$ from the distribution of reorganization energies deviates from the value obtained in molecular geometries that can freely relax, $\lambda_{e(h)}^{\mathrm{free}} = 0.16(0.34)\,\mathrm{eV}$.

### Site-energy distributions

The distributions of conformational energy differences, $\Delta E_{e(h)}^{\mathrm{int}}$, are of Gaussian type with a moderate variance of $\sigma_{e(h)}^{\mathrm{int}} = 0.04(0.05)\,\mathrm{eV}$ and are uncorrelated in space, which allows

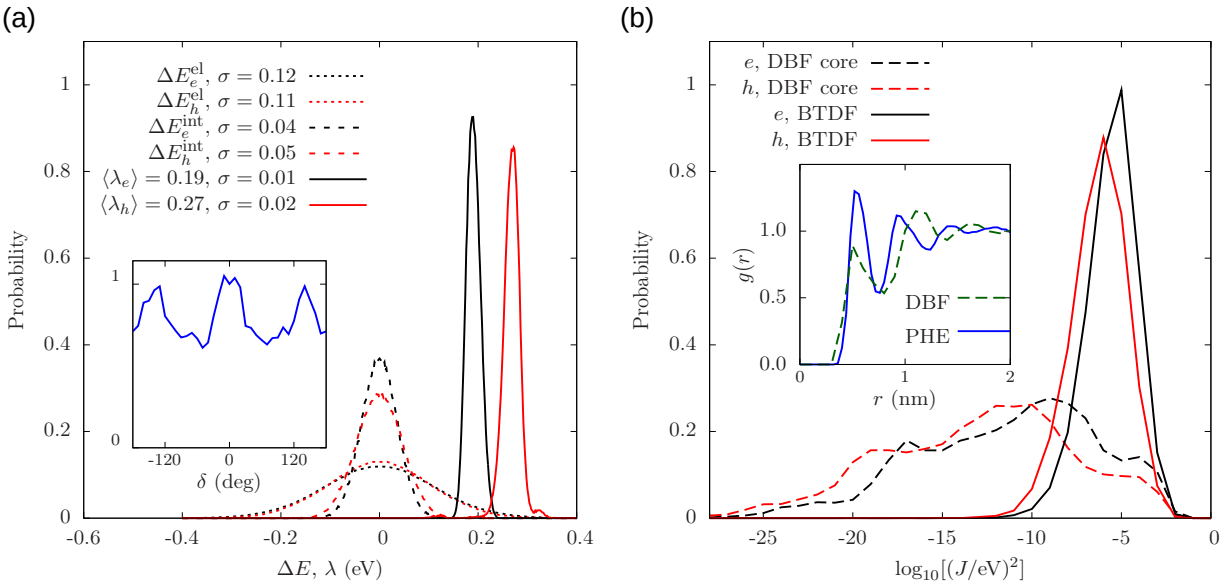


**Figure 3.3.** (a) Distributions of differences in electrostatic energies including polarization, $\Delta E_{e(h)}^{\mathrm{el}}$ (from a neighborlist), internal (conformational) energies, $\Delta E_{e(h)}^{\mathrm{int}}$ and reorganization energies, $\lambda_{e(h)}$ for electrons (holes). Mean and variance $\sigma$ given in eV. Inset shows the distribution of the dihedral angle $\delta$ introduced in fig. 3.1.c. (b) Distributions of the logarithm of the transfer integral $J$ for electron and hole transport constructed from diabatic states based on dibenzofurane (DBF) core or using the whole molecule (BTDF). The same neighborlist and morphology of 4096 BTDF molecules was used for all distributions. Inset: radial distribution functions $g(r)$ of the centers of mass of the DBF core (DBF) and of phenyl rings of the triphenylsilyl groups (PHE).

us to draw them from such a distribution in the larger box of 4096 molecules. Simulations are then additionally averaged over two realizations of this disorder.

Electrostatic contributions to site-energy differences are calculated using partial charges for charged and neutral molecules in the ground state obtained from DFT. Polarization contributions are taken into account self-consistently using the Thole model [104, 106] with a cutoff of 3.5 nm between molecular centers of mass (see sec. 2.7). This results in polarized electrostatic site-energy differences from the neighborlist, $\Delta E_{e(h)}^{\mathrm{el}}$, that are Gaussian distributed with a variance of $\sigma_{e(h)}^{\mathrm{el}} = 0.12(0.11)\,\mathrm{eV}$. This is a rather small energetic disorder which is due to small variations of atomic partial charges (local dipole moments) and the small total dipole moment of BTDF. The bare dibenzofurane has a total dipole moment of $d = 0.7\,\mathrm{D}$, while adding the triphenylsilyl groups slightly increases it to $d = 0.8\,\mathrm{D}$ with a conformational disorder in an amorphous morphology of $\sigma_d = 0.1\,\mathrm{D}$. Since the energetic disorder is proportional to the dipole moment (see eq. 2.22), the attachment of the substituents does not lead to a significant increase of energetic disorder. All distributions are shown in fig. 3.3.a.

### 3.2.2 Mesomeric delocalization effects

The remaining ingredient entering the rate expression is the transfer integral $J$, which relies on the definition of diabatic states of a pair of molecules. The latter are usually constructed from representative orbitals of the $\pi$-conjugated parts, since the effect of attached substituents on the diabatic states is rather small (e.g. in case of alkyl or glycole side-chains [51, 61, 129]). Following this approach, the diabatic states are evaluated by substituting triphenylsilyl by a hydrogen (without modifying the rest of the morphology). Consequently, reorganization energies of the dibenzofurane core ($\lambda^{\mathrm{DBF}}$) are used and transfer integrals are then calculated on DFT level with the PBE functional and a TZVP basis set using the dimer projection method [83, 92]. The distribution of the logarithm of transfer integrals $J$ for pairs of the neighbor list is very broad and is peaked at small values as shown in fig. 3.3.b. This can be rationalized in terms of morphology, as the transfer integral depends exponentially on the intermolecular separation. The distance between the dibenzofurane cores is large because of the attached bulky substituents, as illustrated by the radial distribution function for centers of mass of dibenzofurane cores, shown in the inset of fig. 3.3b. The onset of this function is at ca. 0.5 nm and has a peak $g(r) > 1$ at a separation larger than 1 nm, which eventually leads to the broad distribution of $J$. The small number of high transfer integrals due to a few close-lying cores is apparently not sufficient to form a percolation network of high rates necessary for efficient charge transport. As a consequence, simulations predict low mobilities at experimentally relevant electric fields, $\mu_{e(h)} < 4 \cdot 10^{-7}(3 \cdot 10^{-8})\,\mathrm{cm}^2/\mathrm{Vs}$, which would lead to ohmic losses and poor device performance.

The above made assumptions on the nature of the diabatic states seem logical but are ultimately invalid. Indeed, if the diabatic states are constructed using the frontier orbitals of the entire BTDF molecule, the distributions of transfer integrals become significantly less broad and are peaked at much larger values as shown in fig. 3.3.b. As a result, predicted mobilities are much higher, $\mu_{e(h)} \sim 5 \cdot 10^{-4}(10^{-5})\,\mathrm{cm}^2/\mathrm{Vs}$, which is in agreement with experiments performed by admittance spectroscopy (AS).

### 3.2.3 Comparison to admittance spectroscopy measurements

Admittance spectroscopy (AS) of organic semiconductors allows to characterize electrical properties such as the charge carrier mobility. The theoretical background is based on a simplified system consisting of two electrodes connected by a semiconducting channel formed by the organic layer. A *dc* voltage is applied across the sample and a small *ac* signal at frequency $\omega$ is superimposed. In the space-charge limited current regime [130], the average transit time for charge carriers in the organic film, $\tau$, can be extracted from the maximum of the frequency-dependent negative differential susceptance, $-\Delta B = \omega(C - C_0)$, where $\omega = 2\pi f$ is the angular frequency of the *ac* oscillations, $C_0$ is the capacitance of the organic layer at 0 V and $C$ its frequency-dependent analogue [131]. The transit time $\tau$ allows to evaluate the mobility as a function of the applied voltage according to [130] $\mu^{\mathrm{exp}} = \frac{\langle v^{\mathrm{exp}} \rangle}{F^{\mathrm{exp}}}$, where the mean velocity is given by $\langle v^{\mathrm{exp}} \rangle \sim L/\tau$ and $L$ is the thickness

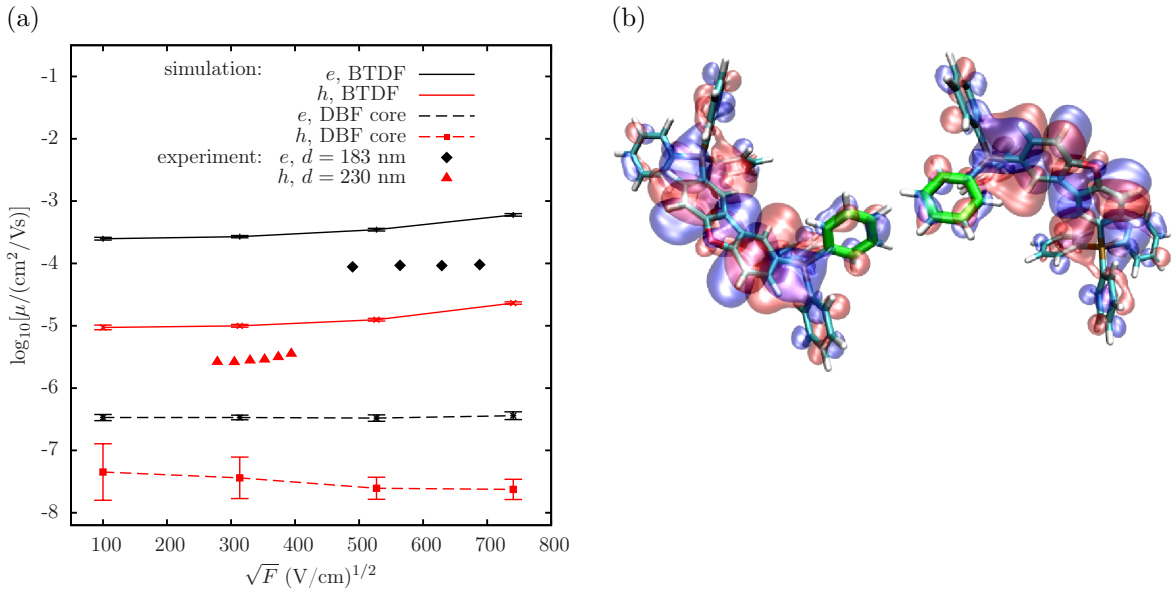


**Figure 3.4.** (a) Simulated electron (black) and hole (red) mobility $\mu$ as function of applied field $F$, with diabatic states based on the whole BTDF molecule (solid) or the DBF core (dashed), respectively. Mobilities are averaged over ten injection points, two MD snapshots, six spatial directions of the field and two realizations of conformational disorder. Error bars are computed from a bootstrap analysis with data sets of 10000 data points. In the scenario where only dibenzofurane cores are taken into account bad connectivity due to small electronic coupling (especially for holes) makes the solution of the master equation difficult which leads to large errorbars in mobility. Experimental data is obtained from admittance spectroscopy at room temperature on films of thickness $d$. (b) Transfer integrals (and consequently mobilities) are boosted by overlap of the delocalized frontier orbitals (here LUMO) on the substituents of neighboring molecules (green).

of the organic film. The field is given by $F^{\text{exp}} = (V - V_b)/L$, where $V$ is the applied $dc$ voltage and $V_b$ is the built-in voltage due to different Fermi levels of the organic material and the electrodes.

Note that the relative dielectric constant $\epsilon_r$ is included in the model used to compute $\langle v^{\text{exp}} \rangle$, while screening of the applied field is not accounted for in simulations. There, the applied electric field $F$ leads to an un-screened site-energy difference of $q\vec{F}\vec{r}_{ij}$ for a charge $q$ hopping between molecules separated by $\vec{r}_{ij}$, which allows to match the mobility computed in linear response of the field to the diffusive mobility from the Einstein relation eq. 2.46. Therefore, in order to compare experimental data to simulations the dielectric constant $\epsilon_r = 2.8$ (from capacitance measurements) was used to obtain the rescaled field-axis $F = F_{\text{exp}}/\epsilon_r$ and mobilities $\mu = \mu_{\text{exp}}\epsilon_r$ from the experimental data points.

Both experimental and simulated mobilities for electrons and holes are shown in fig. 3.4.a. Note that while microscopic charge-transport simulations yield excellent results when comparing relative mobilities, e.g. comparing electrons vs holes in the same compound or

| | LUMO | | HOMO | |
|---|---|---|---|---|
| | DBF | TPS | DBF | TPS |
| HF | 83% | 17% | 97% | 3% |
| PBE | 89% | 11% | 96% | 4% |
| B3LYP | 89% | 11% | 96% | 4% |
| GWA | 90% | 10% | 95% | 5% |

**Table 3.1.** Mulliken population analysis for the localization of the frontier orbitals (LUMO and HOMO) on the dibenzofurane core (DBF) and the triphenylsilyl substituents (TPS). Different quantum chemical methods are employed including Hartree-Fock (HF), density functional theory with the PBE functional or B3LYP functional and the *GW*-approximation [133] all showing that the main part of the orbitals is localized on the dibenzofurane core.

electrons in one compound vs electrons in a similar compound, they usually tend to overestimate the absolute value of mobility as compared to experiment [55, 56, 61, 132].

In BTDF the agreement of experiment and simulations using orbitals from the full BTDF molecule with respect to absolute values of mobilities is reasonably good given the various assumptions made in the charge-transport simulations. These include the creation of the morphology by fast quenching, the choice of the diabatic states (frozen core approximation), the high-temperature limit of the Marcus rate, the strong distance dependence of transfer integrals and the fact that we only have one charge carrier in the simulation box. The relative electron/hole mobilities, however, agree very well between experiment and theory. Simulated electron mobilities are higher compared to holes due to stronger delocalization leading to $\lambda_e < \lambda_h$ and $J_e^2 \gg J_h^2$, while $\sigma_e \approx \sigma_h$ as summarized in fig. 3.3.

### 3.2.4 Rules for the host design

We now discuss the discrepancy between the theoretical approach taking into account contributions to the orbitals on the substituents or neglecting them. The reason for the much higher mobility in the first approach is the mesomeric effect, which delocalizes the frontier orbitals over the silicon atom to the substituents, as shown in fig. 3.1.b. A Mulliken population analysis [134] indicates that a tiny fraction of only 10(4) % of LUMO(HOMO) populates the substituents as shown for different quantum-chemical methods in tab. 3.1.

Although such small delocalization can be easily overlooked on a single molecule level, the effect on electronic couplings is much more pronounced since the substituents are in a closer contact than the cores. This is illustrated in the inset of fig. 3.3.b, where the radial distribution function for centers of mass of phenyl rings is shown. Smaller separations of the phenyl rings boost electronic couplings exponentially, as illustrated in fig. 3.4.b, and therefore dramatically increase charge carrier mobilities.

The charge transfer rate also depends on site-energy differences. It is therefore essential to minimize variations of local dipole moments that would otherwise lead to spatially

correlated energetic disorder [23, 110]. Here the mesomeric effect is also beneficial, since it practically does not change the charge distribution of the conjugated core.

One might argue that the mesomeric effect leads to an additional internal (conformational) disorder of site enegies and reorganization energies due to soft molecular degrees of freedom frozen in an amorphous morphology. This disorder is, however, small compared to the electrostatic disorder, is uncorrelated in space, and has a minor effect on charge transport [64].

To summarize, we suggest using the mesomeric effect to adjust the energy levels via side group attachments to conjugated cores. It substantially improves electronic couplings in the host by delocalizing the frontier orbitals and does not lead to significant additional energetic disorder.

## 3.3 Can lattice models predict the energetic landscape?

Advancements in organic electronics, especially in improving efficiencies and lifetimes of organic light emitting diodes (OLEDs) [119] and solar cells [135], have been stimulated by the synthesis of new materials, optimization of their processing, and a deeper understanding of elementary processes in organic semiconductors. Computer simulations and modeling contributed substantially to this progress [20, 31–33], in particular, lattice models have been successful in rationalizing the influence of finite carrier concentration [34, 35], explicit Coulomb interactions [36], the shape of the density of states [37, 38], site energy spatial correlations [23], and positional disorder [136] on charge and exciton transport dynamics in amorphous materials.

The drawback of lattice models is that they must be parametrized on experimental data and thus do not provide a direct link to underlying chemical structures. Therefore, they cannot aid compound screening, which is becoming more and more important in view of the large number of organic compounds with semiconducting properties [39]. One can, in principle, simulate realistic atomistic morphologies and perform off-lattice Monte Carlo simulations with rates calculated using first principles as explained in ch. 2. This approach is, however, computationally demanding and is limited in accessible system sizes and simulation times [55, 83].

It is therefore tempting to parameterize a lattice model based on calculated electronic properties of single molecules, i.e. to predict site energies from charge distributions, polarizabilities, ionization potentials for internal energies, van der Waals surfaces, etc. While the success of lattice models teaches us that this is possible qualitatively, the question is whether one can *quantitatively* account for a local environment of every molecule, without knowing the details of the (amorphous) material morphology?

To answer this question, we evaluate shifts of the charge-transport levels and the energetic disorder by combining polarizable continuum and lattice models in sec. 3.3.1, where we also incorporate the effect of the polarizability change on the carrier site. In order to

validate the predictions of these mesoscopic models, we then compute site energies using the microscopic approach based on an explicit atomistic morphology in sec. 3.3.2. We finally compare effects of the energy landscape obtained from these two approaches on charge transport in sec. 3.3.3. As a test system, we use a prototypical host-guest mixture of the emission layer of a blue phosphorescent OLED with the materials introduced in fig. 3.1. Note that we use the terms site-energy distribution and density of states (DOS) as synonyms for the distribution of states for one excess charge (electron or hole) in the system, while the more specific term, density of *occupied* states (DOOS) can also be found in the literature.

### 3.3.1 Density of states from mesoscopic models

In this section, contributions to the energy landscape of the host-guest system are evaluated under the assumption that the details of the morphology are not known. Therefore, continuum and lattice models have to be employed allowing only for a mesoscopic description of electrostatic interactions including polarization.

#### Intramolecular contributions

In order to evaluate the free energy of a system with a charge localized on a specific molecule, we first split it according to intra- and intermolecular contributions. The intramolecular part is given by the gas-phase electron affinity (EA) or ionization potential (IP) for electrons and holes, respectively. It is relevant for multi-component systems, since only site-energy differences enter the hopping rate. For the host-guest pair of interest we have computed EAs and IPs using DFT from the energy difference of the charged and neutral molecules allowing for geometry relaxation in both states (see eq. 2.28). The results in tab. 3.2 suggest that the host molecule is responsible for electron transport due to lower lying EA, while holes are transported by the emitter.

#### Polarizable Continuum Model

To partially account for the environment, one can use the dielectric continuum models (PCM) [137] to describe polarization effects. There, a molecule is placed into a cavity (defined by its van der Waals surface) embedded in a homogeneous dielectric and the corresponding Poisson equations inside the cavity and on its surface have to be solved. Since the individual nature of the environment is neglected, the PCM leads only to a shift of the gas-phase levels without broadening. In our case, host and guest have a similar stabilization of the gas-phase EAs and IPs, as presented in tab. 3.2. The energy barrier preventing hole transport from the emitter to the host $\Delta_h = \mathrm{IP}_{\mathrm{host}} - \mathrm{IP}_{\mathrm{emi}} \approx 1.5\,\mathrm{eV}$, and the barrier preventing electron transport from host to the neutral emitter $\Delta_e = \mathrm{EA}_{\mathrm{emi}} - \mathrm{EA}_{\mathrm{host}} \approx 0.4\,\mathrm{eV}$ remain much higher than the thermal energy $k_{\mathrm{B}}T = 0.025\,\mathrm{eV}$.

**Table 3.2.** IPs and EAs calculated from the gas phase and in the PCM with different dielectric constant $\epsilon_r$ for host and guest and the respective energy difference $\Delta$ for hole and electron transport.

| | IP | | | EA | | |
|---|---|---|---|---|---|---|
| | host | emitter | $\Delta_h$ | host | emitter | $\Delta_e$ |
| B3LYP/TZVP (gas phase) | 7.25 | 5.68 | 1.57 | -0.30 | 0.08 | 0.38 |
| B3LYP/TZVP (pcm $\epsilon_r = 3.5$) | 6.55 | 5.12 | 1.42 | -1.20 | -0.81 | 0.39 |
| B3LYP/TZVP (pcm $\epsilon_r = 2.6$) | 6.68 | 5.22 | 1.46 | -1.03 | -0.65 | 0.38 |
| B3LYP/TZVP (pcm $\epsilon_r = 1.5$) | 6.98 | 5.46 | 1.52 | -0.63 | -0.26 | 0.37 |

### Lattice models

To account for *individual* molecular environments in the amorphous phase that lead to the DOS broadening (energetic disorder), we employ lattice models. The lattice is constructed by placing randomly oriented molecules on grid points of a three-dimensional regular lattice, mimicking an amorphous morphology. Molecular electrostatic potentials are then expanded in multipoles and the electrostatic contribution to the DOS is calculated by summing over interactions of these multipoles yielding a distribution of site energies with zero mean $\langle E^{\mathrm{el}} \rangle = 0$ due to rotational symmetry. This model also leads to spatially correlated site energies as neighboring molecules share the same environment, and is often referred to as a correlated disorder model [23, 138].

To account for screening, each site can additionally be assigned an isotropic (molecular) polarizability $\alpha$. This reduces the broadening and leads to a shift of the DOS due to the stabilization of the charge. Within this model [136], the shift of the gas-phase levels due to the interaction of the charge with induced dipole moments on the surrounding lattice sites is $E^{\mathrm{pol}} = -\frac{1}{2}\alpha e^2 \sum_{j\neq 0} r_{0j}^{-4}$, where $e$ is the elementary charge and $r_{0j}$ the distance between the charge and the dipole on lattice site $j$ resulting in stabilization energies up to 1 eV.

Note, however, that the PCM incorporates a full quantum-mechanical description of the charged molecule taking into account all moments of the charge distribution. It can also be applied to large and irregularly formed molecules, while lattice models based on a multipole expansion of the charge distribution are limited to small, quasi-spherical molecules. This is why we believe that, in lack of a realistic morphology, the PCM provides a better estimate of the shift, so that we use IP and EA from the PCM and employ the lattice model only to compute the level broadening as presented in the remaining part of this section.

In line with the central limit theorem, the contribution to the DOS due to interactions of multipole moments of a charged site ($l'$) and the surrounding neutral molecules ($l$) can be approximated by a Gaussian distribution of individual site energies characterized by the width

$$\bar{\sigma}_{l'l} = \frac{\kappa_{l'l}\,\Delta q_{l'} q_l \sqrt{c}}{a^{l'+l+1}\epsilon_{l'}^{\mathrm{eff}}(\alpha)}, \qquad \begin{matrix} l' = 0, 1 \ldots \\ l = 1, 2 \ldots \end{matrix} \tag{3.1}$$

Here, $\Delta q_{l'}$ is the rotationally averaged change of the multipole moment of the carrier site upon charging, and $q_l$ is the rotationally averaged moment of the surrounding molecules

**Table 3.3.** Single molecule parameters for electron transport in the host-guest system. Given are changes in multipole moment $l'$ on the carrier site ($\Delta q_{l'}$) and multipole moments $l$ for surrounding neutral molecules ($q_l$). Dipole moments are calculated with respect to the center of charge. Quadrupole obtained from eigenvalues $Q_k$ of the traceless tensor as $Q = (\frac{2}{3}\sum_k Q_k^2)^{1/2}$. Polarizability volume for charged ($\alpha'$) and neutral molecules ($\alpha$) are defined as $\alpha = \frac{1}{3}\mathrm{Tr}\,\hat{\alpha}$, their difference is the change in polarizability upon charging $\Delta\alpha$.

| | carrier site | host | guest | | neutral | host | guest |
|---|---|---|---|---|---|---|---|
| $\Delta q_0$: | $\lvert q' - q\rvert$ [e] | 1 | 1 | $q_1$: | $d$ [D] | 0.8 | 5.4 |
| $\Delta q_1$: | $\lvert\vec{d'} - \vec{d}\rvert$ [D] | 9.8 | 5.4 | $q_2$: | $Q$ [DÅ] | 5.6 | 39.7 |
| $\Delta\alpha$: | $(\alpha' - \alpha)$ [Å$^3$] | 119 | 219 | $\alpha$: | $\alpha$ [Å$^3$] | 91 | 107 |

as defined in tab. 3.3. Since the surrounding molecules are neutral, the lowest interaction is the charge ($\Delta q_{l'=0} = e$) dipole ($q_{l=1} = d$) interaction with broadening $\bar{\sigma}_{01} \sim ed/a^2$, where $a$ is the lattice spacing. Furthermore, $\kappa_{l'l}$ is a constant of order one which accounts for the topology of the lattice. For a simple cubic lattice [139]: $\kappa_{01} = 2.35$, $\kappa_{02} = 0.87$, $\kappa_{11} = 2.36$. For an fcc lattice, these constants are practically the same as for the cubic lattice, e.g. the difference is smaller than 5% for $\kappa_{01}$. Screening is included via an effective dielectric constant $\epsilon_{l'}^{\mathrm{eff}} > 1$ that can be parameterized as a function of the polarizability of the surrounding neutral molecules ($\alpha$) by self-consistent simulations on a lattice [100]. Estimations based on the polarizability of the host (which mainly forms the environment for both host and emitter) yield $\epsilon_{0(1)}^{\mathrm{eff}} \sim 1.5(1.0) < \epsilon_r = 2.6$ for charge (exciton) transport [140]. Finally, $c$ accounts for a possible fractional filling of the lattice, where for very small fillings of the lattice, the distribution can deviate from a Gaussian [141].

Using the *ab initio* molecular parameters obtained from DFT with the B3LYP functional and the def2-TZVP basis from tab. 3.3 in combination with filling factors of $c_{\mathrm{g(h)}} = 0.1(0.9)$ for guest (host), and a lattice spacing of $a = 1\,\mathrm{nm}$ obtained from the density, the energetic disorder is

$$\bar{\sigma} \sim \left[\sum_{m=\mathrm{g,h}} \bar{\sigma}_{01}^2(c_m, q_1^m)\right]^{1/2} = 0.09\,\mathrm{eV}\,, \tag{3.2}$$

since the variances $\bar{\sigma}_{01}^2(c_m, q_1^m = d^m)$ for interactions with the charge and the dipoles of surrounding host ($m = \mathrm{h}$) and guest ($m = \mathrm{g}$) are uncorrelated. The disorder is mainly dominated by $\bar{\sigma}_{01}$ since the interaction between charge and dipole [141] leads to stronger broadening compared to the charge-quadrupole [139] or dipole-dipole [140, 142] interactions ($\bar{\sigma}_{01} > \bar{\sigma}_{02}$ and $\bar{\sigma}_{01} > \bar{\sigma}_{11}$). Note that, in the lattice model, the broadening is identical for the DOS of the host and the guest ($\bar{\sigma}_{\mathrm{h}} = \bar{\sigma}_{\mathrm{g}} = \bar{\sigma}$), since always $\Delta q_0 = e$ and both molecules are embedded in the same surrounding. In contrast to this, a different broadening for host and guest is likely for exciton transport, where eq. 3.1 can also be used but $\bar{\sigma}_{0l} = 0$ because the carrier is uncharged. Then, $\Delta q_1 = |\vec{d^*} - \vec{d}|$ is the first contribution to the DOS and contains the excited state dipole $\vec{d^*}$ which can be different for host and guest.

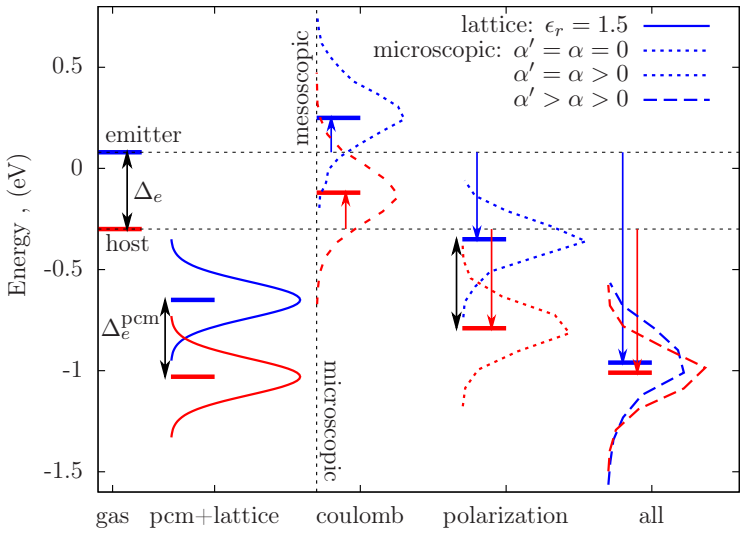


**Figure 3.5.** DOS for electrons localized on host (red) or emitter (blue) at an emitter concentration of $c = 0.1$. Shown are gas phase levels (gas) and their stabilization by PCM and broadening by a lattice model (pcm+lattice). For the microscopic model based on the realistic morphology of 4000 molecules at the same emitter concentration we compute the DOS without polarization (coulomb), with the same polarizabilities of the neutral and charged molecules (polarization), and including the polarizability change upon charging (all). Distributions are averaged over four snapshots.

The host and guest DOS, based on the PCM levels and broadening given by eq. 3.1, are shown in the left-hand side of fig. 3.5 (pcm+lattice) together with the gas-phase energies (gas). The DOS with broadening form the lattice and shift from the PCM constitute the best guess for the energy landscape of the host-guest system assuming that the details of the underlying morphology are not known which only allows for a mesoscopic description of electrostatic interactions including polarization.

### Polarizability change upon charging

We have so far recapitulated the results of various lattice models, estimated all static contributions to the DOS and have taken into account the polarizability of the environment using the PCM model for site-energy shifts and effective dielectric screening $\epsilon_{\mathrm{eff}}$ for the broadening. An important polarization contribution is, however, still missing, which is due to the interaction of electric fields created by the surrounding neutral molecules with the resulting induced dipole moment on the *charged* site. To account for this on a lattice level, we assume that the carrier site is a point-particle at $(0, 0, 0)$ with a polarizability tensor $\hat{\alpha}$ ($\hat{\alpha}'$) in a neutral (charged) state and is surrounded by randomly oriented static dipoles of strength $d$ pinned to the lattice sites. For *one* randomly oriented dipole at $(0, 0, a)$, the components of the electric field $\vec{f}$ at $(0, 0, 0)$ are uniformly distributed with zero means

and variances $\langle f_{x,y}^2 \rangle = \frac{d^2}{3a^6}$, $\langle f_z^2 \rangle = \frac{4d^2}{3a^6}$, which can easily be computed from the field

$$\vec{f} = 3\frac{(\vec{r}\cdot\vec{d})\vec{r}}{r^5} - \frac{\vec{d}}{r^3}\,, \tag{3.3}$$

that is created in the origin by a dipole $\vec{d}$ separated by a distance $\vec{r}$. Note that this field is created by a neutral molecule so that it will only weakly be screened ($\epsilon_{l=1}^{\text{eff}} \sim 1$ [140]), which is why we can safely neglect the polarizability of the surrounding sites in our derivation.

If we want to take into account that all surrounding lattice sites carry dipole moments, we have to sum up their contributions to find the distribution of the total electric field at the origin $\vec{F}$. Since summing over all dipoles is equivalent to a sum of *independent* uniform distributions, the central limit theorem implies that the three components $\gamma = x, y, z$ of the total field at the origin are all (approximately) Gaussian-distributed with vanishing mean $\langle F_\gamma \rangle = 0$ and variance

$$\langle F_\gamma^2 \rangle = \sigma_{F_\gamma}^2 \approx (4 + 1 + 16/81 + 1/16 + \dots)\frac{d^2}{a^6} \approx 5.3\frac{d^2}{a^6}\,, \tag{3.4}$$

where each term in the sum corresponds to a shell on a (cubic) lattice. In case of a neutral site, this field induces a dipole of strength $\vec{d}^{\text{ind}} = \vec{F}\hat{\alpha}$, so that the energy of the neutral site is $-\frac{1}{2}\vec{F}\hat{\alpha}\vec{F}$, where the factor $\frac{1}{2}$ takes into account the energy needed to distort the molecular charge distribution. When the site is charged, the energy becomes $-\frac{1}{2}\vec{F}\hat{\alpha}'\vec{F}$, which usually differs from the neutral case because the molecular polarizability in the charged state is stronger due to delocalization effects. Since the site energy is defined as the difference between charged and neutral states, the interaction of the total field created by randomly oriented molecules with the induced moment on the site leads to a contribution of $-\frac{1}{2}\Delta\alpha F^2$, with change in polarizability $\Delta\alpha = \frac{1}{3}\text{Tr}(\hat{\alpha}' - \hat{\alpha})$ since the orientations of $\hat{\alpha}$ and $\vec{F}$ are independent. If we neglect the correlations between the field components of the same dipole, then the squared components of the total field $F_{x,y,z}^2$ are three independent normal random variables, and their sum corresponds to a $\chi_3^2$ distributed variable $\xi$ with

$$\chi_3^2(\xi) = \sqrt{\xi}\exp\left[-\frac{\xi}{2}\right], \qquad \xi = \frac{F_x^2 + F_y^2 + F_z^2}{\sigma_{F_\gamma}^2} = \frac{F^2}{\sigma_{F_\gamma}^2}\,, \tag{3.5}$$

where the field is scaled by the variance introduced in eq. 3.4 making $\xi$ dimensionless. This variable has a mean of $\langle\xi\rangle = 3$ a variance of $\sigma_\xi^2 = \langle\xi^2\rangle - 3^2 = 6$, and an exponential tail at large $\xi$, which brings us to the main results of this subsection: the mean corresponds to a stabilization of the transport level by $\frac{3}{2}\Delta\alpha\sigma_{F_\gamma}^2$, the variance to its broadening by $\frac{\sqrt{6}}{2}\left|\Delta\alpha\right|\sigma_{F_\gamma}^2$, and the exponential tail results in low energy sites that can act as traps.

The $\chi_3^2$ distribution of a pure host system, with the *ab initio* parameters taken from tab. 3.3, is shown in fig. 3.6.a. It is compared to a numerically evaluated DOS on a cubic lattice filled with randomly oriented dipoles including all correlations. The agreement is good, justifying the derivation. At the same time, the results predict that the contribution

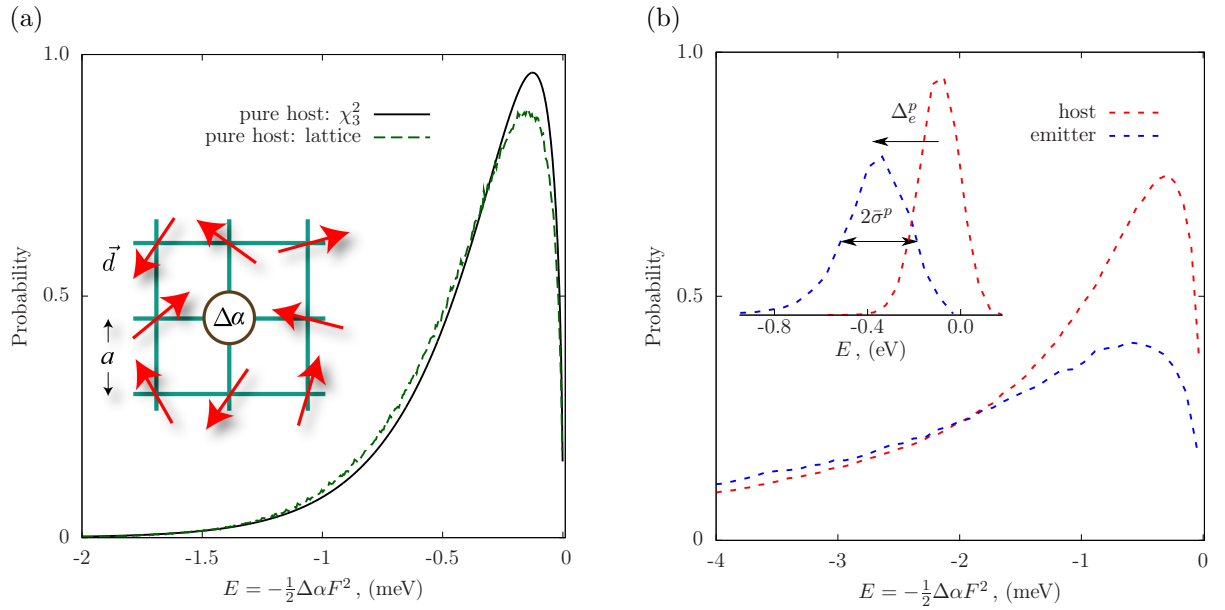


**Figure 3.6.** Histogram of the interaction energy between electric field $\vec{F}$ of randomly oriented static dipoles $\vec{d}$ with the induced dipole on a site with polarizability change $\Delta\alpha$ for a cubic lattice ($a = 1\,\mathrm{nm}$) as indicated in the left inset. (a) Pure host system: $\chi_3^2$ is an analytical result, while numerical simulations are performed using 3375 lattice sites averaged over 600 realizations. (b) Numerical estimation for the same interaction for the induced dipole on host or guest ($\Delta\alpha_\mathrm{h} < \Delta\alpha_\mathrm{g}$) in the mixture with $c_\mathrm{g} = 0.1$ evaluated on a lattice. While both main figures imply that the effect of $\Delta\alpha$ is of the order of meV, the inset in (b) shows that the same contribution is large when computed microscopically from the Thole model based on a realistic morphology of 4000 molecules ($c_\mathrm{g} = 0.1$) and charge distributions represented by atomistic partial charges.

to the DOS due to the polarizability change can be entirely neglected, since the absolute energy values involved are of the order of meV. This is also true for DOS of host and guest in the mixture as evaluated numerically in a lattice, where we have exchanged a fraction of $c_\mathrm{g} = 0.1$ host dipoles by the larger dipoles of the guest, with results presented in the main part of fig. 3.6.b.

### 3.3.2 Density of states from microscopic models

To verify the predictions of the mesoscopic models introduced above, we now calculate the DOS in the host-guest mixture using a realistic morphology at an atomistic resolution. In order to look at the effects of different electrostatic and polarization contributions to the DOS we turn certain interactions on and off in the microscopic model and always compare the resulting DOS to the mesoscopic result shown in fig. 3.5.

**Morphology of the mixture**

We prepare the morphology in the host-guest system using molecular dynamics simulations. The force field development for the host molecule has been described in sec. 2.2, and we perform similar steps to obtain the force field of the emitter. For the non-bonded interactions we use atomistic partial charges computed from DFT. Lennard-Jones parameters (see eq. 2.1) are taken from the OPLS force field with the exception of Ir, where we use parameters from a universal force field [143].

For bonded interactions, the unknown potentials are parametrized starting with the strongest improper dihedral $\phi$ which keeps the carbene and dibenzofuran units of one ligand in the same plane. Then, including this potential, the three angular potentials $\theta_{1,2,3}$ connecting the three ligands are scanned. After this, we add the softer dihedrals $\psi_{1,2,3}$ defining the orientation of the ligands with respect to each other. All seven potentials are parameterized using a quadratic form $V(\theta) = \frac{1}{2}k(\theta - \theta_0)^2$. Finally a Ryckaert-Bellemans potential $V(\beta) = \sum_{n=1}^{5}(\cos\beta)^n$ is used for the angle $\beta$ describing the rotation of the methyl group, where we use a multidimensional fit for the three H-atoms. The definitions of the potentials are shown together with the scans of the potential energy surfaces in fig. 3.7, while the force constants are summarized in tab. 3.4.

Amorphous morphologies of the host-guest system consisting of a total of $N = 4000$ molecules containing a small fraction of $0, 120, 240, 400, 520$ emitter molecules are obtained using the following protocol. First a random morphology is generated at low density using the PACKMOL package. Then, the system is equilibrated at 1000 K and the system becomes independent of the initial configuration, e.g. molecules have moved more than their diameter and the rotational correlation function has decayed. The equilibration is performed in the NPT ensemble (Berendsen pressure coupling with a time constant of $\tau_P = 2$ps) using stochastic dynamics (SD) with strong coupling, which allows to increase the density of the system while at the same time avoiding instabilities. In SD, a friction term (we have used strong coupling $\zeta^{-1} = 0.07$ps) and a fluctuating force $\vec{A}_i(t)$ (approximated by Gaussian white noise with zero mean for all times and a correlation function of $\langle A_{i\alpha}(t)A_{j\beta}(t+\Delta t)\rangle = 2m_i\zeta k_\mathrm{B}T\delta(\Delta t)\delta_{ij}\delta_{\alpha\beta}$ for two atoms $i$ and $j$ and components $\alpha, \beta = x, y, z$ are added to Newton's equations of motion resulting in a Langevin equation

$$m_i\frac{\mathrm{d}^2\vec{r}_i}{\mathrm{d}t^2} = \vec{F}_i - m_i\zeta\frac{\mathrm{d}\vec{r}_i}{\mathrm{d}t} + \vec{A}_i\,, \tag{3.6}$$

which is integrated using a time-step of 0.002 ps while constraining bonds. After annealing, the system is cooled down to 700 K during 4ns where it is equilibrated for another 1ns. Then it is quenched to 300 K using MD to integrate Newton's equations of motion, $m_i\frac{\mathrm{d}^2\vec{r}_i}{\mathrm{d}t^2} = \vec{F}_i$, as explained in sec. 2.2.3. All these steps were repeated for four different initial configurations yielding statistically independent final morphologies necessary to improve statistics of site energy distributions for small emitter concentrations. The length of the final cubic box is $L = 16$ nm for all emitter concentrations.

This protocol results in perfectly homogeneous morphologies, which might not correspond to the situation in the experiment, where emitter molecules with large dipole

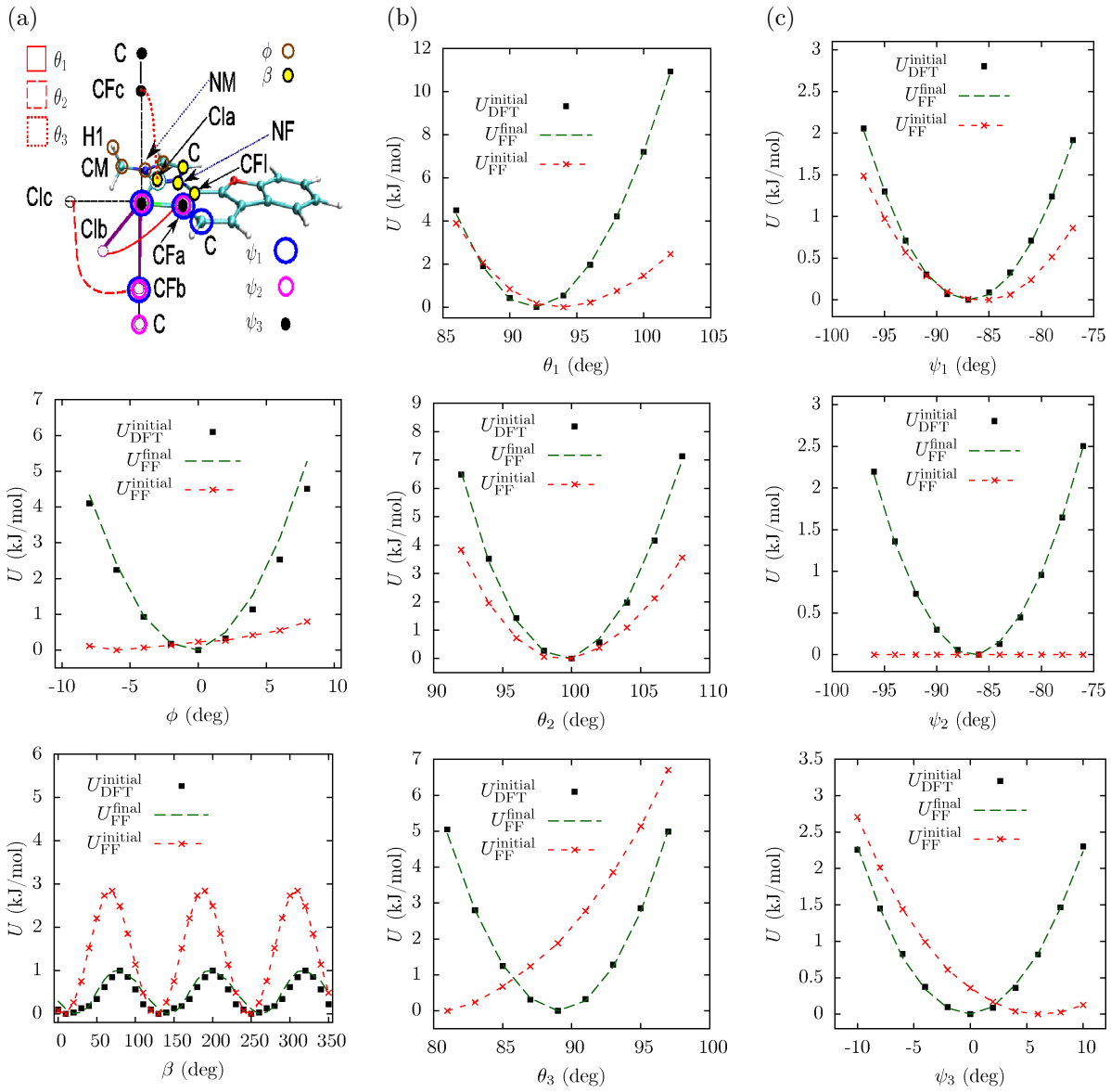


**Figure 3.7.** Force-field scans for the unknown degrees of freedom in the emitter. First-principles scans, $U_{\rm DFT}$, and final and initial force field scans, $U_{\rm FF}$, are shown. Column (a) Shows labeling with atoms CI(a,b,c) connected to the imidazole unit of ligands a,b,c and CF(a,b,c) connected to dibenzofuran unit. Below is the scan for the improper dihedral $\phi$ keeping the imidazole and dibenzofuran units of one ligand in the same plane. Below that is the scan for the rotational angle of the methyl group $\beta$. Column (b) shows scans for angles $\theta$ between the three ligands. Column (c) shows scans for rotations of the ligands with respect to each other defined by the proper dihedral $\psi$. Resulting force-field parameters are given in tab. 3.4.

| angle | atom labels | $\theta_0$ (deg) | $k$ (kJ mol$^{-1}$ rad$^{-2}$) |
|---|---|---|---|
| $\phi$ | NF-C-CIx-CFI, (x=a,b,c) | 0 | 420 |
| $\theta_1$ | CFa Ir CIb | 90 | 411 |
| $\theta_2$ | CFb Ir CIc | 96 | 321 |
| $\theta_3$ | CFc Ir CIa | 93 | 367 |
| $\psi_1$ | C CFa Ir CFb | -89 | 53 |
| $\psi_2$ | C CFb Ir CFa | -82 | 64 |
| $\psi_3$ | C CFc Ir CFa | -5 | 80 |

| angle | atom labels | $C_5$ (kJ mol$^{-1}$) |
|---|---|---|
| $\beta$ | C NM CM Hx, (x=1,2,3) | -1.12 |

**Table 3.4.** Force-field parameters for bonded interactions from PES scans of the emitter as shown in fig. 3.7. All potentials of the angles $\phi, \theta, \psi$ have a quadratical form, while for $\beta$ (rotating the methyl group) we use a periodic Ryckaert-Bellemans potential, where all coefficients $C_n \approx 0$ except for $n = 5$.

moments can aggregate and form an interconnected pathway. However, this is only relevant for studying hole transport which occurs via the minority component due to large $\Delta_h$. Here, we concentrate on electron transport, where the assumption of a homogeneous morphology is not critical. In the remaining part of this section we use a morphology with an emitter concentration of $c = 0.1$ which corresponds to 400 emitter molecules and 3600 host molecules.

### Site-energy distributions

The molecular charge distributions for charged and neutral states are approximated by fitting atomistic partial charges to reproduce the electrostatic potential of *ab initio* calculations (DFT) in the gas phase. Polarization effects in the bulk are treated self-consistently using the Thole model which we have parameterized on molecular polarizability tensors from DFT as explained in sec. 2.7.3. For the emitter, additional atomistic polarziabilities of $\alpha_{\mathrm{N,\,Ir}} = (1.6, 11.0)\text{Å}^3$ are used to reproduce the polarizability of $\alpha = 106.7\,\text{Å}^3$ in the neutral state. Atomistic polarizabilities are scaled by $f_{c(a)} = 1.93(9.02)$ for the cationic/anionic emitter which reproduces $\alpha' = \alpha_{c(a)} = 130.1(325.7)\,\text{Å}^3$. Therefore, the change in polarizability $\Delta\alpha$ for the anion (electron transport) is much larger for the emitter as compared to the host molecule as shown in tab. 3.3.

For computation of the DOS of host and guest in the mixture, we first consider bare Coulomb interactions in the nearest image convention using $\epsilon_r = 1$ in eq. 2.24, and thereby neglect polarization completely. The corresponding DOS, shown in fig. 3.5 (coulomb), is shifted with respect to the gas-phase values, both for host and guest. This shift is

not predicted by lattice models which can be explained by a break-down of the multipole expansion at small intermolecular separations (intercalating charge distributions) and local correlations in molecular orientations. Since both host and guest are equally shifted, there is no effect on charge transport. The broadening of the levels is artificially strong because the screening is not taken into account.

We now partially include molecular polarizability by assigning the polarizabilities of the neutral state of host and guest also to their charged states. The resulting DOS is shown in fig. 3.5 (polarization). The screening of the charge reduces the broadening and the static shift and also leads to a strong stabilization similar to the PCM. Apart from an irrelevant global shift, this DOS agrees quite well with the broadening and energy barrier $\Delta_e$ predicted by the mesoscopic approach (pcm+lattice). This can be explained by the fact that the main contribution to the DOS (the charge-dipole interaction), is well captured by the lattice model, while contributions due to the change in polarizability are small in the lattice model and are neglected at this stage of the microscopic description ($\alpha' = \alpha$).

Finally, we account for the polarizability change upon charging by increasing the atomic polarizabilities in the anionic state of emitter and host to take into account the higher polarizability in the charged state. We first evaluate only the interaction of the field from the surrounding molecules with the resulting induced dipole on the carrier site, since this contribution can be directly compared to the lattice model results presented in the main part of fig. 3.6.b. For better comparison, we impose some of the assumptions of the lattice model, i.e. while charge distributions on surrounding molecules are taken into account, their polarizabilities are neglected. The central molecule has no charge distribution but its change in polarizability tensor is accounted for. The results are shown in the inset of fig. 3.6.b for both host and guest. One can see that the larger polarizability difference of the guest as compared to the host ($\Delta\alpha_\mathrm{g} > \Delta\alpha_\mathrm{h}$, see tab. 3.3) leads to a reduction of the energy difference between guest and host levels, $\Delta_e$, by $\Delta_e^p$. There is also an additional broadening of the DOS, $\bar{\sigma}^p$, with a tail of low-lying states (especially for the guest). All three effects are in an excellent *qualitative* agreement with the lattice model, i.e., $\Delta_e^p = \frac{3}{2}\left(\Delta\alpha_\mathrm{g} - \Delta\alpha_\mathrm{h}\right)\sigma_{F_\gamma}^2$, and additional broadening is stronger for the guest than for the host since $\bar{\sigma}^p_{\mathrm{h(g)}} = \frac{\sqrt{6}}{2}\left|\Delta\alpha_{\mathrm{h(g)}}\right|\sigma_{F_\gamma}^2$. The *quantitative* difference is, however, striking: in the microscopic model, the guest has a gas-phase level shift and broadening, $\langle E_\mathrm{g}^p\rangle = -0.37\,\mathrm{eV}$, $\bar{\sigma}_\mathrm{g}^p = 0.15\,\mathrm{eV}$ which are an order of magnitude larger than predicted by the mesoscopic model.

This discrepancy can be attributed to two factors. First, we have used a perfect lattice in the mesoscopic model, while including positional disorder might be necessary to better describe the amorphous phase. In order to do this, one could choose the positions of the dipoles to slightly deviate from the lattice points $\vec{r}_i$ by introducing Gaussian distributed random displacements $\vec{u}_i$ with zero mean and width $\sigma_a$. Then, the new positions of the dipoles are constructed from $\vec{r}_i^{\,\mathrm{new}} = \vec{r}_i + \vec{u}_i$. In this model, the broadening of the DOS due to electrostatic interactions increases with $\sigma_a$ and the total rank of the interaction $(l' + l)$. For example, the energetic disorder of the charge-dipole interaction (which scale as $1/a^2$) increases for small $\sigma_a$ to $\bar{\sigma}_{01}^{\mathrm{new}} = \bar{\sigma}_{01}\{1 + 0.17[(\sigma_a/a)(l' + l + 2)]^2\}^{1/2}$. Since $l + l' = 1$, and

typically $\sigma_a/a < 0.3$ in amorphous phases of small molecules [136], the effect of positional disorder on the static contributions to the DOS can be neglected.

In contrast to this, the contribution to the DOS due to the change in polarizability on the carrier site scales as $1/a^6$, as shown in eq. 3.4, and positional disorder plays a more important role. Since the positional disorder $\sigma_a$ is an intrinsic property of the real morphology, it cannot be quantitatively predicted by lattice models and fitting to microscopic simulations (or experimental data) are unavoidable to predict the energy landscape.

The second reason for the discrepancy between mesoscopic and microscopic approach lies in the fact that only the lowest moment (a second rank tensor) is used to account for molecular polarizability in the lattice, while the description of an inhomogeneous distribution of the induced electrostatic potential requires higher order tensors [144]. In other words it is unlikely that mesoscopic descriptions are capable of correctly predicting the energy landscape in amorphous organic semiconductors, at least at this level of description of molecular polarizability.

We finally would like to point out that, in case of hole transport, the shift between host and guest is reversed since for the cations $\Delta\alpha_{\mathrm{h}} = 63.7\,\text{Å}^3 < \Delta\alpha_{\mathrm{g}} = 23.4\,\text{Å}^3$, which results in an increase of the barrier $\Delta_h$.

### 3.3.3 Consequences on charge transport in mixtures

In the last section of this chapter we discuss the implications of the altered DOS on the OLED functionality. Before we concentrate on the site energies, where the change in polarizability plays the most important role, we shortly discuss the other parameters (transfer integrals and reorganization energies) entering the charge transfer rate.

#### Transfer integrals

In the mixture we have to distinguish between rates from host to host, from emitter to emitter and between host and emitter. We have computed transfer integrals from DFT (PBE functional and TZVP basis) taking into account frontier orbitals of the whole molecules (see sec. 3.2.2). The resulting distributions of transfer integrals for 4000 molecular pairs at an emitter concentration of $c = 0.1$ are presented (for electrons) in fig. 3.8.a. They show that in the amorphous phase, transfer integrals are similar between all types of molecules although intermolecular distances can differ as illustrated by the pair radial distribution function shown in the inset.

#### Reorganization energy

Intramolecular reorganization energies $\lambda_{ij}$ for a pair of molecules $i$ and $j$ can be computed from potential energy surfaces of charged and neutral molecules as explained in sec. 2.6. In case of the host and guest considered here, we have for electron transport between two host molecules $\lambda_e^{\mathrm{hh}} = 0.19\,\text{eV}$, while between guests $\lambda_e^{\mathrm{gg}} = 0.10\,\text{eV}$. For transport from host to guest $\lambda_e^{\mathrm{hg}} = 0.16\,\text{eV}$ and $\lambda_e^{\mathrm{gh}} = 0.14\,\text{eV}$ in the reverse direction since charging and

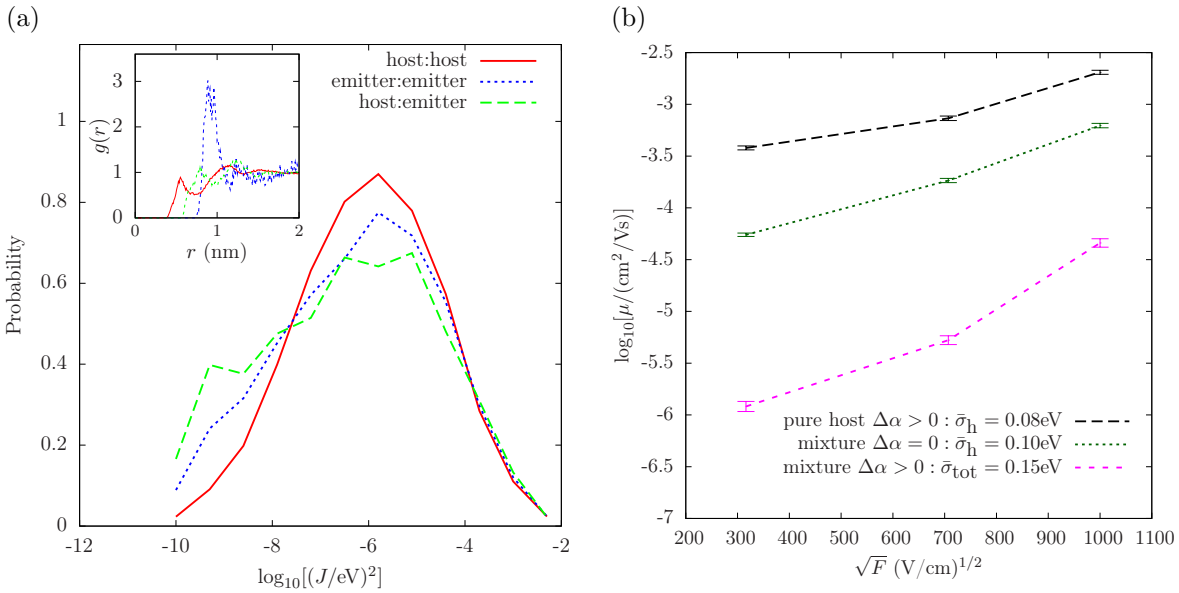


**Figure 3.8.** (a) Transfer integrals for electron transport in the mixture with emitter concentration $c = 0.1$ obtained for 4000 molecules. Inset shows radial distribution functions for centers of mass. (b) Electron mobilities in a pure host system and in the mixture using the DOS from the microscopic models excluding ($\Delta\alpha = 0$) or including ($\Delta\alpha > 0$) change in polarizability $\Delta\alpha$. As the energetic disorder $\bar{\sigma}$ grows, mobilities are reduced and the Poole-Frenkel slope is increased. We show the disorder for the DOS of the host ($\bar{\sigma}_\mathrm{h}$) if electrons are transported only by the host, while the width of the combined (emitter+ host) DOS is used for $\Delta\alpha > 0$ as both contribute to charge transport.

discharging energies are different for the two compounds. These values suggest that the reorganization energy slightly favors transport of electrons between the emitter molecules. For hole transport all reorganization energies are around $\lambda_h \approx 0.27$eV.

### Energy landscape and mobility

The final DOS obtained from the the microscopic model in the host-guest system, shown in fig. 3.5 (all), is substantially different from the one predicted by combining the PCM with a lattice model (pcm+lattice). One would expect, that the increased DOS width for electrons and the exponential tail of low lying energies (acting as traps) due to $\Delta\alpha > 0$ in the microscopic model will result in much lower electron mobility compared to the DOS predicted by lattice model or by neglecting the change in polarizability in the microscopic model by setting $\Delta\alpha = 0$ (polarization). In order to quantify the effect of $\Delta\alpha$ on mobility we have performed KMC simulations of one electron in the host-guest system using the realistic morphology obtained from MD. First, we use the DOS obtained with $\Delta\alpha = 0$ and then include the change in polarizability by using the DOS with $\Delta\alpha > 0$. Mobilities, shown in in fig. 3.8.b, are compared to values in the pure host material. As expected,

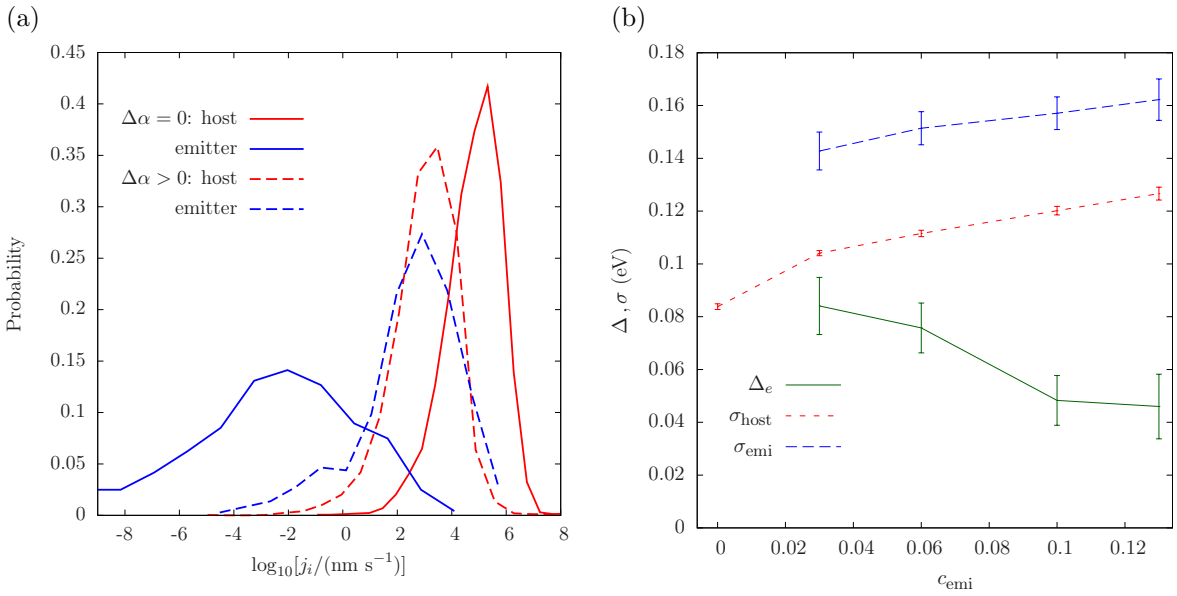


**Figure 3.9.** (a) Histogram of electron currents for 4000 molecules at an emitter concentration of $c = 0.1$ show that in case of $\Delta\alpha = 0$ electrons are transported mainly by the host, but if $\Delta\alpha > 0$ is considered, emitter molecules contribute almost equally to charge transport. (b) DOS broadening for host and emitter and the transport barrier $\Delta_e$ between them as a function of the emitter concentration evaluated with $\Delta\alpha > 0$ and averaged over four MD snapshots. For $\Delta\alpha = 0$ the barrier is much larger $\Delta_e \approx 0.4\,\text{eV}$.

the mobility decreases by two orders of magnitude and a steeper Poole-Frenkel slope can be observed if $\Delta\alpha > 0$. Both effects can be explained by stronger energetic disorder (see eq. 2.31).

### Electron current on host and emitter

Now we address the question of which molecules are participating in electron transport. In the mesoscopic lattice model one would expect, that electrons are transported only by the host because of the energy barrier $\Delta_e \approx 0.4\,\text{eV} \gg k_\text{B}T$, that originates from a large energy difference of the EA of host and guest (see tab. 3.2). Note that the site energies are spatially correlated (see sec. 2.7.5), so that the small overlap of the DOS of host and guest will not lead to charge-transfer of electrons from the host to the guest. Also the microscopic model where the change in polarizability is neglected ($\Delta\alpha = 0$) predicts that electrons are transported only by the host.

In contrast to this, the DOS of host and guest strongly overlap if the change in polarizability is accounted for in the microscopic model, as shown in fig. 3.5. In order to analyze whether this overlap leads to the participation of the host molecules to electron transport, we evaluate a local electron current $\vec{j}_i$ through molecules $i$, as introduced in eq. 2.44. The distributions of this current on host and guest molecules is presented in fig. 3.9.a. where

we have used the DOS from the microscopic model with $\Delta\alpha = 0$ (equivalent to the lattice model) and $\Delta\alpha > 0$. As expected, the electron current through the emitter is negligible in case of $\Delta\alpha = 0$, but both host and guest contribute equally to the current if the change in polarizability is included.

**Dependence of the DOS on emitter concentration**

Finally we also investigate the broadening of the DOS and the barrier for electron transport between host and guest, $\Delta_e$, (including internal energies from EA and electrostatic interactions with $\Delta\alpha > 0$) as a function of the emitter concentration. As expected from eq. 3.2, the energetic disorder $\bar{\sigma}$ for host and guest increases for stronger concentrations of the emitter which is due to its large dipole moment (see tab. 3.3). Additionally the energy barrier (for which $\Delta_e \approx 0.4$ in case of $\Delta\alpha = 0$) decreases since the average static dipole moment increases (as expected from eq. 3.4).

### 3.3.4 Summary of polarization effects

To summarize, we have shown that a polarization-induced stabilization of a molecule in its charged and neutral state can lead to shifts, broadening, and traps in the distribution of site energies in an amorphous phase. This effect cannot correctly be described in mesoscopic models, and is especially important in multi-component systems, where the change in polarizability is different for the components, e.g for the emission layer of OLEDs or for donor-acceptor mixtures used in OPVC. Note that similar results are expected to occur for the energy landscape of exciton transport due to a change in polarizability between the ground states and excited states of a molecule. Thus, the polarizability change upon charging or excitation should be added to the set of molecular parameters essential for understanding charge and energy transport in organic semiconductors.

# Chapter 4

# Charge transport in self-assembled systems

Materials for organic electronics can be classified in two major categories, related to their processing conditions. On the one hand, small molecules with low molecular weight can be grown in single crystals or can be vapor-deposited from the gas phase which allows a very controlled but rather slow thin film growth and facilitates the fabrication of complicated layered structures. These are needed for example in high-quality organic light emitting diodes (OLED) that are nowadays used in displays or television screens. On the other hand, materials with larger molecular weight, such as polymers or aromatic molecules with long side-chains, can be processed from solution. Typical techniques include spin-coating on suitable substrates followed by evaporation of the solvent, or inkjet-like printing methods. The scalability of these techniques eventually allows for cheap mass-production of organic solar cells or radio frequency identification tags consisting of organic field effect transistors (OFET).

One of the main disadvantages of organic materials compared to traditional semiconductors lies in their low charge carrier mobility which has a negative impact on efficiencies of solar cells and limits switching frequencies of OFETs. In this respect, additional self-assembling abilities of organic materials can be of great advantage to increase the mobility.

Discotic liquid crystals represent a subset of soluble, self-organizing compounds displaying columnar molecular arrangement. While side chains attached to an aromatic core make these materials soluble, the overlap of the $\pi$-orbitals of the cores from neighboring molecules allows for efficient charge-transport along these columns. In these molecular wires, local charge-carrier mobilities up to $1\,\mathrm{cm^2V^{-1}s^{-1}}$ can be achieved by systematically varying the substituents and the processing conditions [145].

Perylenediimide (PDI) derivatives form a particularly interesting class of discotics, since compounds based on these derivatives are some of the best and most frequently used n-type semiconductors [146, 147], even though their electron and hole mobilities are rather similar [148]. Mobilities up to $0.6\,\mathrm{cm^2V^{-1}s^{-1}}$ have been reported for thin PDI films [149] and they have already been applied in different areas of organic electronics, such as all-organic solar cells and OFETs [150, 151]. They can self-assemble in structures with different pack-

ing motives, which result in different charge-carrier mobilities [152]. The self-organization can be controlled by introducing hydrogen bonding [153], metal-ion coordination, [154] or by changing the geometry of the side groups [155].

Since high charge-carrier mobility is essential for the majority of applications, for example high switching frequencies in organic thin film transistors used in back-planes of displays, significant efforts have been directed at its improvement, for example by varying the chemical structure [156]. It has been concluded, however, that optimizing the electronic structure alone is not sufficient, since the material morphology, which heavily depends on both chemical structure and processing, can alter charge mobility by orders of magnitude [157]. This suggests that the following steps are required for compound design: synthesis of a new compound, optimization of processing conditions, morphology characterization, and finally measurements of the mobility. By iterating this procedure for a set of compounds, one might be able to formulate empirical rules, or structure-processing-property relationships. In practice, however, finding such relationships has been so far very difficult. It is often not obvious whether the improvement comes from a better electronic structure or a superior morphology, since both are affected by changes in the chemical structure.

A particularly difficult problem is to characterize partially disordered material morphologies with a high level of detail. Routinely employed experimental techniques are wide-angle X-ray scattering (WAXS) and solid-state nuclear magnetic resonance (NMR) [158, 159]. Both methods provide *averages* over the molecular ensemble and, as such, do not contain full information about the *distributions* of molecular positions and orientations. At the same time, charge dynamics of partially ordered semiconductors is sensitive to the molecular arrangement on all length scales. Indeed, transfer integrals and charge hopping rates strongly depend on the chemical composition and *local* molecular ordering, while the global charge-carrier pathway is determined by the *large scale* morphology and presence of defects, which are limiting charge transport in one-dimensional systems.

In this situation, modeling becomes a necessity: it assists in identifying correct molecular packing motives [145, 160, 161], quantifies the degree of local disorder, and links both of these to the charge carrier mobility.

In this chapter, we investigate the role of the side chains in supra-molecular (in this case helical) packing motives of discotics and study effects of these packing motives on charge transport. In particular, we compare supra-molecular arrangement of two PDI derivatives, with alkyl ($C_{8,7}$–PDI) and tri-ethylene-glycol (TEG–PDI) side chains as shown in fig. 4.1.a,b. To do this, we first analyze the experimental results from solid-state NMR and WAXS and correlate the deduced molecular arrangement with the results of molecular dynamics (MD) simulations. Analyzing the MD snapshots we relate packing of side chains to the supra-molecular helical arrangement of molecules in a column. Finally, we calculate electronic couplings between conjugated cores of neighboring molecules and use the high-temperature non-adiabatic limit of Marcus theory (eq. 2.6) to calculate the charge hopping rates between them. Charge carrier mobility for electrons and holes is then obtained by solving a linearized master equation for occupation probabilities (eq. 2.33). Simulation results are compared to pulse-radiolysis time-resolved microwave conductivity (PR-TRMC)

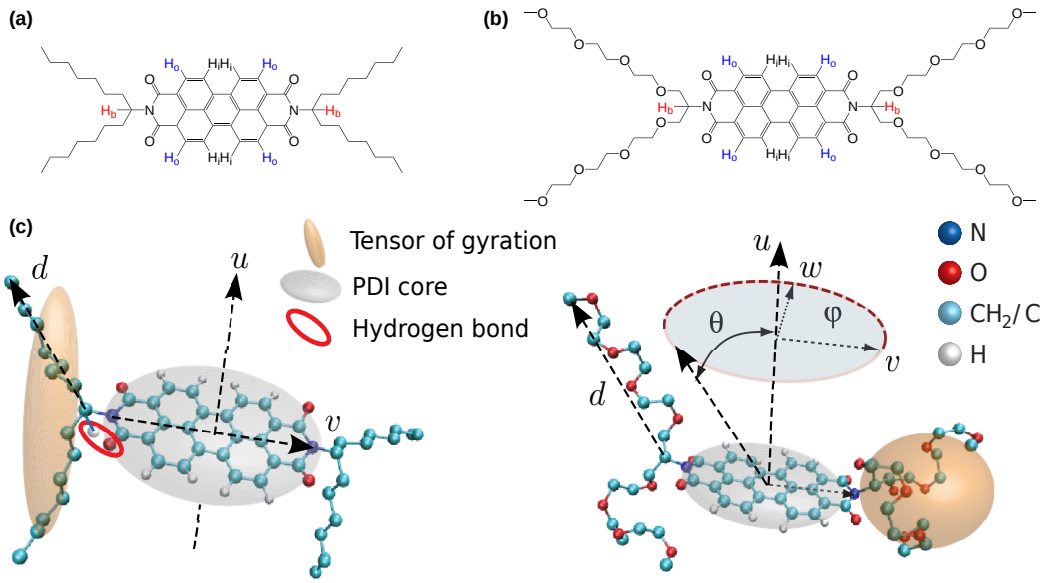


**Figure 4.1.** Chemical structure of (a) $C_{8,7}$–PDI with the alkyl side chain and (b) TEG–PDI with the tri-ethylene-glycol (TEG) side chain. (c) Sketch of the two PDI derivatives: side chains are displayed using united atom representation except for the branching C-atom. The orientation of the conjugated core defines the coordinate systems given by vectors $\boldsymbol{v}$ (connects the two N-atoms in the molecular plane), $\boldsymbol{u}$ (normal to the molecular plane), and $\boldsymbol{w} = \boldsymbol{u} \times \boldsymbol{v}$. Angles $\theta$ and $\phi$ are polar and azimuthal angles of the end-to-end vector $\boldsymbol{d}$ in this coordinate system. Ellipsoids depict tensors of gyration for each pair of side chains. Labels for different H atoms (left) are used for dynamical order parameters in Table 4.1.

mobility measurements and finally, structure-mobility relationships are formulated.

## 4.1 Molecular ordering from experiment

A combination of WAXS and advanced solid-state NMR experiments probing the local molecular conformations averaged over the whole sample have been used to analyze the self-assembled packing motives for the two PDI derivatives. Due to the strong $\pi$-$\pi$ interaction of the PDI cores, the molecules pack in columns with normal vectors $\vec{u}$ of the cores parallel to the column. Interactions of the side chains lead to a helical pitch angle $\alpha$ between the long axes $\vec{v}$ of consecutive elongated cores in the column (see fig. 4.1.c for definitions of the vectors). Experimental results indicate that $C_{8,7}$–PDI molecules are stacked with a small pitch angle of about $20 - 45°$ [159, 162]. This information was derived from the observation of a strong inter-molecular contact between the branching protons of the attached side chains for successive $C_{8,7}$–PDI molecules and the distance between these protons. Moreover, solid state NMR results suggest that this proton is hydrogen bonded and thereby coordinated to the carbonyles on either side of the PDI core, as indicated in fig. 4.1.c. Such an intra-molecular hydrogen bond is quite unusual since it involves a

CH group and a carbonyle. It is, however, expected to be important with respect to how the attached side chains pack and organize between the columns [163, 164]. Finally, the $C_{8,7}$–PDI core was observed to be rather rigid as identified from a site-specific dynamical order parameter $S \approx 1$ (see eq. 4.1) indicating that the columnar packing of $C_{8,7}$–PDI is rather stable [162].

Replacing the alkyl side chains with TEG at the branching point has a dramatic effect on both the thermotropic behavior and the columnar packing of the PDI molecules. Transition temperatures at 326 K and 403 K can be identified in TEG–PDI, corresponding to the phase transitions from crystalline (Cr) to liquid crystalline (LC) and from LC to the isotropic phase, respectively. In the LC phase TEG–PDI molecules are packed with a pitch angle of 90° [165].

When cooling TEG–PDI from the LC phase to the Cr phase the main packing motif remains helical with a pitch angle of 90° [165], but two other motives at smaller angles also emerge, resulting in a broad distribution of pitch angles centered around 90° for TEG–PDI. This immediately raises two questions. How can such a complex packing be understood? And what is the role of the attached TEG side chains? To answer these questions a deeper understanding of the morphology of the TEG–PDI system in its crystalline state is required, which can be provided by performing MD simulations at room temperature.

Before going into detail about the different morphologies and packing motives we compare dynamical order parameters for $C_{8,7}$–PDI and TEG–PDI obtained experimentally from solid-state NMR [159, 165] with those based on MD simulations. The dynamical order parameter $S$ is related to the flexibility of a moiety of interest. From the MD-trajectory it can be computed as

$$S = \left\langle \frac{1}{N} \sum_{i=1}^{N} \left( \frac{3}{2} \left( \vec{M}_i \cdot \vec{m}_i \right)^2 - \frac{1}{2} \right) \right\rangle , \qquad \vec{M}_i = \langle \vec{m}_i \rangle , \tag{4.1}$$

where $< \cdots >$ denotes time average, $N$ is the number of molecules in the system and $\vec{m}_i$ is the vector along the $C - H_x$ group of interest with $H_x = (H_i, H_o, H_b)$ as shown in fig. 4.1.a.

Calculated dynamical order parameters are summarized together with the NMR results in tab. 4.1. For $C_{8,7}$–PDI a value of $S = 0.91$ (T = 300 K) is calculated for the innermost core protons of the PDI core. This is in good agreement with the dynamical order parameter of $S \approx 0.9$ determined from solid-state NMR experiments [159] and shows that the columnar system based on $C_{8,7}$–PDI is quite stable, even on the short time scales of the MD simulations, which are of the order of nanoseconds.

Experimentally determined order parameters of TEG–PDI are on the order of $S \approx 0.5$ in both the LC and Cr phase (see tab. 4.1). The reduction by about a factor of 2 from a completely rigid case can be explained by the presence of cooperative motion and local fluctuations of the columnar-packed molecules in the LC and Cr phases, respectively. From the MD trajectory of TEG–PDI, values in the range of $S \approx 0.8 - 0.9$ are obtained for the PDI core part of TEG–PDI (see tab. 4.1). The discrepancy from the experimental values detected during the solid-state NMR experiments (milliseconds) mainly reflect that the different kinds of motion occurring in the two thermodynamic phases of TEG–PDI are

**Table 4.1.** Dynamic order parameters $S$ for the different core C-H moieties determined from MD simulations (see Eq. 4.1) and 2D rotor-encoded solid-state NMR and the corresponding orientational order parameter $Q$ from MD (see Eq. 4.2). Experimental uncertainties are ±0.1. Results of previous work, which was not performed in the course of this thesis are indicated in brackets.

| Method | PDI | $T$, K | $S(\mathrm{CH_o})$ | $S(\mathrm{CH_i})$ | $S(\mathrm{CH_b})$ | $Q$ |
|---|---|---|---|---|---|---|
| NMR [159] | $C_{8,7}$–PDI | 300 | 0.9 | ∼1 | 0.9 | |
| NMR [165] | TEG–PDI | 303 | 0.46 | 0.43 | 0.48 | |
| NMR [165] | TEG–PDI | 373 | 0.48 | 0.48 | 0.52 | |
| MD [162] | $C_{8,7}$–PDI | 300 | 0.91 | 0.86 | 0.96 | 0.90 |
| MD | TEG–PDI | 300 | 0.93 | 0.88 | 0.98 | 0.95 |
| MD | TEG–PDI | 400 | 0.89 | 0.84 | 0.96 | 0.94 |

on time scales longer than what is sampled in the MD simulations (nanoseconds). Thus, the MD simulations performed for TEG–PDI should be considered as a *static snapshot* of the morphology. This snapshot, however, can still be used to determine the charge carrier mobility of the TEG–PDI-system, since charge transfer occurs on a much faster time scale (picoseconds) in the molecular wire due to strong electronic coupling and low energetic disorder.

In addition to the dynamical order parameter we have computed an orientational order parameter $Q$ as the largest eigenvalue of the tensor

$$Q_{\alpha\beta} = \left\langle \frac{1}{N} \sum_{i=1}^{N} \left( \frac{3}{2} u_\alpha^{(i)} u_\beta^{(i)} - \frac{1}{2} \delta_{\alpha\beta} \right) \right\rangle . \tag{4.2}$$

where $\alpha, \beta = x, y, z$. Here, $Q = 1$ implies perfect alignment of the unit vectors $\vec{u}$ (see fig. 4.1.c) and $Q = 0$ corresponds to an isotropic angular distribution. Both derivatives show strong nematic order as can be seen in tab. 4.1.

## 4.2 Molecular ordering from simulations

Apart from analyzing rigidity and nematic ordering, MD simulations can also be used to link the side-chain packing to the molecular arrangement within columns. All systems under consideration consisted of 960 PDI molecules stacked in 16 columns of 60 molecules each. Force-field parameters and simulation details can be found in the Supporting Information of ref. [145, 162].

Initial configurations were prepared using an orthorhombic unit cell with $a = 22\,\text{Å}$, $b = 17\,\text{Å}$, and $c = 3.5\,\text{Å}$ for $C_{8,7}$–PDI and a hexagonal lattice with $a = b = 23\,\text{Å}$, $c = 3.4\,\text{Å}$ for TEG–PDI [162, 165]. Systems were equilibrated at 300 K for 40 ns using the GROMACS package [166]. Different initial pitch angles were used which all converge to an average pitch angle of 40° in $C_{8,7}$–PDI, and 90° for TEG–PDI respectively.

We have used these MD simulations as a starting point for our investigation of the molecular packing motives. First, histograms of the pitch angle $\alpha$ between neighboring

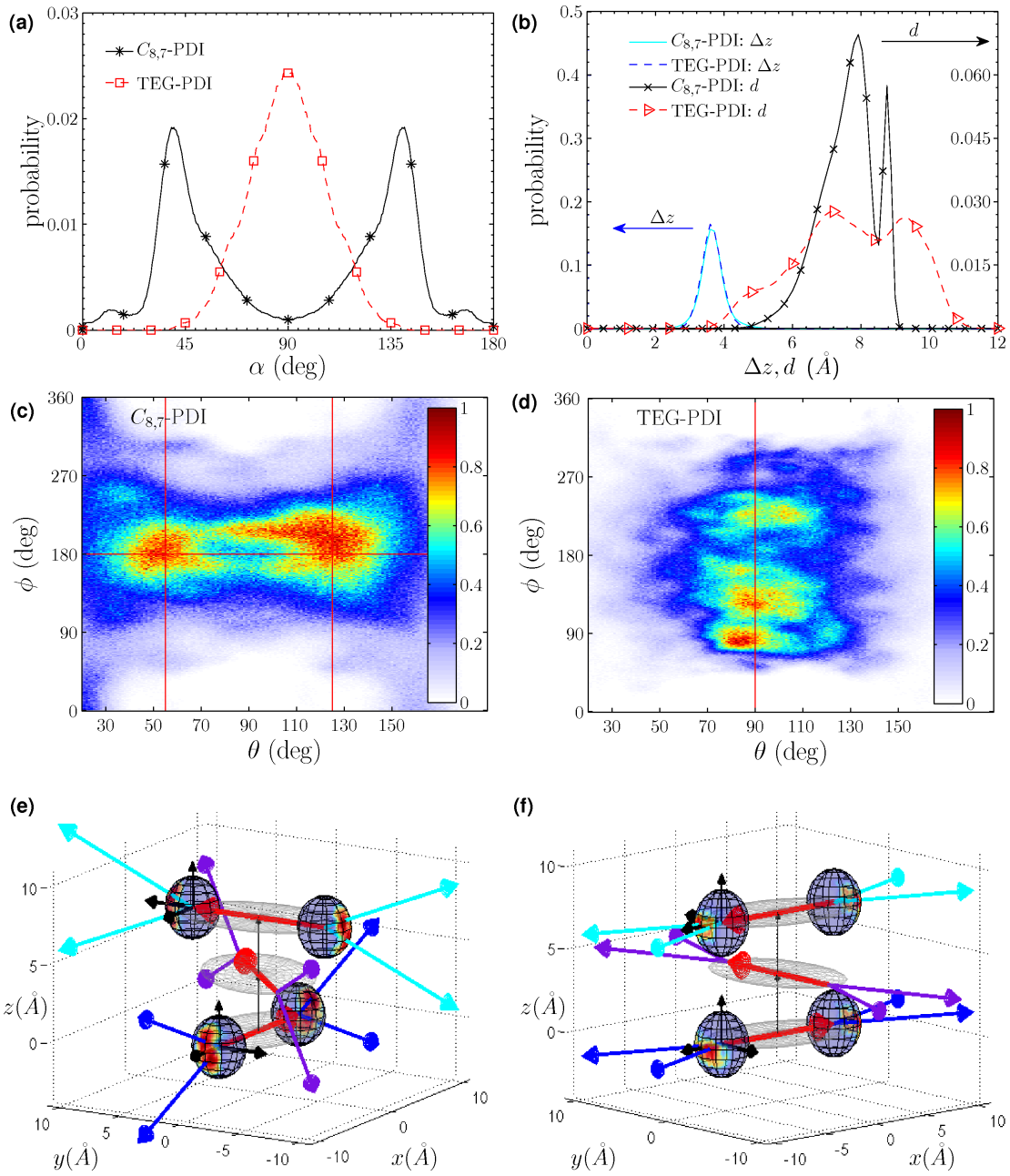


**Figure 4.2.** Molecular packing motives (see fig. 4.1 for definitions). Histograms of (a) the helical pitch angle $\alpha$ and (b) of the intermolecular distance $\Delta z$ and length $d$ of the four side chains. The narrower distribution of $d$ for $C_{8,7}$–PDI, which has less atoms shows that alkyl side chains are more rigidly stretched out and TEG side chains are more flexible. (c),(d) Orientation of the end-to-end distance $d$ for alkyl and TEG side chains with respect to the core. The hydrogen bond near the branching C-atom defines the direction of the stiff alkyl side chain to point out of the molecular plane $\theta \approx 55°$ (red vertical line) while the more flexible TEG side chains can average out the direction given by the hydrogen bond and rest in the molecular plane $\theta \approx 90°$. (e) For three $C_{8,7}$–PDI molecules in a column, side chains (blue arrows) are sticking out of the molecular plane (grey disc) leading to a pitch angle of 40° (red arrows display the vector $\vec{v}$ connecting N atoms in the core). Distributions of angles $\theta, \phi$ for orientation of side chains from (c) are indicated on unit spheres centered at the two N atoms (red indicates highest probability). (f) For TEG–PDI, side chains rest in the molecular plane leading to larger pitch angles of 90°.

molecules are shown in fig. 4.2.a. A narrow distribution with a maximum around 40° is found for $C_{8,7}$–PDI while for TEG–PDI the distribution is much broader and is centered around 90°. This agrees with the NMR results of $20° - 45°$ for $C_{8,7}$–PDI and 90° for TEG–PDI as was mentioned in the last section. Furthermore, the broad pitch angle distribution for TEG–PDI shows indications of the same packing motives as revealed by solid-state NMR in the Cr phase, where the width of the distribution was estimated to be as large as $\sigma_\alpha \approx 40°$ [165], which is in excellent agreement with simulation results. Intermolecular distances have a narrow distribution for both compounds with a maximum around $\Delta z = 3.6\,\text{Å}$, as shown in fig. 4.2.b.

To understand the difference in molecular packing of the two PDI derivatives we analyzed conformations of their side chains. This was done with the help of the end-to-end vector $\vec{d}$ connecting the branching C-atom and the end of the side chain, as illustrated in fig. 4.1.c. The distributions of the length of this vector, $d$, are shown in fig. 4.2.b. The narrower distribution for alkyl side chains suggests that they are more rigid and stretched out as compared to the TEG side chains. This is confirmed by a similar mean value $\bar{d} = 7.6\,\text{Å}$ for $C_{8,7}$–PDI and 7.7 Å for TEG–PDI when keeping in mind that the alkyl side chain has less atoms than the TEG side chain. The eigenvalues of the tensors of gyration of the two combined branches of side chains, shown in fig. 4.1.c, indicate that side chains are more stretched out in $C_{8,7}$–PDI (having a ratio of eigenvalues of 43:6:1) as compared to a more flexible glycol chain in TEG–PDI (17:3:1). The orientation of the vector $\vec{d}$ is characterized using two-dimensional histograms of spherical coordinates $\phi, \theta$ (see fig. 4.1.c) shown in fig. 4.2.c,d. In case of $C_{8,7}$–PDI, the distribution is centered around $\theta = 55°$ and $180° - 55° = 125°$ indicating that, on average, the alkyl chains stick out of the molecular plane of the core by ±35°. In contrast, the distribution for TEG side chains is centered around $\theta = 90°$ indicating that the TEG chain reside in the molecular plane,

The observed conformational differences can be linked to the chemical structure as explained below. Simulation results in accordance to the NMR data [159] suggest that a hydrogen bond is formed between the H-atom attached to the branching C-atom of the side chain and the O-atom of the core (indicated in red in fig. 4.1.c). Due to the tetrahedral structure around the branching $sp^3$-hybridized C-atom in both derivatives, the first C-atoms after the branching C-atom in the upper and lower side chains will stick out of the molecular plane defined by the core. The direction given by the bond between the branching and first C-atom is maintained for the following bonds in the alkyl chain because of its rigid nature induced by the excluded volume of the H-atoms.

The TEG chains, on the other hand, contain less H-atoms and are more flexible. As a result, the direction imposed by the first C-atoms can be averaged out by the following bonds in the side chain that therefore can reside in the molecular plane.

Summarizing the MD results, one can conclude that the pitch angle of $\alpha = 90°$ for TEG–PDI is a consequence of a steric repulsion of the bulky spherical TEG side chains belonging to molecules that are *direct* neighbors. For $C_{8,7}$–PDI the more rigid alkyl side chains stick out of the molecular plane because of the hydrogen bond formation. Due to their larger extension, steric repulsion exists, not only between the side chains of direct

neighbors but also the *next-to-nearest* neighbors. Therefore the pitch angle is reduced to $\alpha = 40°$, which ensures the best side chain packing. The packing is illustrated for three consecutive PDI cores in fig. 4.2.f,g for $C_{8,7}$–PDI and TEG–PDI respectively. The pitch angle $\alpha$ is represented by red arrows connecting N-atoms in the core. The four side chains are shown as blue arrows with length $\bar{d}$, pointing to directions obtained from the 2D histograms of $\theta, \phi$ on the unit sphere, which is attached to the the N-atoms of the core.

## 4.3 Charge-carrier mobility

With the atomistic morphologies at hand, we can now calculate hole and electron mobilities along the columns. To do this, charge hopping rates for neighboring molecules $i$ and $j$ are evaluated using the high-temperature limit of Marcus theory as introduced in eq. 2.6. Since we are looking at a highly ordered system, we have neglected effects of energetic disorder due to electrostatic interactions and conformations (sec. 2.7) so that only the electric field $F$ applied along the column determines energy differences. As we only allow for one-dimensional transport we have

$$\omega_{ij} = \frac{2\pi}{\hbar} \frac{J_{ij}^2}{\sqrt{4\pi\lambda k_\mathrm{B} T}} \exp\left[-\frac{(eF\Delta z_{ij} - \lambda)^2}{4\lambda k_\mathrm{B} T}\right], \tag{4.3}$$

where $e$ is the elementary charge, $\Delta z_{ij}$ is the distance between centers of mass of consecutive molecules in the column, $\lambda$ is the reorganization energy (dominated by internal contributions, see sec. 2.6) and $J_{ij}$ are electronic coupling elements (see sec. 2.5). In contrast to BTDF, where the mesomeric effect leads to delocalization of electron density due to $d$-orbitals in the Si-atom connecting the conjugated core to the phenyl rings (see ch. 3), the side chains in PDI can safely be neglected when evaluating reorganization energies and transfer integrals. This leads to identical reorganization energies of $C_{8,7}$–PDI and TEG–PDI that are analyzed in the next subsection.

### 4.3.1 Reorganization energy

The first parameter entering the rate equation is the reorganization energy. Values of $\lambda_h = 0.14\,\mathrm{eV}$ for holes and $\lambda_e = 0.24\,\mathrm{eV}$ for electrons indicate higher rates and mobilities for holes in both derivatives. The effect of reorganization energy on the relative electron/hole mobility can be quantified in linear response $\Delta E = eF\Delta z \to 0$ if we assume constant transfer integrals and stacking distance. Then eq. 4.3 can be expanded to first order in $\Delta E$ yielding identical rates for both derivatives along ($\omega_+$) and against ($\omega_-$) the direction of the field along the column

$$\omega_\pm = \frac{2\pi}{\hbar} \frac{J^2}{\sqrt{4\pi\lambda k_\mathrm{B} T}} \exp\left(-\frac{\lambda}{4k_\mathrm{B} T}\right)\left[1 \pm \frac{\Delta E}{2k_\mathrm{B} T}\right]. \tag{4.4}$$

If we only allow for hopping between neighbors, the mobility is given by the difference in upward and downward rates (see sec. 2.9.2)

$$\mu = \frac{\langle v \rangle}{F} = \frac{(\omega_+ - \omega_-)\,\Delta z}{F} = \frac{2\pi}{\hbar}\frac{J^2}{\sqrt{4\pi\lambda k_\mathrm{B}T}}\exp\left(-\frac{\lambda}{4k_\mathrm{B}T}\right)\frac{e(\Delta z)^2}{k_\mathrm{B}T}\,. \tag{4.5}$$

Using this expression we can quantify the relative hole and electron mobilities by the ratio

$$\frac{\mu_h}{\mu_e} = \frac{J_h^2}{J_e^2}\times\sqrt{\frac{\lambda_e}{\lambda_h}}\exp\left(-\frac{\lambda_h-\lambda_e}{4k_\mathrm{B}T}\right) =: \frac{J_h^2}{J_e^2}\times C_\lambda\,, \tag{4.6}$$

which defines a constant which in our case is $C_\lambda \approx 4$, indicating that hole transport should be four times faster than electron transport in both derivatives only due to the difference in reorganization energies.

### 4.3.2 Transfer integrals

We now look at distributions of transfer integrals and their effect on charge carrier mobility in columnar systems. In one-dimensional, ordered systems, the overlap of frontier orbitals contributing to the transfer integral is very sensitive to relative orientations and distances of neighbors. The distribution of the center of mass distances between neighbors in a column, shown in fig. 4.2.b, is rather narrow and peaked around $\Delta z = 3.6\,\text{Å}$. This value is in agreement with the WAXS data [162, 165]. Hence, the variation of transfer integrals will be mostly due to the change in relative orientations of neighboring molecules. Due to the strong nematic order ($Q \approx 1$), the relative orientation is determined mostly by the twist angle $\alpha$ between consecutive cores. The dependence of the transfer integrals for electrons and holes based on the overlap of the LUMO and HOMO on this angle $\alpha$ in a dimer where centers of mass are separated by $\Delta z = 3.6\,\text{Å}$ is shown in fig. 4.3.a. The widths of the distributions of the angle $\alpha$ as obtained from MD simulations are also shown in red and black arrows for $C_{8,7}$–PDI and TEG–PDI. One might anticipate that average electronic coupling for electrons in the column is much smaller than that for holes, since the minima of the $J^2_\mathrm{LUMO}$ are close to the maxima of the angle distributions of $C_{8,7}$–PDI at 40° and TEG–PDI at 90°.

In order to verify this hypothesis from the dimer calculation, we have evaluated transfer integrals from all dimers in 1000 snapshots of the MD simulations. Diabatic states (see sec. 2.3) were constructed by replacing the slightly deformed PDI-cores from MD snapshots by geometry optimized rigid copies, while retaining their orientations as explained in ch. 2. Geometry optimization for the PDI-core was performed using the B3LYP hybrid functional and a 6-311G(p,d) basis set. Then integrals were computed using the semi-empirical molecular orbital overlap method [84] based on HOMO and LUMO orbitals of a neutral PDI-core (frozen orbital approximation), which has been shown to yield similar results to density functional theory at a fraction of computational cost. As expected from the dimer calculation, $J_e^2 < J_h^2$ for both derivatives, as shown in fig. 4.3.b.

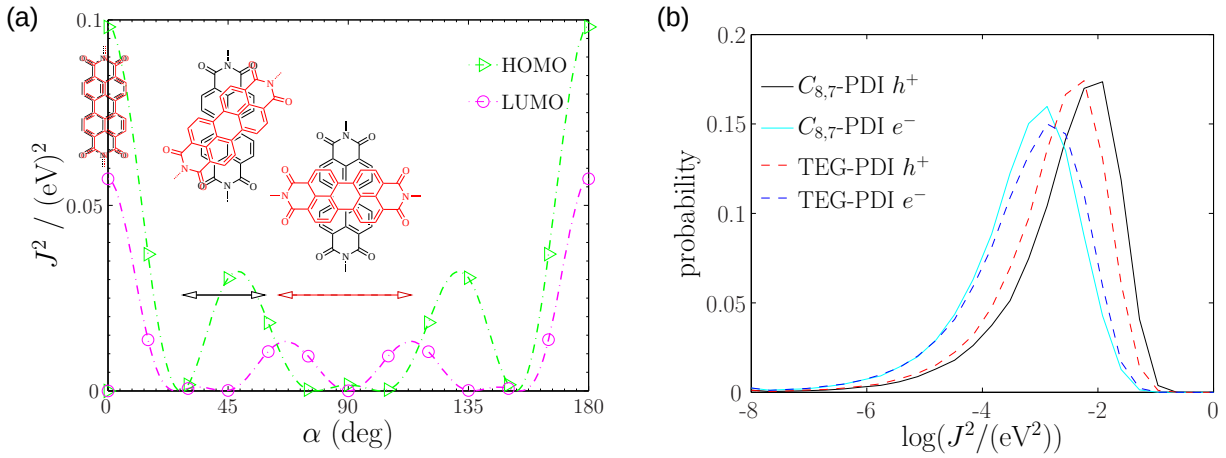


**Figure 4.3.** (a) Transfer integrals for holes (HOMO) and electrons (LUMO) for two isolated molecules at a distance of $\Delta z = 3.6\,\text{Å}$ as a function of the relative pitch angle $\alpha$. The widths of the distributions of pitch angles from MD are indicated using black and red arrows for $C_{8,7}$–PDI and TEG–PDI, respectively. Minima of $J^2_{\text{LUMO}}$ occur near maxima of these distributions at $\alpha = 40°$ ($C_{8,7}$–PDI) and $\alpha = 90°$ (TEG–PDI) indicating lower transfer integrals for electrons in both derivatives. (b) Distribution of transfer integrals for holes and electrons in the two PDI derivatives obtained from all pairs in 16 columns having 60 molecules each evaluated over 1000 snapshots of the MD simulation. Orbital overlap favors hole transport in $C_{8,7}$–PDI and makes electron transport in both derivatives less efficient.

### 4.3.3 The master equation for one-dimensional systems

Having computed integrals, reorganization energy and rates using eq. 4.3, charge carrier mobilities along each column ($N = 60$ molecules) are obtained by solving a stationary, linearized master equation for one carrier hopping along this column

$$0 = \frac{\partial p_i}{\partial t} = \sum_j p_j \omega_{ji} - \sum_j p_i \omega_{ij} \quad \forall i = 1, ..., N \qquad \text{and} \qquad \sum_i p_i = 1\,, \tag{4.7}$$

where $\omega_{ij}$ is the rate for charge transfer from molecule $i$ to the molecule $j$ and the occupation probability $p_i$ to find the charge on molecule $i$ is normalized to 1.

The solution of these $N$ equations can be found by linear algebra when recasting eq. 4.7 in terms of a matrix $R_{ij}$ and including the normalization constraint using a Kronecker delta equal to 1 only in the last ($N^{\text{th}}$) line and zero elsewhere leading to

$$\delta_{iN} = \sum_j R_{ij} p_j \quad \forall i = 1, ..., N\,. \tag{4.8}$$

The matrix $R_{ij}$ is based on the hopping rates between neighbors $\omega_{ij}$. One-dimensional periodic boundary conditions are used to connect the first and last molecule in a column so that $R_{ij} = 0$ except for $i = j \pm 1$ where we define $R_{ij} = \omega_{ij}$. In order to factorize $p_j$ in eq. 4.7 we need to define diagonal elements $R_{ii} = -\sum_j \omega_{ij}$. Finally the normalization

condition is included on the last ($N^{\text{th}}$) line of eq. 4.8 by defining $R_{Nj} = 1\,, \forall j = 1, ..., N$ which makes this equation identical to eq. 4.7. The occupation probabilities $p_i$ can now be obtained by inverting the matrix equation so that $\vec{p} = \hat{R}^{-1}\vec{e}$, where $\vec{e}$ is a $N$-dimensional unit vector with $e_i = \delta_{iN}$.

The mobility in the column is computed from the applied field $F$ and the mean velocity $\langle v \rangle$ constructed from the occupation probabilities $p_i$. Due to periodic boundary conditions and time independent probabilities, the probability flux is constant in the column. This means that the mean velocity in the column of length $L = \sum_i \Delta z_{i,i+1}$ (including $\Delta z_{N,1}$) can be obtained from the probability flux between any two connected molecules which is fully determined by probabilities on these two molecules and the rates between them so that

$$\langle v \rangle = (\omega_{1N} p_N - \omega_{N1} p_1)\, L, \qquad \mu = \frac{\langle v \rangle}{F}\,. \tag{4.9}$$

We have used this approach to compute mobilities individually for all columns in the MD simulation. 1000 MD snapshots during the 40 ns simulation were analyzed to obtain better statistics. The distributions of mobilities are presented in fig. 4.4.a and show the highest mobility for holes in $C_{8,7}$–PDI, slightly lower hole mobilities in TEG–PDI and equally low mobility for electrons in both derivatives. Note that due to the absence of energetic disorder the mobility does not depend on the (small) applied electric field (see sec. 2.7.5).

### 4.3.4 Charge mobility in one-dimensional systems

Since the transfer integral distributions are rather broad and transport is effectively one-dimensional, the charge carrier is likely to encounter a very small transfer integral, i.e. a defect while hopping along the column. In our case, this weak link will lead to a small mobility especially in case of electron transport, where transfer integral distributions have a prominent tail with low values as shown in fig. 4.3.b. Indeed, the averaged mobilities, given in tab. 4.2, show that hole transport is ten time times more efficient than electron transport. This is not only due to the difference in transfer integrals, but also due to the difference in reorganization energy (see eq. 4.6). Note that the observation of higher hole mobility is unexpected since PDI is typically known as an n-type semiconductor [146, 147].

The slightly smaller hole mobility in TEG–PDI compared to $C_{8,7}$–PDI is due to the very broad pitch angle distribution in TEG–PDI that covers the minimum of the HOMO-HOMO overlap around 80° (see fig. 4.3). The narrower distribution for $C_{8,7}$–PDI only covers the minima of the HOMO-HOMO overlap with its tails. Broad distributions of the pitch angle in TEG–PDI result in smaller hole transfer integrals for TEG–PDI as for $C_{8,7}$–PDI, which can be seen in fig. 4.3.b and, hence smaller hole mobility in TEG–PDI.

### 4.3.5 Comparison of mobility to experimental results

The sum of electron and hole mobilities can directly be compared to the mobility measured by pulse-radiolysis time-resolved microwave conductivity (PR-TRMC).

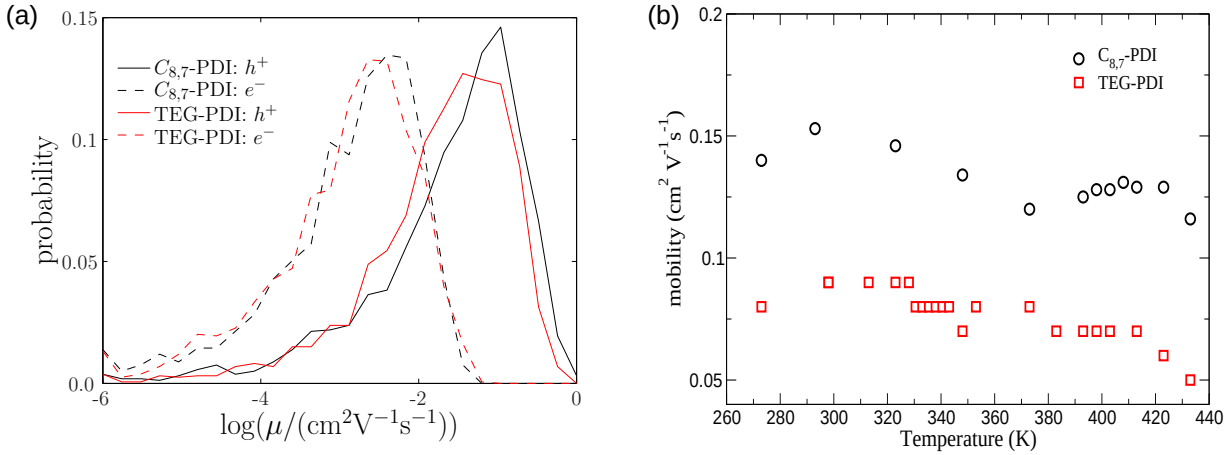


**Figure 4.4.** (a) Distributions of charge carrier mobilities for electrons and holes for $C_{8,7}$–PDI and TEG–PDI. Hole mobilities are larger than electron mobilities for both derivatives. While electron mobilities are similar in $C_{8,7}$–PDI and TEG–PDI, holes are slightly faster in $C_{8,7}$–PDI. (b) Combined electron and hole mobilities as a function of temperature measured by the PR-TRMC technique show a similar trend with slightly higher mobility in TEG–PDI.

In order to perform PR-TRMC measurements powder samples of $C_{8,7}$–PDI and TEG–PDI are introduced into a Ka-band (28-38 GHz) microwave cell. A uniform, micromolar concentration of charge carriers is generated into the sample by a 10 nanosecond pulse of 3 MeV electrons from a Van de Graaff accelerator. The change in the conductivity of the sample resulting from the formation of mobile charge carriers was monitored as a decrease in the microwave power reflected by the sample cell. The one-dimensional, intracolumnar charge carrier mobility was determined from the end-of-pulse conductivity per unit dose, $\frac{\Delta\sigma_{\mathrm{eop}}}{D}$ (measured in units of $\mathrm{Sm}^2/\mathrm{J}$), using the relation

$$\mu = 3\frac{\Delta\sigma_{\mathrm{eop}}}{D}\frac{E_p}{W_p}\,, \tag{4.10}$$

where $E_p$ is the average energy deposited per ionization event and $W_p$ is the probability that initially formed ion-pairs survive until the end of the pulse. Here $E_p = 25\,\mathrm{eV}$ and $W_p = 0.513\,(0.420)$ for $C_{8,7}$–PDI (TEG–PDI). The random orientation of the ordered columnar domains is taken into account by the prefactor 3. The measured mobility $\mu$ is the sum of hole and electron mobilities, $\mu = \mu_+ + \mu_-$, since the PR-TRMC technique does not allow to distinguish the contribution of positive and negative charge carriers.

The temperature dependence of the experimentally measured charge carrier mobility is shown in fig. 4.4.b. The absolute values of the mobility are around 0.15 $\mathrm{cm}^2\mathrm{V}^{-1}\mathrm{s}^{-1}$ and 0.09 $\mathrm{cm}^2\mathrm{V}^{-1}\mathrm{s}^{-1}$ at room temperature for the $C_{8,7}$–PDI and TEG–PDI, respectively. By increasing the temperature to 400K the mobility slightly decreases to 0.13 $\mathrm{cm}^2\mathrm{V}^{-1}\mathrm{s}^{-1}$ and 0.07 $\mathrm{cm}^2\mathrm{V}^{-1}\mathrm{s}^{-1}$, respectively, without showing any abrupt changes which could be related to a phase transition.

Theoretical estimates of the mobility from tab. 4.2 are slightly smaller than found

| | $C_{8,7}$–PDI | TEG–PDI |
|---|---|---|
| $\mu_h$ | 0.087 (±0.03) | 0.053 (±0.02) |
| $\mu_e$ | 0.004 (±0.001) | 0.004 (±0.001) |
| $\mu_e + \mu_h$ | 0.09 (±0.03) | 0.06 (±0.02) |
| $\mu_{\mathrm{PR-TRMC}}$ | 0.15 | 0.09 |

**Table 4.2.** Simulated and experimental mobilities in units of $cm^2V^{-1}s^{-1}$. Values for electron and hole mobilities for both PDI derivatives are obtained by averaging over 16 columns in 1000 MD snapshots of a 40ns trajectory. We also show combined electron and hole mobilities which can be directly compared to measured PR-TRMC mobilities with good relative agreement between TEG–PDI and $C_{8,7}$–PDI. The error of the mean from a bootstrap analysis consisting of 10.000 data sets is given in brackets.

in experiment, which is unusual compared to other compounds that have been studied previously [55, 56, 61, 132]. This implies that the length of a column in the simulation (60 molecules) exceeds the distances sampled by the PR-TRMC technique, which normally probes only 10-20 molecules [162]. As a result, PR-TRMC is relatively insensitive to occasional stacking defects, while they are much more likely in simulations where the columns are three times longer. The relative (combined) mobilities between the two PDI derivatives is however in very good agreement with the experiment.

## 4.4 Summary for one-dimensional charge transport

To summarize we were able to link the value of the helical pitch angle to side chain conformations for two perylenediimide derivatives by comparing theory and experiment. The alkyl side chains prefer a linearly stretched out conformation with the end-to-end vector pointing out of the molecular plane defined by the core. As a result, not only the direct neighbors, but also the next-to-nearest neighbors interact with each other which results in a pitch angle of 40°. The glycol side chains are more flexible and reside in the molecular plane. This leads to a much broader distribution of the pitch angle centered around 90°.

Since the transfer integral for electron transport (LUMO) has minima close to these angles at 40° and 90°, electron transport for both derivatives is less favorable as compared to hole transport, where the minima (HOMO) occur at 25° and 75°. This trend between electrons and holes is even enhanced by a larger reorganization energy of electrons as compared to holes.

Comparing hole transport in both derivatives we find that minima of transfer integrals occur at pitch angles which are less probable in the case of $C_{8,7}$–PDI as compared to TEG–PDI. Computed mobilities, however, show only slightly higher hole mobilities in $C_{8,7}$–PDI than for TEG–PDI. We therefore conclude that, in order to obtain maximal charge-carrier mobilities, it is not sufficient to match the *average* local molecular order induced by the side chains with maxima of the transfer integrals. It is also important to make the corresponding distributions (in this case of the helical pitch angle) as narrow as possible compared to the window determined by the closest minima of the transfer

integral. The immediate implication for compound design is that the side chains should assist the self-assembling process not only via "soft" entropic interactions, but also via stronger specific interactions, such as hydrogen bonding.

Another possibility to improve mobilities would be to allow for two-dimensional charge transport by interconnecting the columns with high electronic couplings. In this case, stacking defects within a column do not limit transport in the network because the charge can take a detour along a different column.

# Chapter 5

# Conclusion and outlook

In this thesis we have extended the methods used for microscopic charge-transport simulations in organic semiconductors and applied this approach to formulate structure-property relations for amorphous host-guest systems and self-assembled discotic mesophases. The contributions to the method development include:

1. The derivation of a bimolecular charge-transfer rate with two independent sets of nuclear coordinates of (quantum-mechanically treated) donor and acceptor molecules in presence of a classical outer-sphere mode (representing the environment). Our observation is that for a situation with (i) intramolecular reorganization energy similar to the outer-sphere one, (ii) reorganization energies of the order of the vibrational energy of the promoting mode (typically a C-C stretching mode), and (iii) small site-energy difference between initial and final state as compared to the intramolecular reorganization energy, results of this bimolecular rate are comparable to the classical Marcus rate and the semi-classical Levich-Jortner expression [19]. However, for systems with large site-energy differences, e.g. when computing escape rates from traps, the bimolecular rate or the Levich-Jortner formalism should be used.

2. The derivation and implementation of a method that allows for efficient evaluation of outer-sphere reorganization energies based on the classical dielectric response of a polarizable environment. Here, donor and acceptor are represented using atomic partial charges while the environment is characterized by atomic charges and the Pekar factor. Our results show that, as expected from the Marcus expression [19], the outer-sphere reorganization energy increases with increasing distance between donor and acceptor. In contrast to the Marcus expression, the proposed method, however, does not lead to unphysical negative values of reorganization energies for very small molecular separations occurring in an amorphous phase. More importantly, we find that the outer-sphere reorganization energy is slightly smaller than the intramolecular one. This observation is confirmed by other approaches [89, 97, 98], which do not rely on explicit knowledge of the Pekar factor, but are also significantly more time-consuming.

3. Investigation of the role of conformational disorder in calculations of intramolecular reorganization energies and internal site energies. The corresponding broadening of the distributions, however, is insignificant compared to the energetic disorder that arises due to electrostatic interactions [64] in the systems under consideration here. Therefore, effects of conformational changes on charge transport are small.

4. The inclusion of self-consistent polarization interactions for calculation of site energies. This is the most important development since an accurate prediction of the energy-landscape is essential for charge-transport simulations in (disordered) amorphous phases [64] and in some cases also in crystalline phases, where fluctuations at room-temperature can lead to significant energetic disorder [132].

From the point of view of applications of the developed methods, the following results were obtained:

- When bulky substituents are attached to an aromatic core in order to adjust energy levels or prevent crystallization, a small amount of delocalization of the frontier orbital to the substituents can increase electronic couplings between neighboring molecules. This leads to improved charge-transfer rates and, hence, larger charge-mobility. We therefore suggest using the *mesomeric effect* (as opposed to the inductive effect) when attaching substituents to aromatic cores, which is necessary for example in deep blue OLEDs, where the energy levels of a host molecule have to be adjusted to those of the emitter.

- The energy landscape for charges in an amorphous phase cannot be predicted by mesoscopic models because they approximate the realistic morphology by a lattice and represent molecular charge distributions in a multipole expansion. The microscopic approach shows that a polarization-induced stabilization of a molecule in its charged and neutral states can lead to large shifts, broadening, and traps in the distribution of site energies. These results are especially important for multi-component systems (the emission layer of an OLED or the donor-acceptor interface of an OPVC), if the change in polarizability upon charging (or excitation in case of energy transport) is different for the components. Thus, the *polarizability change* upon charging or excitation should be added to the set of molecular parameters essential for understanding charge and energy transport in organic semiconductors.

- In case of one-dimensional charge transport in self-assembled systems, intermolecular packing motives induced by side chains can increase electronic couplings between molecules. This leads to larger charge mobility, which is essential for devices such as OFETs. However, it is not sufficient to match the *average* local molecular order induced by the side chains with maxima of the electronic couplings. It is also important to make the corresponding distributions, e.g. of the pitch angle between consecutive molecules, as narrow as possible compared to the window determined by the closest minima of the electronic couplings [19]. The immediate implication for

compound design is that the side chains should assist the self-assembling process not only via "soft" entropic interactions, but also via stronger specific interactions, such as hydrogen bonding.

The current set of simulation methods provides a good understanding of microscopic charge-transport processes occurring in organic semiconductors including prediction of topological connectivity from electronic couplings, energetic landscape, charge mobilities, site occupations and currents. However, there are still a number of challenges before in silico design of *devices* based on organic semiconductors can be performed including:

1. Prediction of non-equilibrium and self-assembled morphologies. In amorphous phases considered here, the different static dipole moments of guest(emitter) molecules and host molecules lead to emitter aggregation during vacuum deposition of the OLED emission layer. Including aggregation effects is especially important to predict charge transport in the minority component of the emission layer. This cannot be achieved by annealing the host-guest mixture above the glass transition and quenching it to room temperature since this procedure completely randomizes positions and orientations of guest molecules in the host. An alternative is the simulation of the gradual adsorption of molecules on a substrate, either by using Monte Carlo moves and treating molecules as rigid rotors [52] or by employing molecular dynamics and sublimating molecules at high temperatures [65]. The drawback of the first method is that the molecular conformations are always fixed, while the second method is limited to microsecond simulation times, which might be too short to fully relax positions and orientations of adsorbed molecules [167].

2. Parametrization of polarizable force fields allowing for strongly anisotropic molecular polarizability tensors. This is needed for an accurate evaluation of the energy landscape since in the Thole model, the anisotropy of the polarizabilities for charged molecules is often underestimated. This deficiency can be cured by allowing for anisotropic atomic polarizabilities and virtual polarizable sites. Alternatively, other methods such as charge-equilibration can be employed [102].

3. Accurate and efficient evaluation of outer-sphere reorganization energies that do not rely on the Pekar factor. Here, polarizable force fields are essential to improve the prediction of the dielectric response of the environment from molecular dynamics simulations [89, 98]. Outer-sphere reorganization energies are especially important to predict de-trapping of charges in energetically deep lying states that are created by impurities such as oxygen or water with a negative effect on device stability for OLEDs, OPVC and OFETs.

4. Charge injection or extraction. Since organic materials are intrinsic insulators, charges have to be photo-generated or injected at a metallic interface, where image-charge effects occur. Furthermore, the build-up of space-charge at an ohmic contact due to a low mobility has to be considered [168].

5. Development of off-lattice KMC algorithms for multiple charge carriers. This is essential to describe the influence of a realistic carrier density on mobility [112] which is especially important for OFETs where densities are higher than in OLEDs or OPVCs. While in lattice models the interaction between the charges can mainly be taken into account by excluding double occupancy of sites [36], it is not clear whether this is also true in off-lattice simulations based on a realistic morphology.

6. Efficient site-energy calculations for multiple charge carriers including polarization effects. For KMC simulations with interacting charge carriers, site energies cannot simply be computed once for all sites before the start of the KMC simulation, but have to be evaluated on the fly after each KMC step, which makes efficient algorithms necessary.

7. Processes involving excited states. Excited states are an important ingredient of functionality in OLEDs and OPVC. An adaptation of the state-based description for excitons is intrinsically challenging due to their diverse character including singlet and triplet states, strongly-bound Frenkel excitations localized on single molecules, charge-transfer excitons involving a donor-acceptor complex and long-range polaron pairs. Analogues of diabatic states (energies, wavefunctions) have to be determined for all types of excitations using suitable first-principles descriptions. Accurate quantum-chemical methods, such as coupled-cluster, configuration-interaction are capable of this but come at high computational cost. Time-dependent density-functional theory is less demanding but has problems describing long-range asymptotics of the electron-electron interaction potential [169], affecting charge-transfer states in particular. Range-separated exchange-correlation kernels [170, 171] may be used to overcome this deficiency but need compound-specific adjustments [172, 173]. Here, many-body Green's functions theory using the *GW* approximation and the Bethe-Salpeter equation [133, 174] is a feasible alternative as it allows for the calculation of energies and wavefunctions of excitepd states at a required accuracy, while computational demands remain manageable. For singlet (triplet) exciton dynamics, one can use Förster (Dexter) energy transfer rates or use a more general expression based on the excitonic wave functions [175, 176]. Furthermore, the long-range nature of the exchange interaction of singlet excitons will result in a different topology of the directed graph used in KMC simulations (as compared to charge transport), requiring large system sizes.

8. KMC simulations with electrons, holes, and excitons. For simulations in OLEDs and OPVC processes such as recombination of electrons and holes to form excitons (and their dissociation) or the conversion between Frenkel and charge-transfer excitons have to be considered.

# Bibliography


[1] C. K. Chiang, C. R. Fincher, Y. W. Park, A. J. Heeger, H. Shirakawa, E. J. Louis, S. C. Gau, and Alan G. MacDiarmid. Electrical conductivity in doped polyacetylene. *Phys. Rev. Lett.*, 39(17):1098–1101, 1977.

[2] Michael Sommer, Sven Hüttner, and Mukundan Thelakkat. Donor–acceptor block copolymers for photovoltaic applications. *J. Mater. Chem.*, 20(48):10788, 2010.

[3] Ana Claudia Arias, J. Devin MacKenzie, Iain McCulloch, Jonathan Rivnay, and Alberto Salleo. Materials and applications for large area electronics: Solution-Based approaches. *Chem. Rev.*, 110(1):3–24, 2010.

[4] Amaresh Mishra, Chang-Qi Ma, and Peter Bäuerle. Functional oligothiophenes: Molecular design for multidimensional nanoarchitectures and their applications. *Chem. Rev.*, 109(3):1141–1276, 2009.

[5] Jishan Wu, Wojciech Pisula, and Klaus Müllen. Graphenes as potential material for electronics. *Chem. Rev.*, 107(3):718–747, 2007.

[6] Sybille Allard, Michael Forster, Benjamin Souharce, Heiko Thiem, and Ullrich Scherf. Organic semiconductors for Solution-Processable Field-Effect transistors (OFETs). *Angew. Chem. Int. Edit.*, 47(22):4070–4098, 2008.

[7] John E. Anthony. Functionalized acenes and heteroacenes for organic electronics. *Chem. Rev.*, 106(12):5028–5048, 2006.

[8] John E. Anthony, Antonio Facchetti, Martin Heeney, Seth R. Marder, and Xiaowei Zhan. n-Type organic semiconductors in organic electronics. *Adv. Mater.*, 22(34): 3876–3892, 2010.

[9] K. Walzer, B. Maennig, M. Pfeiffer, and K. Leo. Highly efficient organic devices based on electrically doped transport layers. *Chem. Rev.*, 107(4):1233–1271, 2007.

[10] Adam J. Moulé and Klaus Meerholz. Morphology control in Solution-Processed Bulk-Heterojunction solar cell mixtures. *Adv. Funct. Mater.*, 19(19):3028–3036, 2009.

[11] Iain McCulloch, Martin Heeney, Clare Bailey, Kristijonas Genevicius, Iain MacDonald, Maxim Shkunov, David Sparrowe, Steve Tierney, Robert Wagner, Weimin Zhang, Michael L. Chabinyc, R. Joseph Kline, Michael D. McGehee, and Michael F. Toney. Liquid-crystalline semiconducting polymers with high charge-carrier mobility. *Nat. Mater.*, 5(4):328–333, 2006.

[12] Christian Müller, Toby A. M. Ferenczi, Mariano Campoy-Quiles, Jarvist M. Frost, Donal D. C. Bradley, Paul Smith, Natalie Stingelin-Stutzmann, and Jenny Nelson. Binary organic photovoltaic blends: A simple rationale for optimum compositions. *Adv. Mater.*, 20(18):3510–3515, 2008.

[13] A. Zen, J. Pflaum, S. Hirschmann, W. Zhuang, F. Jaiser, U. Asawapirom, J. P. Rabe, U. Scherf, and D. Neher. Effect of molecular weight and annealing of poly(3-hexylthiophene)s on the performance of organic Field-Effect transistors. *Adv. Funct. Mater.*, 14(8):757–764, 2004.

[14] R.J. Kline, M.D. McGehee, E.N. Kadnikova, J. Liu, and J.M.J. Fréchet. Controlling the Field-Effect mobility of regioregular polythiophene by changing the molecular weight. *Adv. Mater.*, 15(18):1519–1522, 2003.

[15] H. Sirringhaus, P. J. Brown, R. H. Friend, M. M. Nielsen, K. Bechgaard, B. M. W. Langeveld-Voss, A. J. H. Spiering, R. A. J. Janssen, E. W. Meijer, P. Herwig, and D. M. de Leeuw. Two-dimensional charge transport in self-organized, high-mobility conjugated polymers. *Nature*, 401(6754):685–688, 1999.

[16] Barry P. Rand, Jan Genoe, Paul Heremans, and Jef Poortmans. Solar cells utilizing small molecular weight organic semiconductors. *Prog. Photovoltaics*, 15(8):659–676, 2007.

[17] C. W Tang. Two-layer organic photovoltaic cell. *Appl. Phys. Lett.*, 48(2):183–185, 1986.

[18] Heliatek GmbH press release, webpage accessed on 10.05.2012. http://www.heliatek.com, 2011.

[19] Volkhard May and Oliver Kühn. *Charge and Energy Transfer Dynamics in Molecular Systems*. Wiley-VCH, 3rd, revised and enlarged edition edition, 2011. ISBN 3527407324.

[20] Jean-Luc Brédas, Joseph E. Norton, Jérôme Cornil, and Veaceslav Coropceanu. Molecular understanding of organic solar cells: The challenges. *Accounts Chem. Res.*, 42(11):1691–1699, 2009.

[21] P. M. Borsenberger, L. Pautmeier, and H. Bässler. Charge transport in disordered molecular solids. *J. Chem. Phys.*, 94(8):5447, 1991.

[22] H. H. Fong and S. K. So. Hole transporting properties of tris(8-hydroxyquinoline) aluminum (alq3). *J. Appl. Phys.*, 100(9):094502–5, 2006.

[23] S. V. Novikov, D. H. Dunlap, V. M. Kenkre, P. E. Parris, and A. V. Vannikov. Essential role of correlations in governing charge transport in disordered organic materials. *Phys. Rev. Lett.*, 81(20):4472, 1998.

[24] V. Podzorov, E. Menard, A. Borissov, V. Kiryukhin, J. A. Rogers, and M. E. Gershenson. Intrinsic charge transport on the surface of organic semiconductors. *Phys. Rev. Lett.*, 93(8):086602, 2004.

[25] Gilles Horowitz. Organic Field-Effect transistors. *Adv. Mater.*, 10(5):365–377, 1998.

[26] Zhenan Bao, Andrew J. Lovinger, and Janelle Brown. New Air-Stable n-Channel organic thin film transistors. *J. Am. Chem. Soc.*, 120(1):207–208, 1998.

[27] Carsten Deibel and Vladimir Dyakonov. Polymer–fullerene bulk heterojunction solar cells. *Reports on Progress in Physics*, 73(9):096401, 2010.

[28] N. C. Giebink, B. W. D'Andrade, M. S. Weaver, J. J. Brown, and S. R. Forrest. Direct evidence for degradation of polaron excited states in organic light emitting diodes. *J. Appl. Phys.*, 105(12):124514, 2009.

[29] Mark E. Thompson, Paul E. Burrows, and Stephen R. Forrest. Electrophosphorescence in organic light emitting diodes. *Curr. Opin. Solid State Mater. Sci.*, 4(4): 369–372, 1999.

[30] Peter Erk, Markus Bold, Martina Egen, Evelyn Fuchs, Thomas Gessner, Klaus Kahle, Christian Lennartz, Oliver Molt, Simon Nord, Helmut Reichelt, Christian Schildknecht, Hans-Herrmann Johannes, and Wolfgang Kowalsky. Efficient deep blue triplet emitters for OLEDs. *SID Symposium Digest of Technical Papers*, 37(1): 131–134, 2006.

[31] J. Kirkpatrick, V. Marcon, J. Nelson, K. Kremer, and D. Andrienko. Charge mobility of discotic mesophases: A multiscale quantum and classical study. *Phys. Rev. Lett.*, 98(22):227402, 2007.

[32] Veaceslav Coropceanu, Jérôme Cornil, Demetrio A. da Silva Filho, Yoann Olivier, Robert Silbey, and Jean-Luc Brédas. Charge transport in organic semiconductors. *Chem. Rev.*, 107(4):926–952, 2007.

[33] Alessandro Troisi, David L. Cheung, and Denis Andrienko. Charge transport in semiconductors with multiscale conformational dynamics. *Phys. Rev. Lett.*, 102(11): 116602, 2009.

[34] W. F. Pasveer, J. Cottaar, C. Tanase, R. Coehoorn, P. A. Bobbert, P. W. M. Blom, D. M. de Leeuw, and M. A. J. Michels. Unified description of Charge-Carrier mobilities in disordered semiconducting polymers. *Phys. Rev. Lett.*, 94(20):206601, 2005.

[35] J. Cottaar, L. J. A. Koster, R. Coehoorn, and P. A. Bobbert. Scaling theory for percolative charge transport in disordered molecular semiconductors. *Phys. Rev. Lett.*, 107(13):136601, 2011.

[36] J. J. M. van der Holst, F. W. A. van Oost, R. Coehoorn, and P. A. Bobbert. Monte carlo study of charge transport in organic sandwich-type single-carrier devices: Effects of coulomb interactions. *Phys. Rev. B*, 83(8):085206, 2011.

[37] H. Bässler. Charge transport in disordered organic photoconductors a monte carlo simulation study. *Phys. Status Solidi B*, 175(1):15–56, 1993.

[38] Y.Y. Yimer, P.A. Bobbert, and R. Coehoorn. Charge transport in disordered organic host–guest systems: Effects of carrier density and electric field. *Synthetic Metals*, 159 (21-22):2399–2401, 2009.

[39] Milind Misra, Denis Andrienko, Björn Baumeier, Jean-Loup Faulon, and O. Anatole von Lilienfeld. Toward quantitative Structure–Property relationships for charge transfer rates of polycyclic aromatic hydrocarbons. *J. Chem. Theory Comput.*, 7(8): 2549–2555, 2011.

[40] Kevin M. Coakley and Michael D. McGehee. Conjugated polymer photovoltaic cells. *Chem. Mater.*, 16(23):4533–4542, 2004.

[41] Ferdinand C. Grozema and Laurens D. A. Siebbeles. Mechanism of charge transport in self-organizing organic materials. *Int. Rev. Phys. Chem.*, 27(1):87–138, 2008.

[42] Sven Stafström. Electron localization and the transition from adiabatic to nonadiabatic charge transport in organic conductors. *Chem. Soc. Rev.*, 39(7):2484, 2010.

[43] D. A. da Silva Filho, E.-G. Kim, and J.-L. Brédas. Transport properties in the rubrene crystal: Electronic coupling and vibrational reorganization energy. *Adv. Mater.*, 17(8):1072–1076, 2005.

[44] Edgar A. Silinsh and Vladislav Capek. *Organic Molecular Crystals: Interacton Localization, and Transport Phenomena*. American Institute of Physics, 1 edition, 1997. ISBN 1563960699.

[45] R. Silbey and R. W. Munn. General theory of electronic transport in molecular crystals. i. local linear electron–phonon coupling. *J. Chem. Phys.*, 72(4):2763, 1980.

[46] K. Hannewald, V. M. Stojanović, J. M. T. Schellekens, P. A. Bobbert, G. Kresse, and J. Hafner. Theory of polaron bandwidth narrowing in organic molecular crystals. *Phys. Rev. B*, 69(7):075211, 2004.

[47] David L. Cheung and Alessandro Troisi. Modelling charge transport in organic semiconductors: from quantum dynamics to soft matter. *Phys. Chem. Chem. Phys.*, 10 (39):5941, 2008.

[48] David P. McMahon and Alessandro Troisi. Organic semiconductors: Impact of disorder at different timescales. *ChemPhysChem*, 11(10):2067–2074, 2010.

[49] Y. Olivier, L. Muccioli, V. Lemaur, Y. H. Geerts, C. Zannoni, and J. Cornil. Theoretical characterization of the structural and hole transport dynamics in Liquid-Crystalline phthalocyanine stacks. *J. Phys. Chem. B*, 113(43):14102–14111, 2009.

[50] Eugenio Di Donato, Rocco P. Fornari, Simone Di Motta, Yan Li, Zhaohui Wang, and Fabrizia Negri. n-Type charge transport and mobility of fluorinated perylene bisimide semiconductors. *J. Phys. Chem. B*, 114(16):5327–5334, 2010.

[51] Jenny Nelson, Joe J. Kwiatkowski, James Kirkpatrick, and Jarvist M. Frost. Modeling charge transport in organic photovoltaic materials. *Accounts Chem. Res.*, 42 (11):1768–1778, 2009.

[52] J. J. Kwiatkowski, J. Nelson, H. Li, J. L. Brédas, W. Wenzel, and C. Lennartz. Simulating charge transport in tris(8-hydroxyquinoline) aluminium (Alq3). *Phys. Chem. Chem. Phys.*, 10(14):1852, 2008.

[53] Yuki Nagata and Christian Lennartz. Atomistic simulation on charge mobility of amorphous tris(8-hydroxyquinoline) aluminum (alq3): Origin of Poole–Frenkel–type behavior. *J. Chem. Phys.*, 129(3):034709, 2008.

[54] J. Kirkpatrick, V. Marcon, K. Kremer, J. Nelson, and D. Andrienko. Columnar mesophases of hexabenzocoronene derivatives. II. charge carrier mobility. *J. Chem. Phys.*, 129(9):094506, 2008.

[55] Alexander Lukyanov and Denis Andrienko. Extracting nondispersive charge carrier mobilities of organic semiconductors from simulations of small systems. *Phys. Rev. B*, 82(19):193202, 2010.

[56] Thorsten Vehoff, Björn Baumeier, Alessandro Troisi, and Denis Andrienko. Charge transport in organic crystals: Role of disorder and topological connectivity. *J. Am. Chem. Soc.*, 132(33):11702–11708, 2010.

[57] Thorsten Vehoff, Yeon Sook Chung, Karen Johnston, Alessandro Troisi, Do Y. Yoon, and Denis Andrienko. Charge transport in Self-Assembled semiconducting organic layers: Role of dynamic and static disorder. *J. Phys. Chem. C*, 114(23):10592–10597, 2010.

[58] Thorsten Vehoff, Björn Baumeier, and Denis Andrienko. Charge transport in columnar mesophases of carbazole macrocycles. *J. Chem. Phys.*, 133(13):134901, 2010.

[59] Victor Rühle, James Kirkpatrick, and Denis Andrienko. A multiscale description of charge transport in conjugated oligomers. *J. Chem. Phys.*, 132(13):134103, 2010.

[60] Valentina Marcon, Dag W. Breiby, Wojciech Pisula, Julie Dahl, James Kirkpatrick, Sameer Patwardhan, Ferdinand Grozema, and Denis Andrienko. Understanding Structure-Mobility relations for perylene tetracarboxydiimide derivatives. *J. Am. Chem. Soc.*, 131(32):11426–11432, 2009.

[61] Xinliang Feng, Valentina Marcon, Wojciech Pisula, Michael Ryan Hansen, James Kirkpatrick, Ferdinand Grozema, Denis Andrienko, Kurt Kremer, and Klaus Müllen. Towards high charge-carrier mobilities by rational design of the shape and periphery of discotics. *Nat. Mater.*, 8(5):421–426, 2009.

[62] Linjun Wang, Guangjun Nan, Xiaodi Yang, Qian Peng, Qikai Li, and Zhigang Shuai. Computational methods for design of organic materials with high charge mobility. *Chem. Soc. Rev.*, 39(2):423, 2010.

[63] Victor Rühle, Christoph Junghans, Alexander Lukyanov, Kurt Kremer, and Denis Andrienko. Versatile Object-Oriented toolkit for Coarse-Graining applications. *J. Chem. Theory. Comput.*, 5(12):3211–3223, 2009.

[64] Victor Rühle, Alexander Lukyanov, Falk May, Manuel Schrader, Thorsten Vehoff, James Kirkpatrick, Björn Baumeier, and Denis Andrienko. Microscopic simulations of charge transport in disordered organic semiconductors. *J. Chem. Theory Comput.*, 7(10):3335–3345, 2011.

[65] Luca Muccioli, Gabriele D'Avino, and Claudio Zannoni. Simulation of Vapor-Phase deposition and growth of a pentacene thin film on C(60) (001). *Adv. Mater.*, 23(39): 4532–+, 2011.

[66] U. Chandra Singh and Peter A Kollman. An approach to computing electrostatic charges for molecules. *J. Comput. Chem.*, 5(2):129–145, 1984.

[67] Brent H Besler, Kenneth M Merz Jr., and Peter A Kollman. Atomic charges derived from semiempirical methods. *J. Comput. Chem.*, 11(4):431–439, 1990.

[68] William L. Jorgensen and Julian. Tirado-Rives. The OPLS [optimized potentials for liquid simulations] potential functions for proteins, energy minimizations for crystals of cyclic peptides and crambin. *J. Am. Chem. Soc.*, 110(6):1657–1666, 1988.

[69] William L Jorgensen and Julian Tirado–Rives. Molecular modeling of organic and biomolecular systems using BOSS and MCPRO. *J. Comput. Chem.*, 26(16):1689–1700, 2005.

[70] Nora A. McDonald and William L. Jorgensen. Development of an All-Atom force field for heterocycles. properties of liquid pyrrole, furan, diazoles, and oxazoles. *J. Phys. Chem. B*, 102(41):8049–8059, 1998.

[71] V. Rühle, J. Kirkpatrick, K. Kremer, and D. Andrienko. Coarse-grained modelling of polypyrrole morphologies. *Phys. Stat. Solidi B*, 245:844, 2008.

[72] Valentina Marcon, Thorsten Vehoff, James Kirkpatrick, Cheol Jeong, Do Y. Yoon, Kurt Kremer, and Denis Andrienko. Columnar mesophases of hexabenzocoronene derivatives. i. phase transitions. *J. Chem. Phys.*, 129(9):094505, 2008.

[73] L. Martínez, R. Andrade, E. G Birgin, and J. M Martínez. PACKMOL: a package for building initial configurations for molecular dynamics simulations. *J. Comput. Chem.*, 30(13):2157–2164, 2009.

[74] Giovanni Bussi, Davide Donadio, and Michele Parrinello. Canonical sampling through velocity rescaling. *J. Chem. Phys.*, 126(1):014101, 2007.

[75] H. J. C. Berendsen, J. P. M. Postma, W. F. van Gunsteren, A. DiNola, and J. R. Haak. Molecular dynamics with coupling to an external bath. *J. Chem. Phys.*, 81 (8):3684, 1984.

[76] L. Perera and Essmann. A smooth particle mesh ewald potential. *Journal of Chemical Physics*, 103:8577–8592, 1995.

[77] Nenad Vukmirović and Lin-Wang Wang. Charge patching method for electronic structure of organic systems. *J. Chem. Phys.*, 128(12):121102, 2008.

[78] Nenad Vukmirović and Lin-Wang Wang. Charge carrier motion in disordered conjugated polymers: A multiscale ab initio study. *Nano Letters*, 9(12):3996–4000, 2009.

[79] David P. McMahon and Alessandro Troisi. An ad hoc tight binding method to study the electronic structure of semiconducting polymers. *Chem. Phys. Lett.*, 480(4-6): 210–214, 2009.

[80] A B Walker, A Kambili, and S J Martin. Electrical transport modelling in organic electroluminescent devices. *J. Phys-Condens. Mat.*, 14(42):9825–9876, 2002.

[81] Allen Miller and Elihu Abrahams. Impurity conduction at low concentrations. *Phys. Rev.*, 120(3):745–755, 1960.

[82] Jean-Luc Brédas, David Beljonne, Veaceslav Coropceanu, and Jerome Cornil. Charge-Transfer and Energy-Transfer processes in pi-conjugated oligomers and polymers: A molecular picture. *Chem. Rev.*, 104(11):4971–5004, 2004.

[83] Björn Baumeier, James Kirkpatrick, and Denis Andrienko. Density-functional based determination of intermolecular charge transfer properties for large-scale morphologies. *Phys. Chem. Chem. Phys.*, 12(36):11103, 2010.

[84] James Kirkpatrick. An approximate method for calculating transfer integrals based on the ZINDO hamiltonian. *Int. J. Quantum Chem.*, 108(1):51–56, 2008.

[85] Rudolph A. Marcus. Electron transfer reactions in chemistry. theory and experiment. *Rev. Mod. Phys.*, 65(3):599, 1993.

[86] Geoffrey R. Hutchison, Mark A. Ratner, and Tobin J. Marks. Hopping transport in conductive heterocyclic oligomers: Reorganization energies and substituent effects. *J. Am. Chem. Soc.*, 127(7):2339–2350, 2005.

[87] J. Casado-Pascual, I. Goychuk, M. Morillo, and P. Hänggi. Solvent controlled charge transfer dynamics on diabatic surfaces with different curvatures. *Chem. Phys. Lett.*, 360(3-4):333–339, 2002.

[88] Jia-Lin Chang. A new formula to calculate Franck-Condon factors for displaced and distorted harmonic oscillators. *J. Mol. Spectrosc.*, 232(1):102–104, 2005.

[89] David P. McMahon and Alessandro Troisi. Evaluation of the external reorganization energy of polyacenes. *J. Phys. Chem. Lett.*, 1(6):941–946, 2010.

[90] Jingsong Huang and Miklos Kertesz. Intermolecular transfer integrals for organic molecular materials: can basis set convergence be achieved? *Chem. Phys. Lett.*, 390 (1-3):110–115, 2004.

[91] Jingsong Huang and Miklos Kertesz. Validation of intermolecular transfer integral and bandwidth calculations for organic molecular materials. *J. Chem. Phys.*, 122 (23):234707–9, 2005.

[92] Edward F. Valeev, Veaceslav Coropceanu, Demetrio A. da Silva Filho, Seyhan Salman, and Jean-Luc Brédas. Effect of electronic polarization on Charge-Transport parameters in molecular organic semiconductors. *J. Am. Chem. Soc.*, 128(30):9882–9886, 2006.

[93] Shiwei Yin, Yuanping Yi, Qingxu Li, Gui Yu, Yunqi Liu, and Zhigang Shuai. Balanced carrier transports of electrons and holes in silole-based compounds. A theoretical study. *J. Phys. Chem. A*, 110(22):7138–7143, 2006.

[94] Xiaodi Yang, Qikai Li, and Zhigang Shuai. Theoretical modelling of carrier transports in molecular semiconductors: molecular design of triphenylamine dimer systems. *Nanotechnology*, 18(42):424029, 2007.

[95] Ansgar Schäfer, Christian Huber, and Reinhart Ahlrichs. Fully optimized contracted gaussian basis sets of triple zeta valence quality for atoms li to kr. *J. Chem. Phys.*, 100(8):5829, 1994.

[96] Toshiaki. Kakitani and Noboru. Mataga. Comprehensive study on the role of coordinated solvent mode played in electron-transfer reactions in polar solutions. *J. Phys. Chem.*, 91(24):6277–6285, 1987.

[97] Nicolas G. Martinelli, Julien Idé, Roel S. Sánchez-Carrera, Veaceslav Coropceanu, Jean-Luc Brédas, Laurent Ducasse, Frédéric Castet, Jérôme Cornil, and David Beljonne. Influence of structural dynamics on polarization energies in anthracene single crystals. *J. Phys. Chem. C*, 114(48):20678–20685, 2010.

[98] Joseph E. Norton and Jean-Luc Brédas. Polarization energies in oligoacene semiconductor crystals. *J. Am. Chem. Soc.*, 130(37):12377–12384, 2008.

[99] D. Dunlap, P. Parris, and V. Kenkre. Charge-Dipole model for the universal field dependence of mobilities in molecularly doped polymers. *Phys. Rev. Lett.*, 77(3): 542–545, 1996.

[100] Conor Madigan and Vladimir Bulović. Charge carrier energy disorder in polar amorphous organic thin films. *Phys. Rev. Lett.*, 97(21):216402, 2006.

[101] Valerie Daggett, Peter A. Kollman, and Irwin D. Kuntz. Molecular dynamics simulations of small peptides: Dependence on dielectric model and pH. *Biopolymers*, 31 (3):285–304, 1991.

[102] Razvan A. Nistor and Martin H. Müser. Dielectric properties of solids in the regular and split-charge equilibration formalisms. *Phys. Rev. B*, 79(10):104303, 2009.

[103] Stijn Verlaak and Paul Heremans. Molecular microelectrostatic view on electronic states near pentacene grain boundaries. *Phys. Rev. B*, 75(11):115127, 2007.

[104] B.T. Thole. Molecular polarizabilities calculated with a modified dipole interaction. *Chem. Phys.*, 59(3):341–350, 1981.

[105] Piet Th. van Duijnen and Marcel Swart. Molecular and atomic polarizabilities: Thole's model revisited. *J. Phys. Chem. A*, 102(14):2399–2407, 1998.

[106] Jay W. Ponder, Chuanjie Wu, Pengyu Ren, Vijay S. Pande, John D. Chodera, Michael J. Schnieders, Imran Haque, David L. Mobley, Daniel S. Lambrecht, Robert A. DiStasio, Martin Head-Gordon, Gary N. I. Clark, Margaret E. Johnson, and Teresa Head-Gordon. Current status of the AMOEBA polarizable force field. *J. Phys. Chem. B*, 114(8):2549–2564, 2010.

[107] Pengyu Ren and Jay W. Ponder. Polarizable atomic multipole water model for molecular mechanics simulation. *J. Phys. Chem. B*, 107(24):5933–5947, 2003.

[108] Richard P. Feynman, Robert B. Leighton, and Matthew Sands. *Lectures on Physics: Commemorative Issue Vol 2.* Addison Wesley, 1971. ISBN 9780201021172.

[109] Bernard Derrida. Velocity and diffusion constant of a periodic one-dimensional hopping model. *J. Stat. Phys.*, 31(3):433–450, 1983.

[110] Sergey V. Novikov and Anatoly V. Vannikov. Cluster structure in the distribution of the electrostatic potential in a lattice of randomly oriented dipoles. *J. Phys. Chem.*, 99(40):14573–14576, 1995.

[111] J. Cottaar and P. A. Bobbert. Calculating charge-carrier mobilities in disordered semiconducting polymers: Mean field and beyond. *Phys. Rev. B*, 74(11):115204, 2006.

[112] R. Coehoorn, W. F. Pasveer, P. A. Bobbert, and M. A. J. Michels. Charge-carrier concentration dependence of the hopping mobility in organic materials with gaussian disorder. *Phys. Rev. B*, 72(15):155206, 2005.

[113] B. Movaghar, M. Grünewald, B. Ries, H. Bassler, and D. Würtz. Diffusion and relaxation of energy in disordered organic and inorganic materials. *Phys. Rev. B*, 33 (8):5545–5554, 1986.

[114] Harvey Scher and Elliott Montroll. Anomalous transit-time dispersion in amorphous solids. *Phys. Rev. B*, 12(6):2455–2477, 1975.

[115] P. M. Borsenberger, E. H. Magin, M. Der VanAuweraer, and F. C. De Schryver. The role of disorder on charge transport in molecularly doped polymers and related materials. *Phys. Status Solidi A*, 140(1):9–47, 1993.

[116] H. Cordes, S. D. Baranovskii, K. Kohary, P. Thomas, S. Yamasaki, F. Hensel, and J.-H. Wendorff. One-dimensional hopping transport in disordered organic solids. i. analytic calculations. *Phys. Rev. B*, 63(9):094201, 2001.

[117] Kazuhiko Seki and M. Tachiya. Electric field dependence of charge mobility in energetically disordered materials: Polaron aspects. *Phys. Rev. B*, 65(1):014305, 2001.

[118] Stephen R. Forrest. The path to ubiquitous and low-cost organic electronic appliances on plastic. *Nature*, 428(6986):911–918, 2004.

[119] Sebastian Reineke, Frank Lindner, Gregor Schwartz, Nico Seidler, Karsten Walzer, Bjorn Lussem, and Karl Leo. White organic light-emitting diodes with fluorescent tube efficiency. *Nature*, 459(7244):234–238, 2009.

[120] R. J. Holmes, S. R. Forrest, Y.-J. Tung, R. C. Kwong, J. J. Brown, S. Garon, and M. E. Thompson. Blue organic electrophosphorescence using exothermic host–guest energy transfer. *Appl. Phys. Lett.*, 82(15):2422, 2003.

[121] Hartmut Yersin. Triplet emitters for OLED applications. mechanisms of exciton trapping and control of emission properties. *Top. Curr. Chem.*, 241:1–26, 2004.

[122] Chihaya Adachi, Raymond C. Kwong, Peter Djurovich, Vadim Adamovich, Marc A. Baldo, Mark E. Thompson, and Stephen R. Forrest. Endothermic energy transfer: A mechanism for generating very efficient high-energy phosphorescent emission in organic materials. *Appl. Phys. Lett.*, 79(13):2082, 2001.

[123] R. J. Holmes, B. W. D'Andrade, S. R. Forrest, X. Ren, J. Li, and M. E. Thompson. Efficient, deep-blue organic electrophosphorescence by guest charge trapping. *Appl. Phys. Lett.*, 83(18):3818, 2003.

[124] Hisahiro Sasabe, Jun-ichi Takamatsu, Takao Motoyama, Soichi Watanabe, Gerhard Wagenblast, Nicolle Langer, Oliver Molt, Evelyn Fuchs, Christian Lennartz, and Junji Kido. High-Efficiency blue and white organic Light-Emitting devices incorporating a blue iridium carbene complex. *Adv. Mater.*, 22(44):5003–5007, 2010.

[125] Cheng-Han Hsieh, Fang-Iy Wu, Chun-Hsiang Fan, Min-Jie Huang, Kun-Yi Lu, Pei-Yu Chou, Yu-Han Ou Yang, Shih-Hsiang Wu, I-Chia Chen, Shu-Hua Chou, Ken-Tsung Wong, and Chien-Hong Cheng. Design and synthesis of iridium bis(carbene) complexes for efficient blue electrophosphorescence. *Chem. Eur. J.*, 17(33):9180–9187, 2011.

[126] Nicholas J. Turro, V. Ramamurthy, and Juan Scaiano. *Modern Molecular Photochemistry of Organic Molecules*. Palgrave Macmillan, 2010. ISBN 1891389254.

[127] Thomas Fuhrmann and Josef Salbeck. Functional molecular glasses: Building blocks for future optoelectronics. *Adv. Photochem.*, 27:83–166, 2002.

[128] Miloslav Nič, Jiří Jirát, Bedřich Košata, Aubrey Jenkins, and Alan McNaught, editors. *IUPAC Compendium of Chemical Terminology*. IUPAC, Research Triagle Park, NC, 2.1.0 edition, 2009. ISBN 0-9678550-9-8.

[129] Falk May, Valentina Marcon, Michael Ryan Hansen, Ferdinand Grozema, and Denis Andrienko. Relationship between supramolecular assembly and charge-carrier mobility in perylenediimide derivatives: The impact of side chains. *J. Mater. Chem.*, 21(26):9538, 2011.

[130] S. W Tsang, S. K So, and J. B Xu. Application of admittance spectroscopy to evaluate carrier mobility in organic charge transport materials. *J. Appl. Phys.*, 99 (1):013706–013706–7, 2006.

[131] P.W.M. Blom, H.C.F. Martens, and J.N. Huiberts. Charge transport in polymer light-emitting diodes. *Synthetic Metals*, 121(1-3):1621–1624, 2001.

[132] Manuel Schrader, Roland Fitzner, Moritz Hein, Chris Elschner, Björn Baumeier, Karl Leo, Moritz Riede, Peter Bäuerle, and Denis Andrienko. Comparative study of microscopic charge dynamics in crystalline Acceptor-Substituted oligothiophenes. *J. Am. Chem. Soc.*, 134(13):6052–6056, 2012.

[133] Björn Baumeier, Denis Andrienko, Yuchen Ma, and Michael Rohlfing. Excited states of Dicyanovinyl-Substituted oligothiophenes from Many-Body green's functions theory. *J. Chem. Theory Comput.*, 8(3):997–1002, 2012.

[134] R. S. Mulliken. Electronic population analysis on LCAO[Single Bond]MO molecular wave functions. i. *J. Chem. Phys.*, 23(10):1833, 1955.

[135] Roland Fitzner, Egon Reinold, Amaresh Mishra, Elena Mena-Osteritz, Hannah Ziehlke, Christian Körner, Karl Leo, Moritz Riede, Matthias Weil, Olga Tsaryova, André Weiß, Christian Uhrich, Martin Pfeiffer, and Peter Bäuerle. Dicyanovinyl–Substituted oligothiophenes: Structure-Property relationships and application in Vacuum-Processed small molecule organic solar cells. *Adv. Funct. Mater.*, 21(5):897–910, 2011.

[136] Jose A. Freire and Camila Tonezer. Density of states and energetic correlation in disordered molecular systems due to induced dipoles. *J. Chem. Phys.*, 130(13):134901, 2009.

[137] Jacopo Tomasi, Benedetta Mennucci, and Roberto Cammi. Quantum mechanical continuum solvation models. *Chem. Rev.*, 105(8):2999–3094, 2005.

[138] Yu.N. Gartstein and E.M. Conwell. High-field hopping mobility in molecular systems with spatially correlated energetic disorder. *Chem. Phys. Lett.*, 245(4–5):351–358, 1995.

[139] S. V. Novikov and A. V. Vannikov. Hopping charge transport in disordered organic materials: Where is the disorder? *J. Phys. Chem. C*, 113(6):2532–2540, 2009.

[140] Conor Madigan and Vladimir Bulović. Exciton energy disorder in polar amorphous organic thin films: Monte carlo calculations. *Phys. Rev. B*, 75(8):081403, 2007.

[141] Ralph Young. Dipolar lattice model of disorder in random media analytical evaluation of the gaussian disorder model. *Philos. Mag. B*, 72:435–457, 1995.

[142] L. Kador. Stochastic theory of inhomogeneous spectroscopic line shapes reinvestigated. *J. Chem. Phys.*, 95(8):5574–5581, 1991.

[143] A. K. Rappe, C. J. Casewit, K. S. Colwell, W. A. Goddard, and W. M. Skiff. UFF, a full periodic table force field for molecular mechanics and molecular dynamics simulations. *J. Am. Chem. Soc.*, 114(25):10024–10035, 1992.

[144] Dennis M Elking, Lalith Perera, Robert Duke, Thomas Darden, and Lee G Pedersen. A finite field method for calculating molecular polarizability tensors for arbitrary multipole rank. *J. Comput. Chem.*, 32(15):3283–3295, 2011.

[145] X. Feng, V. Marcon, Wojciech Pisula, Michael Ryan Hansen, James Kirkpatrick, F. Grozema, Denis Andrienko, Kurt Kremer, and Klaus Müllen. Rational design of the shape and periphery of discotics: a synthetic way towards high charge carrier mobilities. *Nat. Mater.*, 8:421 – 426, 2009.

[146] G Horowitz, F Kouki, P Spearman, D Fichou, C Nogues, X Pan, and F Garnier. Evidence for n-type conduction in a perylene tetracarboxylic diimide derivative. *Adv. Mat.*, 8(3):242, 1996.

[147] RJ Chesterfield, JC McKeen, CR Newman, PC Ewbank, DA da Silva, JL Bredas, LL Miller, KR Mann, and CD Frisbie. Organic thin film transistors based on n-alkyl perylene diimides: Charge transport kinetics as a function of gate voltage and temperature. *J. Phys. Chem. B*, 108(50):19281–19292, 2004.

[148] JY Kim, IJ Chung, YC Kim, and JW Yu. Mobility of electrons and holes in a liquid crystalline perylene diimide thin film with time of flight technique. *Chem. Phys. Lett.*, 398:367–371, 2004.

[149] PRL Malenfant, CD Dimitrakopoulos, JD Gelorme, LL Kosbar, TO Graham, A Curioni, and W Andreoni. N-type organic thin-film transistor with high field-effect mobility based on a n,n-'-dialkyl-3,4,9,10-perylene tetracarboxylic diimide derivative. *App. Phys. Lett.*, 80(14):2517–2519, 2002.

[150] Ian A. Howard, Frederic Laquai, Panagiotis E. Keivanidis, Richard H. Friend, and Neil C. Greenham. Perylene tetracarboxydiimide as an electron acceptor in organic solar cells: A study of charge generation and recombination. *J. Phys. Chem. C*, 113 (50):21225–21232, 2009.

[151] BA Jones, MJ Ahrens, MH Yoon, A Facchetti, TJ Marks, and MR Wasielewski. High-mobility air-stable n-type semiconductors with processing versatility: Dicyanoperylene-3,4 : 9,10-bis(dicarboximides). *Ang. Chem. Int. Ed.*, 43(46):6363–6366, 2004.

[152] Z. J. Chen, V. Stepanenko, V. Dehm, P. Prins, L. D. A. Siebbeles, J. Seibt, P. Marquetand, V. Engel, and F. Würthner. Photoluminescence and conductivity of self-assembled pi-pi stacks of perylene bisimide dyes. *Chem. A Eur. J.*, 13(2):436–449, 2007.

[153] X Zhang, ZJ Chen, and F Würthner. Morphology control of fluorescent nanoaggregates by co-self-assembly of wedge- and dumbbell-shaped amphiphilic perylene bisimides. *J. Am. Chem. Soc.*, 129(16):4886, 2007.

[154] F. Würthner. Perylene bisimide dyes as versatile building blocks for functional supramolecular architectures. *Chem. Comm.*, (14):1564–1579, 2004.

[155] Z. Chen, V. Stepanenko, V. Dehm, P. Prins, L. D. A. Siebbeles, J. Seibt, P. Marquetand, V. Engel, and F. Würthner. *Chem.-Eur. J.*, 13:436, 2007.

[156] I McCulloch, M Heeney, ML Chabinyc, D DeLongchamp, RJ Kline, M Coelle, W Duffy, D Fischer, D Gundlach, B Hamadani, R Hamilton, L Richter, A Salleo, M Shkunov, D Sporrowe, S Tierney, and W Zhong. Semiconducting thienothiophene

copolymers: Design, synthesis, morphology, and performance in thin-film organic transistors. *Adv. Mat.*, 21:1091–1109, 2009.

[157] H Sirringhaus, P. J. Brown, R. H. Friend, M. M. Nielsen, K Bechgaard, B. M. W. Langeveld-Voss, AJH Spiering, RAJ Janssen, EW Meijer, P Herwig, and DM de Leeuw. Two-dimensional charge transport in self-organized, high-mobility conjugated polymers. *Nature*, 401(6754):685–688, 1999.

[158] W. Pisula, M. Kastler, D. Wasserfallen, M. Mondeshki, J. Piris, I. Schnell, and K. Müllen. Relation between supramolecular order and charge carrier mobility of branched alkyl hexa-peri-hexabenzocoronenes. *Chem. Mat.*, 18(16):3634–3640, 2006.

[159] M. R. Hansen, R. Graf, S. Sekharan, and D. Sebastiani. Columnar packing motifs of functionalized perylene derivatives: Local molecular order despite long-range disorder. *J. Am. Chem. Soc.*, 131(14):5251–5256, 2009.

[160] V. Marcon, T. Vehoff, J. Kirkpatrick, Ch. Jeong, Do. Y. Yoon, K. Kremer, and D. Andrienko. Columnar mesophases of hexabenzocoronene derivatives. i. phase transitions. *J. Chem. Phys.*, 129:094505, 2008.

[161] V. Marcon, J. Kirkpatrick, W. Pisula, and D. Andrienko. Supramolecular structure of perylene tetracarboxdiimides. *Phys. Stat. Solidi B*, 245:820–824, 2008.

[162] Valentina Marcon, Dag W. Breiby, Wojciech Pisula, Julie Dahl, James Kirkpatrick, Sameer Patwardhan, Ferdinand Grozema, and Denis Andrienko. Understanding structure-mobility relations for perylene tetracarboxydiimide derivatives. *J. Am. Chem. Soc.*, 131(32):11426–11432, 2009.

[163] J. R. Yates, T. N. Pham, C. J. Pickard, F. Mauri, A. M. Amado, A. M. Gil, and S. P. Brown. An investigation of weak ch center dot center dot center dot o hydrogen bonds in maltose anomers by a combination of calculation and experimental solid-state nmr spectroscopy. *J. Am. Chem. Soc.*, 127:10216–10220, 2005.

[164] A.-C. Uldry, J. M. Griffin, J. R. Yates, M. Perez-Torralba, M. D. S. Maria, A. L. Webber, M. L. L. Beaumont, A. Samoson, R. M. Claramunt, C. J. Pickard, and S. P. Brown. Quantifying weak hydrogen bonding in uracil and 4-cyano-4 '-ethynylbiphenyl: a combined computational and experimental investigation of nmr chemical shifts in the solid state. *J. Am. Chem. Soc.*, 130:945–954, 2008.

[165] M. R. Hansen, T. Schnitzler, W. Pisula, R. Graf, K. Müllen, and H. W. Spiess. Cooperative molecular motion within a self-assembled liquid-crystalline molecular wire: the case of a teg-substituted perylenediimide disc. *Angew. Chem. Int. Ed.*, 48: 4621–4624, 2009.

[166] E. Lindahl, B. Hess, and D. van der Spoel. Gromacs 3.0: a package for molecular simulation and trajectory analysis. *J. Mol. Mod.*, 7:306–317, 2001.

[167] Paulette Clancy. Application of molecular simulation techniques to the study of factors affecting the Thin-Film morphology of Small-Molecule organic semiconductors. *Chem. Mater.*, 23(3):522–543, 2011.

[168] J. J. M. van der Holst, M. A. Uijttewaal, B. Ramachandhran, R. Coehoorn, P. A. Bobbert, G. A. de Wijs, and R. A. de Groot. Modeling and analysis of the three-dimensional current density in sandwich-type single-carrier devices of disordered organic semiconductors. *Phys. Rev. B*, 79(8):085203, 2009.

[169] Mark E Casida, Christine Jamorski, Kim C Casida, and Dennis R Salahub. Molecular excitation energies to high-lying bound states from time-dependent density-functional response theory: Characterization and correction of the time-dependent local density approximation ionization threshold. *J. Chem. Phys.*, 108(11):4439–4449, 1998.

[170] Mary A Rohrdanz and John M Herbert. Simultaneous benchmarking of ground- and excited-state properties with long-range-corrected density functional theory. *J. Chem. Phys.*, 129(3):034107–034107–9, 2008.

[171] Roberto Peverati and Donald G. Truhlar. Improving the accuracy of hybrid Meta-GGA density functionals by range separation. *J. Phys. Chem. Lett.*, 2(21):2810–2817, 2011.

[172] Tamar Stein, Leeor Kronik, and Roi Baer. Reliable prediction of charge transfer excitations in molecular complexes using Time-Dependent density functional theory. *J. Am. Chem. Soc.*, 131(8):2818–2820, 2009.

[173] John S Sears, Thomas Koerzdoerfer, Cai-Rong Zhang, and Jean-Luc Brédas. Communication: Orbital instabilities and triplet states from time-dependent density functional theory and long-range corrected functionals. *J. Chem. Phys.*, 135(15):151103–151103–4, 2011.

[174] Giovanni Onida, Lucia Reining, and Angel Rubio. Electronic excitations: density-functional versus many-body green's-function approaches. *Rev. Mod. Phys.*, 74(2): 601, 2002.

[175] David Beljonne, Carles Curutchet, Gregory D. Scholes, and Robert J. Silbey. Beyond förster resonance energy transfer in biological and nanoscale systems. *J. Phys. Chem. B*, 113(19):6583–6599, 2009.

[176] Mathias Pabst, Bernd Lunkenheimer, and Andreas Köhn. The triplet excimer of naphthalene: A model system for Triplet-Triplet interactions and its spectral properties. *J. Phys. Chem. C*, 115(16):8335–8344, 2011.

# Danksagung

Zunächst möchte ich mich bei meinem Betreuer Prof. Kurt Kremer bedanken, der mir ermöglicht hat, meine Doktorarbeit in der Theorie Gruppe des Max-Planck-Instituts für Polymerforschung in Mainz (MPIP) zu schreiben. Mein Dank gilt auch dem zweiten Berichterstatter Prof. Kurt Binder für die zügige Lektüre meiner Arbeit.

Des weiteren möchte ich mich bei Dr. Denis Andrienko bedanken, der mich in der Arbeitsgruppe Organische Elektronik am MPIP mit großem Enthusiasmus betreut hat. Ich möchte mich außerdem für die hervorragende Kooperation mit Dr. Christian Lennartz von der BASF bedanken.

Mein Dank gebührt aber ebenso allen Mitgliedern der Gruppe Organische Elektronik am MPIP. Dazu gehör(t)en Dr. Björn Baumeier, dem ich für seinen unermüdlichen Einsatz beim Korrekturlesen meiner Doktorarbeit sowie für die Unterstützung bei quantenchemischen Rechnungen danke möchte, Dr. Victor Rühle, der das Gerüst für unsere Computersimulationen aufgebaut hat, Dr. Sasha Lukyanov von dem ich viel über dispersiven Transport gelernt habe, Dr. Thorsten Vehoff dem ich für Einblicke in den Ladungstransport in organischen Kristallen danke, Manuel Schrader, mit dem ich viele spannende Diskussionen in unserem gemeinsamen Büro hatte, Carl Poelking der mir im Verständnis der polarisierbaren Kraftfelder zur Lageenergieberechnung geholfen hat und Pascal Kordt, dem ich für Erklärungen zu Simulationen mit mehreren Ladungsträgern danken möchte.

Außerhalb der Gruppe möchte ich insbesondere bei Dr. Christoph Junghans und Konstantin Koschke für die technische Unterstützung am MPIP bedanken.

Danke auch an Torsten Stühn, Harald Bopp und Robert Klein für die Betreuung des Rechenclusters am MPI und ebenso an das Rechenzentrum Garching, ohne deren Hilfe meine numerischen Berechnungen den zeitlichen Rahmen meiner Doktorarbeit gesprengt hätten.

Zudem möchte ich mich für spannende Diskussionen am Innovation Lab in Heidelberg bedanken, wo ich vor allem bei Bernd Lunkenheimer von der Uni Mainz sowie bei Mustapha Al-Helwi und Andreas Fuchs von der BASF ein offenes Ohr für wissenschaftliche Fragestellung gefunden habe.

Zuletzt möchte ich mich bei all denen bedanken, die mich außerhalb der Physik begleitet haben, und ohne deren Hilfe ich nie so weit gekommen wäre - insbesondere bei meiner Frau Katrin, meinem Sohn Maximilian sowie meine Eltern, und meinem Bruder.